406
4/17/78

ANL/FPP-77-4

ANL/FPP-77-4

FUSION POWER PROGRAM
QUARTERLY PROGRESS REPORT

July–September 1977

U of C-AUA-USDOE

ARGONNE NATIONAL LABORATORY, ARGONNE, ILLINOIS

Prepared for the U. S. DEPARTMENT OF ENERGY
under Contract W-31-109-Eng-38

DISCLAIMER

Printed in the United States of America
Available from
National Technical Information Service
U. S. Department of Commerce
5285 Port Royal Road
Springfield, Virginia 22161
Price: Printed Copy $6.50; Microfiche $3.00

Distribution Categories:
UC-20, -20a, -20b, -20c,
-20d, -20e, -20f, -20g

ANL/FPP-77-4

ARGONNE NATIONAL LABORATORY
9700 South Cass Avenue
Argonne, Illinois 60439

FUSION POWER PROGRAM
QUARTERLY PROGRESS REPORT

July—September 1977

Charles C. Baker, Director
Joseph B. Darby, Jr., Associate Director
Samuel D. Harkness, Associate Director

FOREWORD

This quarterly report describes fusion-related activities in research, development, and reactor design and analysis conducted within the Fusion Power Program and within other programs at Argonne National Laboratory.

Previous quarterly reports issued were:

CTR/TM-11	January-March 1974
CTR/TM-24	April-June 1974
CTR/TM-29	July-September 1974
CTR/TM-38	October-December 1974
ANL/CTR/TM-39	January-March 1975
ANL/CTR/TM-45	April-June 1975
ANL/CTR-75-3	July-September 1975
ANL/CTR-75-5	October-December 1975
ANL/CTR-76-2	January-March 1976
ANL/CTR-76-4	April-June 1976
ANL/CTR-76-5	July-September 1976
ANL/FPP-76-6	October-December 1976
ANL/FPP-77-1	January-March 1977
ANL/FPP-77-2	April-June 1977

TABLE OF CONTENTS

TABLE OF CONTENTS (Continued)

TABLE OF CONTENTS (Continued)

LIST OF FIGURES

LIST OF FIGURES (Continued)

LIST OF FIGURES (Continued)

LIST OF FIGURES (Continued)

LIST OF TABLES

I. FUSION REACTOR MATERIALS

A. Plasma Materials Interactions

1. An Accelerator System for Producing Two-Component Beams for Studies of Interactive Surface Effects

M. Kaminsky, S. K. Das, R. Ekern and D. C. Hess, Physics Division

With the aid of single-component irradiation facilities (e.g. particle accelerators, x-ray sources) and low-energy plasma devices, a number of surface effects have been identified as contributing to plasma contaminant release and wall erosion in large size plasma devices. These effects include blistering, chemical and physical sputtering, chemical trapping and compound formation, desorption by particle and photon impact, vaporization, backscattering and photodecomposition. While single component irradiations have yielded useful information concerning effects caused by certain projectile/surface interactions, they cannot provide any information about interactive effects. Such effects arise from the simultaneous interaction of two or more radiation components with surfaces and together cause a total effect on plasma contaminant release and/or surface erosion which is different from the sum of the effects caused by the individual radiation components. Since our knowledge of the occurrence of interactive effects is extremely limited, it appears highly desirable to determine their existence and their influence on plasma contaminant release and surface erosion. This appears especially desirable since the occurrence of synergistic effects appears to be very likely under certain irradiation conditions.[1-4] For example, the simultaneous irradiation of a metal surface by energetic and chemically active deuterons and by energetic and chemically inert helium ions may result in concurrent chemical and physical trapping. In addition, the simultaneous formation of metal deuterides and helium blisters could lead to enhanced plasma contaminant release and surface erosion. In order to facilitate the search for synergistics on surface erosion and plasma contaminant release caused by the interaction of two ion beam components with solid surfaces, a facility that is capable of supplying two different but colinear ion beams at two different energies has recently been constructed and has been put into operation. A brief description of the major features of this facility is given in the paper. A description of preliminary results obtained under the simultaneous irradiation of Ni with 50-keV D^+ and 100-keV $^4He^+$ ions is included. These results will be compared with those obtained for bombarding Ni with either 50-keV D^+ or 100-keV $^4He^+$ ions, and those obtained for sequential irradiation of Ni with the same type of energetic projectiles.

---

[1] M. Kaminsky, Proceedings of International Working Session on Fusion Reactor Technology, Oak Ridge National Laboratory, USAEC, CONF-719624, Oak Ridge (1971), p. 86.

[2] M. Kaminsky, S. K. Das, Proc. of 4th Conference of Scientific and Industrial Applications of Small Accelerators, (IEEE) Denton, Texas (1976), p. 238.

[3] F. Cafasso, et al., Nuclear Technology 34, (1977), 131.

[4] ERDA Report 1977, "Multiple Component Materials Test Facilities for Magnetic Fusion Energy, U.S. ERDA 77-52 (April, 1977).

a. System for Production of Two-Component Beams

The system consists of a 2-MV van de Graaff and a 100-kV dc accelerator which is operated as an injector into the beam line of the 2-MV van de Graaff as shown schematically in Figure I-1. One of the significant design features of the system is that it permits the simultaneous bombardment of materials with a colinear, two-component ion beam. The latter feature of colinearity of the two merging beams allows the angle of beam incidence to be a free parameter. This feature, as well as the operating voltage ranges of the two accelerators (0.1 - 2.1 MV VdG, 10-100 kV dc accelerator), distinguish the new system from some other two-component systems which are being used.[5]

As can be seen in Figure I-1, the 2-MV van de Graaff and beam transport system consists of the accelerator, the electrostatic beam steerers, a 90° bending magnet with a 40-inch mean radius, insulated entrance and exit slits, two electromagnetic quadrupole doublets, and parallel plate deflectors. The beam line is of stainless steel and is pumped by a 1000 liter/s turbomolecular pump and three ion-sublimation pumps at the locations indicated (the pumping speed for N_2 for one ion pump is 400 liter/s, and for the other two pumps 200 liter/s). This type of pumping results in an operating beam line pressure of 2×10^{-7} torr at the 2-MV high voltage terminal (ion source operating), 2×10^{-8} torr at the end of the beam line, and 2×10^{-9} torr in the target chamber, which is independently pumped by a 400 liter/s ion pump and a sublimation pump. After baking the beam line and target chamber for four hours at 120°C, the pressure in the target chamber is reduced by a factor of 2 to 3. The choice of pumps and beam line components has helped significantly to reduce carbon contamination buildup on the irradiated sample.

The 100-kV accelerator system consists of the same type of rf-ion source which is being used at the 2 MV van de Graaff (operating at a frequency of 100 MHz), a 15-stage acceleration tube, an electrostatic beam steerer, insulated adjustable entrance and exit slits for the bending magnet, a 90° bending magnet with a mean radius of curvature of 30 cm, a maximum field of 4.2 kG, and with shims to provide fixed entrance and exit angles of 26.6° in order to obtain some double focussing and stigmatic focussing action. The 100-kV dc accelerating voltage with 5 mA current capability is obtained from a commercial power supply (Megavolt, Inc., Palisades Park, New Jersey) and is regulated to better than 0.01%. A precision resistor divider network on the high voltage permits readout of the accelerating voltage to within 1 part of 10^4. The bending magnet is followed by a target chamber assembly which allows experiments to be carried out with an analyzed beam from the 100-kV accelerator only. A gate valve provides complete isolation of this system from the 2-MV van de Graaff system. The target chamber assembly consists of apertures, shutters, beam viewing ports, target manipulators (micrometer drives) and a 25 liter/s ion pump combined with a sublimation pump. Pressures of 2-5 x 10^{-9} torr can be reached in this chamber (without baking) with the ion source

[5] A. Taylor, et al., Proceedings of the International Conference on Radiation Effects and Tritium Technology for Fusion Reactors, ERDA CONF-750989, Vol. 1., (1976), p. 158.

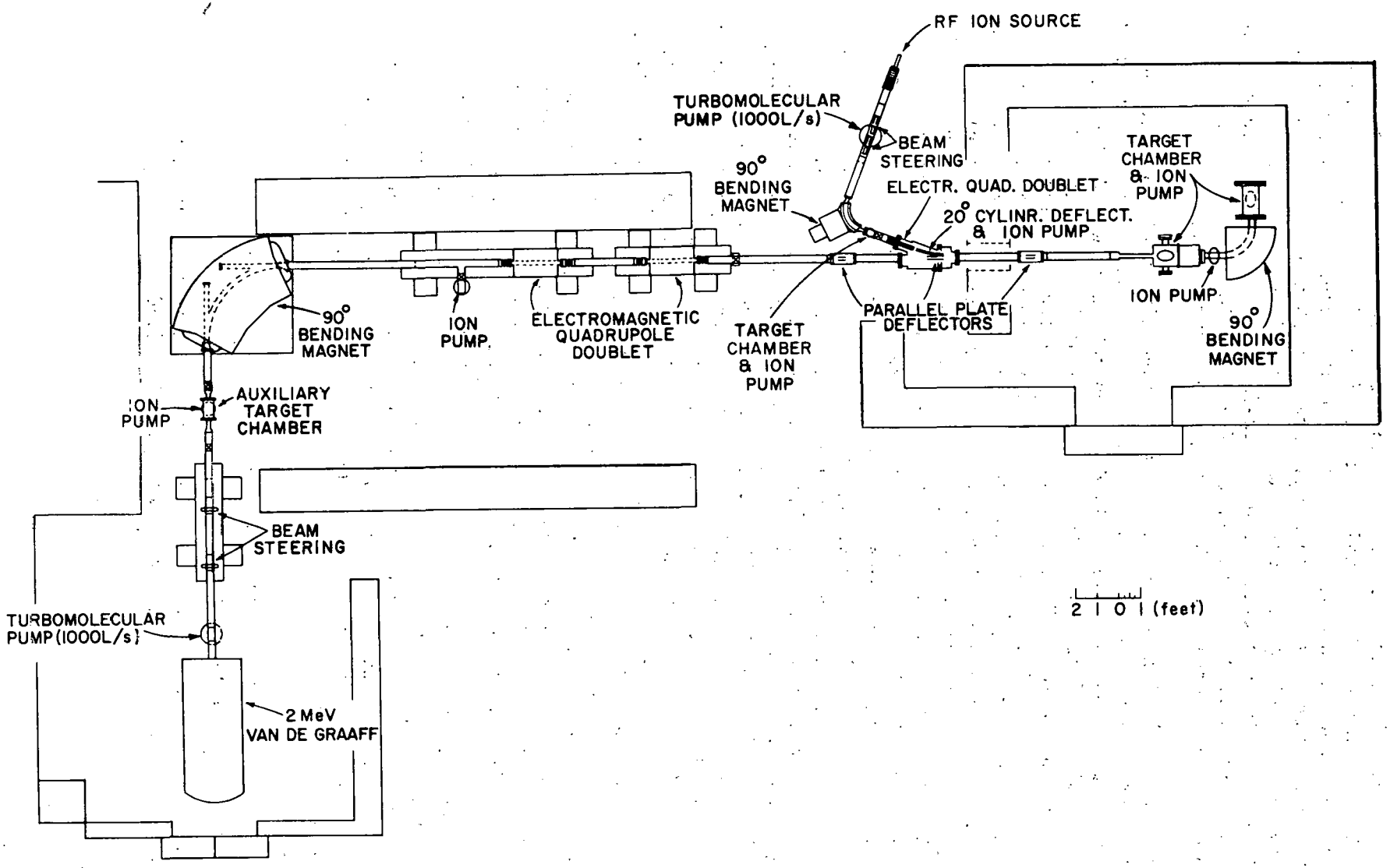

Figure I-1. Schematic diagram of the two-component irradiation facility showing 2-MV van de Graff accelerator with injector system for simultaneous irradiation of surfaces with ions of different mass and energy.

in operation. Typical analyzed D^+ ion current densities on target in this chamber are 800 μA cm^{-2} at 50-keV and 1.2 mA cm^{-2} at 100-keV (on a ∿ 2 mm target spot). In order to use the beam from the 100-kV accelerator for dual beam irradiations it is passed through the target chamber and enters an electrostatic quadrupole doublet (each singlet has 2.54 cm diameter aluminum electrodes, 7.5 cm long) for steering and/or focussing purposes, and to compensate in part for the cylindrical electrostatic deflector which is used to inject the beam into the 2-MV accelerator beam line (see Figure I-1).

The problem of merging two ion beams which have different energies and different beam axis directions into a co-linear beam which can be collimated before striking the target has been solved in the following way.[6] A special, triple parallel plate deflection system has been installed in the 2-MV beam at the locations indicated in Figure I-1. The energetic ion beam from the 2-MV van de Graaff is deflected by an electrostatic field between the first set of parallel plates (effective electrical length d) by an angle θ from the original beam axis and allowed to drift to the second set of parallel deflection plates for a distance of ℓ (measured from center to center of plate set 1 and 2). The field of the second set of plates (effective electrical length 2 d) deflects the beam in the reverse direction by an angle of 2 θ and allows the beam to drift again for a distance of ℓ to the third set of parallel plates (effective electrical length d). Here, the field between the plates causes the deflection by an angle θ and returns the beam direction to the original beam direction. The electrostatic fields in all three deflectors have the same value. The ion beam from the 100-kV injector is introduced into the beam line of the 2-MV accelerator at a design angle of 20°. Minor deviations of the beam from this angle can be made by a pair of short deflection plates at the exit of the 20° electrostatic deflector. The object is to have the 100-kV beam enter the final set of parallel plates at such an angle and location that when it is bent by these plates, it will be coaxial with the beam from the 2-MV Van de Graaff. Since the two beams merge colinearly more than 1.5 m in front of the target, a set of beam collimators can be used to decrease the angular divergence of the merged beams to less than 0.01°. Typical current densities on a 2 mm target spot for two highly collimated, merged ion beam components of 100-keV D^+ and 500-keV $^4He^+$ are 100 μA cm^{-2}. It is intended to install an additional electrostatic quadrupole lens about 1 meter from the target to increase the current densities on target to increase the current densities on target. The 90° analyzing magnet following the target chamber and the final target chamber (housing detectors and/or targets) have been used for the analysis of sputtered species and the determination of gases released by radiation blistering[7] as well as for studies of charge states of ions penetrating through monocrystalline and polycrystalline samples.[8]

---

[6] R. Ekern, D. C. Hess and M. Kaminsky, paper in preparation.

[7] M. Kaminsky, Adv. Mass Spectrom. 3, 69.

[8] M. Kaminsky, "Recent Developments in Mass Spectrometry," University Park Press, editors K. Ogata and T. Hayakawa, p. 1167 (1970).

b. Target Preparation and Irradiation

The polycrystalline nickel targets used in the present studies were obtained from Materials Research Corporation and had a nominal purity of 99.995% (Marz Grade). Thin foils of $\sim$ 0.003" thickness were first given a fine metallographic polish and then annealed at 700° for 2 hours in a vacuum of $\sim 1 \times 10^{-7}$ torr. The targets were then electropolished in a solution containing 280 ml phosphoric acid, 86 ml distilled water, 20 ml sulphuric acid and 4 g of chromium trioxide. For the irradiation of the targets at 500°C they were resistively heated, and the temperature was monitored by an infrared pyrometer.

In a first set of experiments a search was made for interactive effects due to the simultaneous irradiation of nickel with D^+ and He^+ ions with energies of 500-keV and 100-keV, respectively and the target temperature was held at 500°C. The projected range distribution and the depth distribution of energy deposited into damage for 50-keV D^+ and 100-keV He^+ are similar, as can be seen in Figure I-2. The projected range distributions and the damage distributions were calculated as a function of depth for 100-keV He^+ using Brice's formalism,[9] whereas those for 50-keV D^+ were calculated according to Winterbon.[10] In order to see whether the surface damage observed during simultaneous irradiation is an interactive effect or not, five sets of irradiations were performed; two separate irradiations with the two individual components, sequential irradiation with 50-keV D^+ and then 100-keV He^+, another sequential irradiation with reversed order (i.e., first 100-keV He^+ and then 50-keV D^+ irradiation) and finally, simultaneous irradiation with 50-keV D^+ and 100-keV He^+ ions. The total doses were 0.5 C/cm^2 and 0.1 C/cm^2 for 50-keV D^+ and 100-keV He^+ ion irradiation, respectively. During the simultaneous irradiation, the fluxes of individual components were adjusted ($\sim 4 \times 10^{13}$ and $\sim 2 \times 10^{14}$ ions cm^{-2} s^{-1} for He^+ and D^+ components, respectively) so that the total irradiation time was the same for the two components.

c. Results and Discussion

The irradiation of annealed polycrystalline nickel at 500°C with 50-keV D^+ ions to a dose of 0.5 C/cm^2 did not produce any detectable changes on the surface and a typical irradiated area is shown in the scanning electron micrograph in Figure I-3a. For irradiation with 100-keV $^4He^+$ ions to a dose of 0.1 C/cm^2 at the same temperature of 500°C, again, no detectable changes in the surface structure were observed (Figure I-3b), except in one repeat run in which only a few blisters (average diameter $\sim$ 4.3 μm) were observed in a small portion of the irradiated area. Figure I-3c shows a scanning electron micrograph of a nickel surface irradiated simultaneously with 100-keV He^+ and 50-keV D^+ for total doses of 0.1 and 0.5 C/cm^2, respectively. For this case, many blisters could be seen in the irradiated area. The blister diameters for this dual irradiation ranged from $\sim$ 2 μm to 8 μm and the average blister diameter for three repeat runs ranged from 4.2 to 5.0 μm. However,

[9] D. K. Brice, Ion Implantation Range and Energy Deposition Distribution, Vol. I (Plenum Data Company, New York) (1975).

[10] K. B. Winterbon, "Ion Implantation Range and Energy Deposition Distribution," Vol. II (Plenum Data Company, New York) (1975).

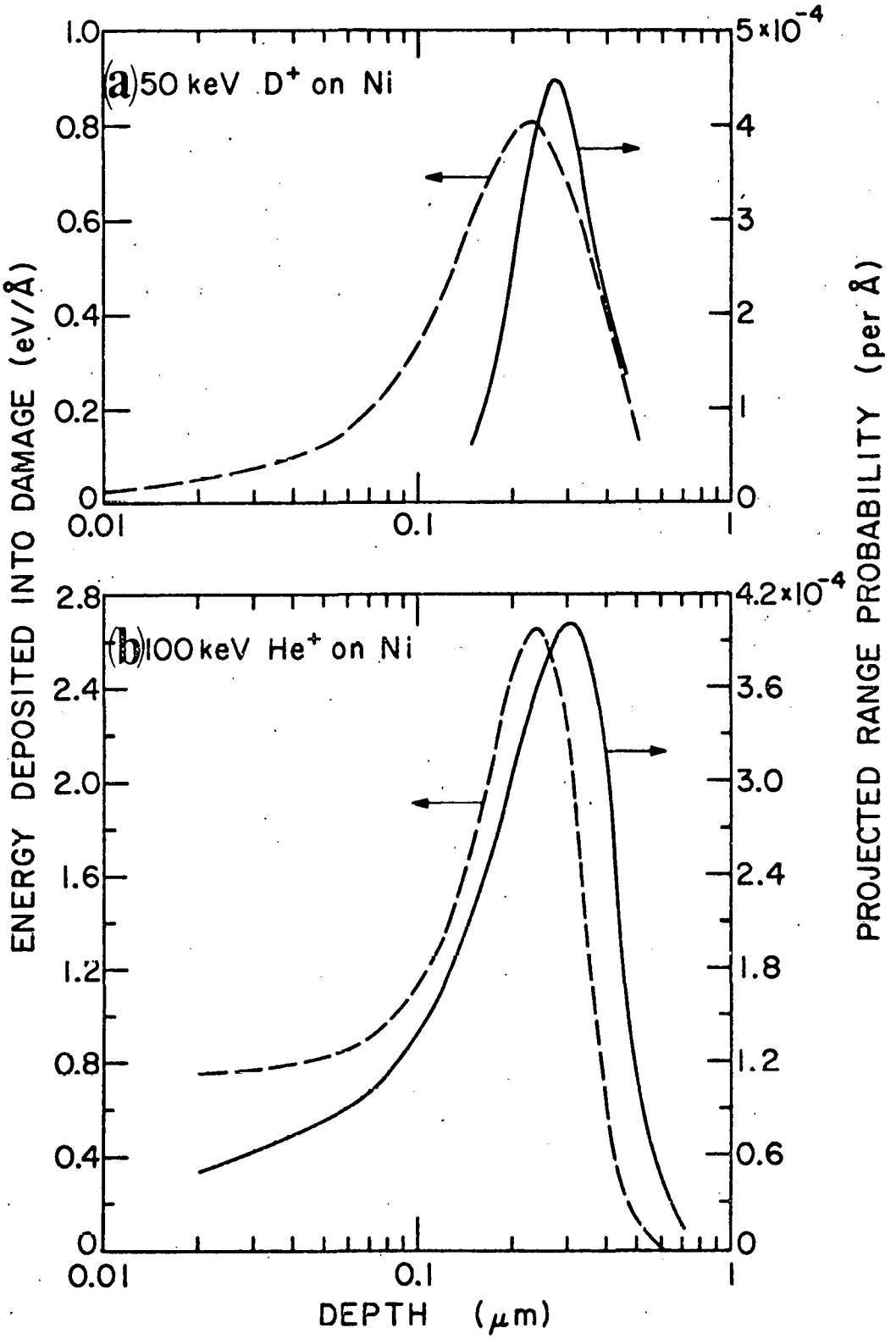

Figure I-2. Plots of projected range probability distributions (solid curves) and of damage-energy distributions (dashed curves) as a function of depth into Ni target (a) for 50-keV D^+ and (b) for 100-keV $^4He^+$ ions.

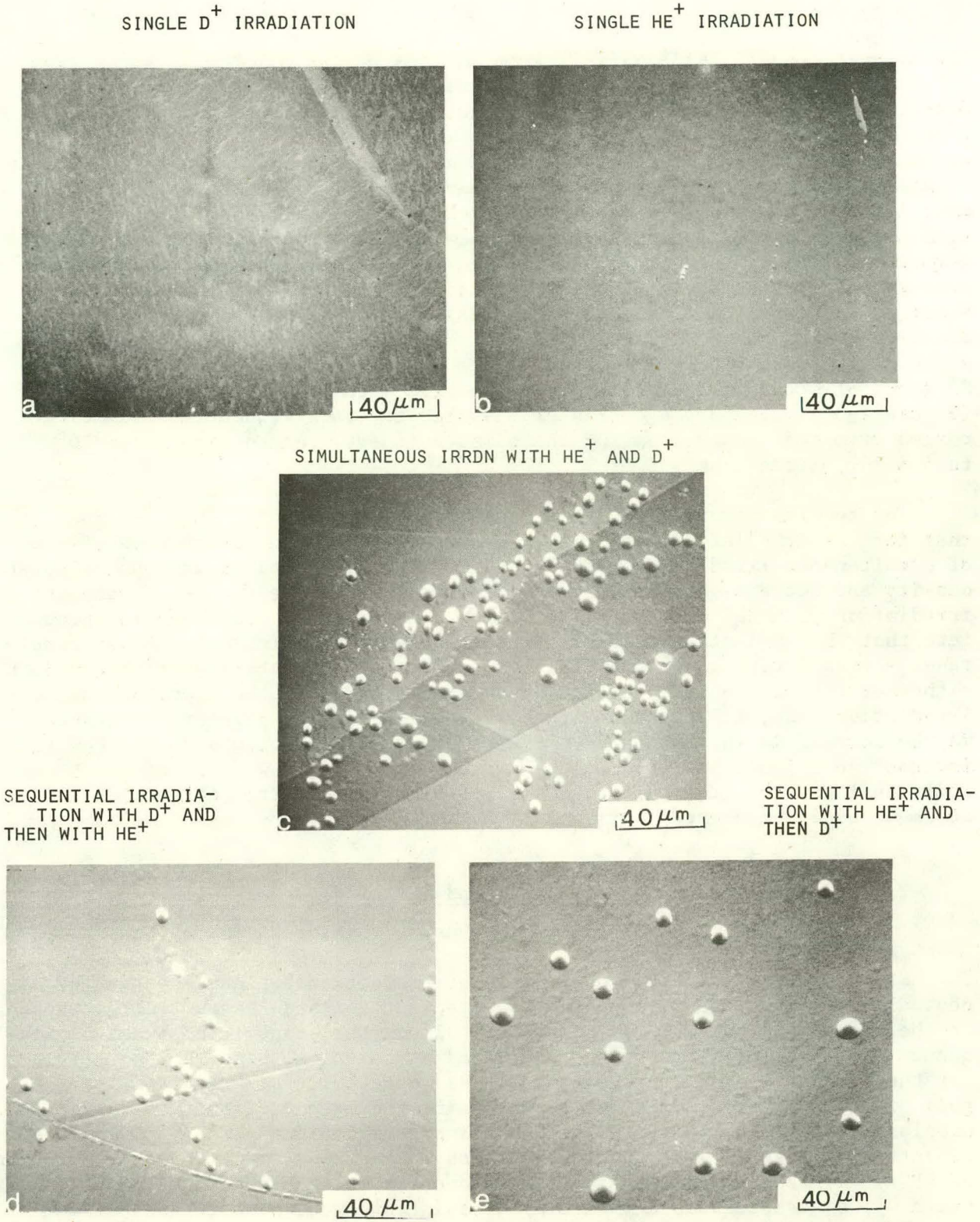

Figure I-3. Scanning electron micrographs of annealed polycrystalline nickel irradiated at 500°C (a) with 50-keV D^+ to a dose of 0.5 C/cm^2, (b) with 100-keV $^4He^+$ to a dose of 0.1 C/cm^2, (c) simultaneously with 100-keV $^4He^+$ and 50-keV D^+ to total doses of 0.1 and 0.5 C/cm^2, respectively, (d) sequentially with 50-keV D^+ to a dose of 0.5 C/cm^2, and then with 100-keV $^4He^+$ to a dose of 0.1 C/cm^2 and (e) sequentially with 100-keV $^4He^+$ to a dose of 0.1 C/cm^2 and then with 50-keV D^+ to a dose of 0.5 C/cm^2.

the blister density varied widely from one run to the other and ranged from 1.5×10^4 blisters/cm^2 to 9.4×10^5 blisters/cm^2. This variation in blister density may in part be related to differences in the fluxes and the total doses of individual components between the different runs. Since the flux of each component incident on the target during the irradiation was monitored manually, the error in the total doses may be $\sim$ 20%. A microprocessor will be used for an automatic control system for keeping the fluxes of the two beams constant within preset ranges and will be taken into operation shortly. Sequential irradiation with 50-keV D^+ and then with 100-keV He^+ to the same corresponding doses as in the single irradiations produce blisters with an average diameter of $\sim$ 5.8 μm (Figure I-3d). The blister density varied widely from 1×10^3 to 1×10^5 blisters/cm^2, between the repeat runs. For sequential irradiation, first with 100-keV He^+ ions, and then with 50-keV D^+ ions, blisters with diameters ranging from 4 to 10 μm could be observed (Figure I-3e). The average blister diameter for this sequential radiation ranged from 5.5 to $\sim$ 7.4 μm and the blister density ranged from $\sim 1 \times 10^5$ to 5×10^5 blisters/cm^2.

The results described above are preliminary in nature, but they indicate that for the irradiation conditions described above, the interactive effect of simultaneous irradiation with D^+ and He^+ ions may tend to increase blister density and decrease average blister diameter as compared to the sequential irradiation with He^+ and then with D^+ ion. This result leads one to speculate that the nucleation rate of helium bubbles may be increased under simultaneous irradiation with D^+ and He^+ ions. Since no blisters were observed in either of the single irradiations, but were observed in the simultaneous irradiation case, it appears that the critical dose for blister appearance may be lowered in the last case. Experiments are in progress to see how the interactive effects observed in the present experiments will change with individual ion energies and ion doses, together with better control of the doses of each component.

2. Surface Damage of Molybdenum and TZM Alloy Under D^+ Impact

S. K. Das, M. Kaminsky and P. Dusza, Physics Division

Several tokamak reactor designs require additional plasma heating by neutral beam injection. Since the injected neutral beam is partially trapped in the plasma, a beam dump is needed to collect the transmitted beam. Molybdenum and its alloys are being considered as potential beam dump materials for the Tokamak Fusion Test Teactor (TFTR) to be built at Princeton. The goal of the present studies was to determine the extent of surface damage and erosion (if any) that polycrystalline molybdenum would experience under the impact of intense D^+ ions under conditions to be expected during the operation of TFTR. Since the TFTR is expected to operate in a pulsed mode (duration of pulse $\sim$ 1 s at intervals of $\sim$ 1 min) irradiations were done in the pulsed mode for 100, 500, 1000 and 2500 pulses, and in the continuous mode for total doses corresponding to the dose values reached in the above number of pulses (i.e., the equivalent of 100, 500, 1000 and 2500 pulses). Estimates of deuterium fluxes striking the beam dump give[11] values of $\sim 1.7 \times 10^{15}$ D^+/(cm^2-s) at 40-keV, 2.9×10^{15} D^+/(cm^2-s) at 60-keV and 1.2×10^{16} D^+/(cm^2-s) at

[11] J. L. Cecchi, Princeton Plasma Physics Laboratory, private communication (1977).

120-keV. These estimates are based on the assumption that 10% of the 120-keV neutral beam component would not be absorbed by the plasma. There are no data available on surface damage of molybdenum under these irradiation conditions to be expected in TFTR (see Reference 12 for a review of surface damage due to blistering). H. Verbeek and W. Eckstein[13] observed blister formation in molybdenum irradiated at room temperature with 15-keV D^+ for total doses of 2.8×10^{18} ions/cm^2. G. McCracken and S. K. Erents[14] studied gas release from Mo surfaces under low energy D^+ irradiation but did not study any surface damage. Another aim of the present study was to see how the commercial Mo-base alloy TZM, a material with higher yield strength than Mo, would behave with respect to surface damage and erosion under D^+ irradiation.

a. Experimental Procedures

The molybdenum targets were obtained from Materials Research Corporation, Orangeburg, New York, as 1" wide and 0.005" thick foils. The TZM foils of the same dimensions as the Mo foils were obtained from Amax Specialty Metals Corporation, Cleveland, Ohio. The chemical composition of the foils as received from the manufacturer are given in Table I-1. Both Mo and TZM foils were received in the stress relieved condition and no further annealing was done. The targets (1" x 1/2") were first given a fine metallographic polish and then electropolished in a bath containing 87.5% methanol and 12.5% sulphuric acid at a temperature of 5°C.

The electropolished targets were characterized before and after irradiation using scanning electron microscopy and scanning Auger spectroscopy. The average grain size for both Mo and TZM was measured to be $\sim$ 4 μm. Auger spectra were taken from some typical electropolished Mo targets to determine the impurities present on the surface and the major surface impurities were O, C and N. After sputtering the surface with 2-keV Ar^+ ions, the C and O peaks are greatly reduced and the C and O impurities were roughly estimated to be $\sim$ 20 monolayers.

For irradiation, a mass analyzed beam of D^+ ions was produced by an accelerator system consisting of a duoplasmatron source, a beam profiler, an electrostatic beam steerer, an analyzing magnet, and a 150-kV dc supply. The analyzed D^+ ion beam passed through a quadrupole doublet for focussing and through two liquid nitrogen beam line traps to reduce carbon contamination on the irradiated targets. The focussed and analyzed beam then passed through a set of collimating apertures before striking either the target or a pneumatically operated shutter. The irradiated spot on the target was $\sim$ 3 mm in diameter. The target chamber consisted of a stainless steel cross with metal seal ports for the mounting of the stepping motor-target micro-manipulator arrangement, the viewing port, the pneumatically operated shutter,

---

12 S. K. Das and M. Kaminsky, Radiation Effects on Solid Surfaces, Adv. in Chem. Series 158 (American Chemical Society, Washington, 1976) p. 112.

13 H. Verbeek and W. Eckstein, Applications of Ion Beams to Metals, eds. S. T. Picraux, E. P. EerNisse and F. L. Vook (Plenum, New York 1974), p. 597.

14 G. M. McCracken and S. K. Erents, Applications of Ion Beams to Metals, eds. S. T. Picraux, E. P. EerNisse and F. L. Vook (Plenum, New York 1974) p. 585.

Table I-1. Chemical Composition of the Materials Used

Material	Major Elements Present (ppm)						
	Ti	Zr	O	C	Si	Fe	Ni
Mo	< 10	< 10	25	20	< 5	60	80
TZM	5000	1040	9	200	10	25	10

an ion-sublimation pump combination, and a front flange with beam entrance port plus smaller viewing windows (the window was used for the infrared pyrometer). During a typical run the pressure in the target chamber was 4-6 x 10^{-9} torr, and only in two runs was the pressure as high as 1.8 x 10^{-8} torr. The targets were mounted on a ∿ 3/4" diameter Cu-block having ten faces. A stepping motor allowed the precise rotation of the target assembly block in two-hundred steps (1.8° per step). In order to be able to irradiate more than one target during the period of the pulse repetition time of 60 s (the pulse length being only 1 s), a microproce-sor was used to automatically open the shutter for 1 s every 6 s, then, after each pulse, activate the step-motor to advance the next target of the 10 targets mounted on the target block into the beam position. The microprocessor system would store the total dose (dose determined using current integrator and biased apertures for secondary electron suppression) each target obtained during the entire pulsed irradiation. The target temperatures were not controlled (except for one set of high temperature irradiation at 300°C), but monitored using thermocouples and with the aid of an infrared pyrometer. The D^+ fluxes for 40-, 60-, and 120-keV were 1.7 x 10^{15}. 3.0 x 10^{15}, and 9 x 10^{15} ions/(cm^2-s), respectively. The irradiations were performed for 100, 500, 1000 and 2500 pulses and in the continuous mode for the same total dose as accumulated during the above number of pulses. Following the irradiation, the targets were examined with an energy dispersive X-ray spectrometer. The size distribution of the blisters observed in the irradiated samples were measured from the micrographs using a Zeiss particle size analyzer.

b. Results and Discussion

Molybdenum - Figure I-4a shows a scanning electron micrograph of a poly-crystalline surface irradiated with 40-keV D^+ for 2500 pulses (the total dose accumulated is 4.3 x 10^{10} ions/cm^2). For this dose, blisters can be readily seen on the surface. The blister diameters range from 2.5 to 20 μm and the values for the average blister diameter and blister density are 4.6 μm and 7.1 x 10^{14} blisters/cm^2, respectively. Figure I-4b shows a micrograph of the surface after irradiation with 40-keV D^+ ions in the continuous mode for a total dose of 4.3 x 10^{18} ions/cm^2 (equivalent of 2500 pulses). For this continuous irradiation the average blister diameter has decreased to ∿ 1.8 μm and the blister density is 2.8 x 10^5 blisters/cm^2. For the sake of comparison, a typical unirradiated area is shown in Figure I-4c. Figures I-4d and I-4e show typical molybdenum surfaces irradiated with 60-keV D^+ to a total dose of

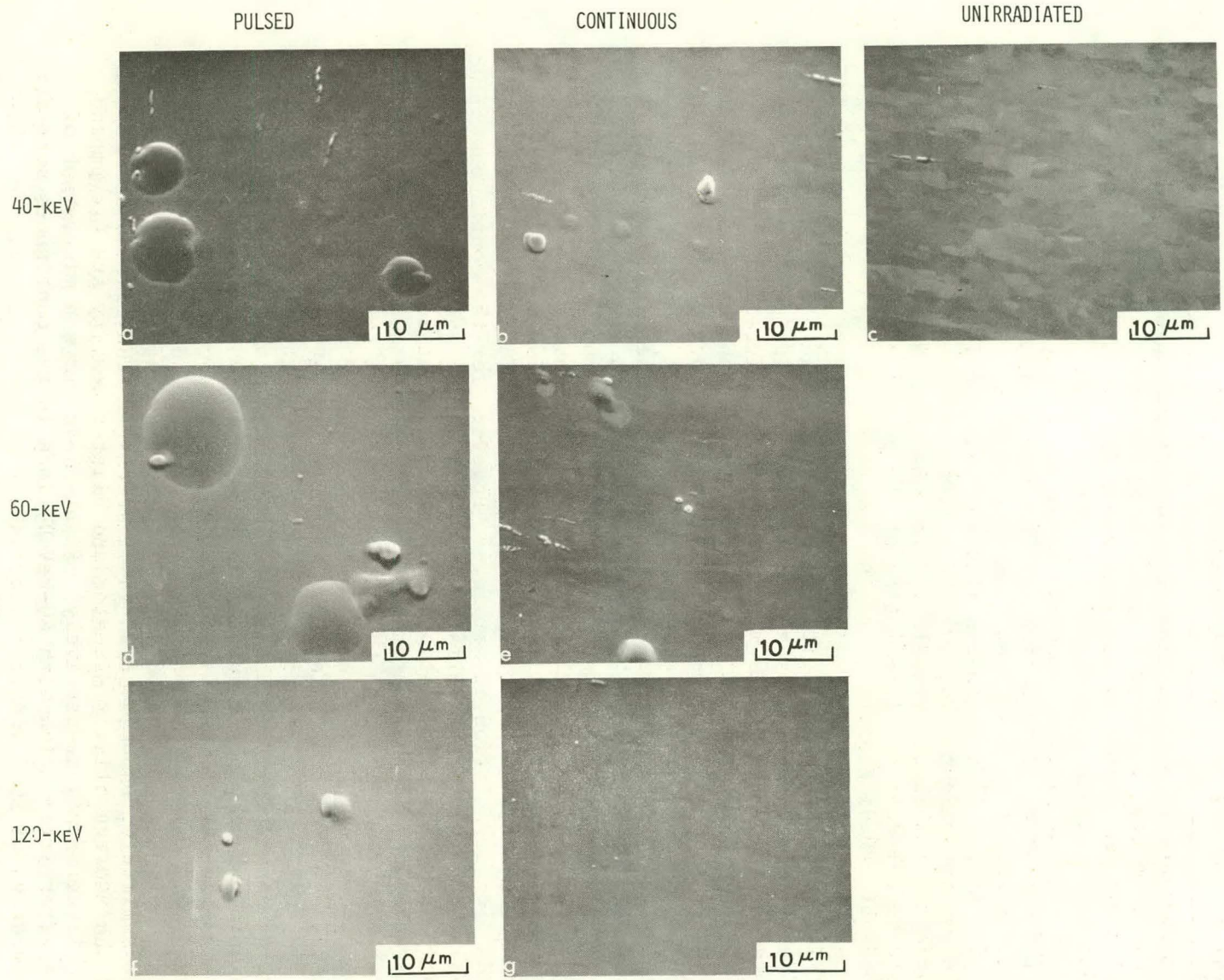

Figure I-4. Scanning electron micrographs (SEMs) of polycrystalline Mo surfaces irradiated (a) with 40-keV D^+ for 2500 pulses (equivalent dose 4.3 x 10^{18} ions/cm^2); (b) with 40-keV D^+ for 4.3 x 10^{18} ions/cm^2 in continuous mode; (c) an unirradiated area; (d) with 60-keV D^+ for 2500 pulses (equivalent dose: 8.1 x 10^{18} ions/cm^2); (e) with 60-keV D^+ for 8.1 x 10^{18} ions/cm^2 in continuous mode; (f) with 120-keV D^+ for 2500 pulses (equivalent dose: 2.2 x 10^{19} ions/cm^2; (g) with 120-keV D^+ for 2.2 x 10^{19} ions/cm^2 in continuous mode.

2500 pulses or its equivalent dose of 8.1×10^{18} ions/cm^2 in the continuous mode, respectively. The average blister diameter is 6.6 μm in the pulsed mode and 2.1 μm in the continuous mode. For irradiation with 120-keV D^+ for 2500 pulses, only a few blisters with diameters of 3-5.5 μm could be seen (Figure I-4f), but no blisters could be detected for continuous irradiation to a dose equivalent to 2500 pulses (Figure I-4g).

The distributions of blister diameters for the pulsed and continuous irradiation are compared in Figure I-5, in which the ordinate is the percentage of blisters in a class of blisters whose diameters fall within the range included in the width of each vertical bar. In the case of 40-keV D^+ pulsed irradiation, the blister diameters range up to $\sim$ 20 μm (Figure I-5a), whereas for the continuous irradiation for the same equivalent dose, the maximum blister diameter is less than 5 μm (Figure I-5c). Similar results are observed for 60-keV D^+ irradiation (Figures I-5b and I-5d). The effect of total dose was investigated for 100, 500, 1000 and 2500 pulses or their equivalent dose for continuous irradiation for the three energies. No blisters could be detected for irradiation of 100 pulses or its equivalent for either mode of irradiation.

Table I-2 summarizes the quantitative data on average blister diameter and blister density for both pulses and continuous irradiations for different doses. The target temperatures, as measured during the irradiations, are also listed in Table I-2. Here, it can be seen that in the case of pulsed irradiation for both 40-keV and 60-keV D^+ irradiation, both blister density and average blister diameter increase with the increasing number of pulses. It can also be seen that for an equivalent number of pulses, the average blister diameter is higher for 60-keV D^+ irradiation than for 40-keV D^+ irradiation for the pulsed mode of irradiation. For example, for 2500 pulses the average blister diameter is 4.6 μm for 40-keV irradiation, whereas it is 6.6 μm for 60-keV irradiation, but the values for the blister density do not appear to change significantly. This result is similar to those observed earlier for He^+ ion irradiation of metals.[12] However, for the continuous mode of irradiation, the average blister diameters do not change significantly in going from 40 to 60-keV irradiations for the equivalent dose values. For 120-keV D^+ irradiation, the blistering is greatly reduced as compared to 40- and 60-keV D^+ irradiation even though the total doses for an equivalent number of pulses were higher for the former case than for the latter two cases (see Table I-2). This reduction in blistering for 120-keV D^+ irradiation as compared to 40- and 60-keV D^+ irradiation can be partly attributed to the higher target temperature during the 120-keV D^+ irradiation. Since the target temperatures were not controlled during the irradiation, higher power deposition for the 120-keV D^+ irradiation caused the surface temperature to rise to $\sim$ 280°C (and bulk temperature measured behind the irradiated surface to $\sim$ 70°C) for the pulsed mode, and to 360-400°C for the continuous mode of irradiation. Similarly, the reduction in blistering in the continuous irradiation with 40- and 60-keV D^+ as compared to the pulsed irradiation, can, in part, be attributed to the higher target temperatures reached during the continuous irradiations ($\sim$ 260-295°C) as compared to the pulsed irradiations (surface temperature of 100-120°C).

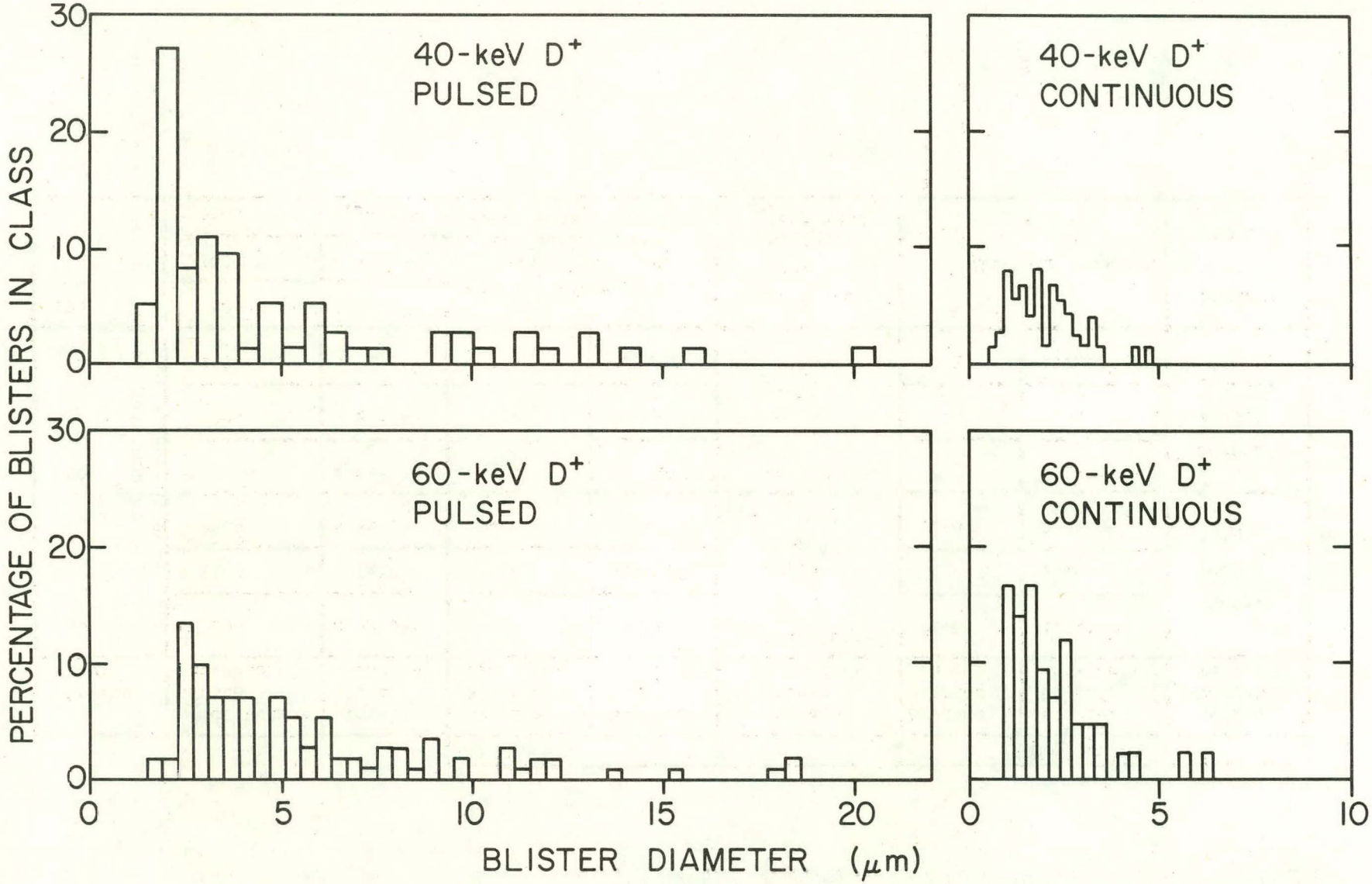

Figure I-5. Histograms of the percentage of blisters in a class for polycrystalline Mo irradiated (a) with 40-keV D^+ in pulsed mode; (b) with 60-keV D^+ in pulsed mode; (c) with 40-keV D^+ in continuous mode and (d) with 60-keV D^+ in continuous mode.

Table I-2. Summary of Average Blister Diameter and Blister Density for Mo Irradiated with D^+ Under Various Conditions

			PULSED			CONTINUOUS		
Energy (keV)	No.of Pulses or its Equivalent	Total Dose Ions/cm^2	Average Blister Dia. (μm)	Blister Density (no./cm^2)	Average Target Temp. (^oC)	Average Blister Dia.(μm)	Blister Density (no./cm^2)	Average Target Temp. (^oC)
40	500	8.7×10^{17}	2.8	3.1×10^4	Bulk Temp-38, Surface Temp ~100	1.6	1.6×10^5	Surface Temp ~260
	1000	1.7×10^{18}	4.6	5.7×10^4		1.8	2.1×10^5	
	2500	4.3×10^{18}	4.6	7.1×10^4		1.8	2.8×10^5	
60	500	1.6×10^{18}	3.5	3.5×10^4	Bulk Temp-~44, Surface Temp. ~120	1.7	1.6×10^5	Surface Temp. 260-295
	1000	3.2×10^{18}	5.2	3.9×10^4		1.6	1.8×10^5	
	2500	8.1×10^{18}	6.6	7.3×10^4		2.1	1.7×10^5	
120	500	4.3×10^{18}	Only Few Blisters of 3-5.5μm in dianeter in the entire bombarded area.		Bulk Temp ~70, Surface Temp ~280	No Blisters Detected		Surface Temp. 360-400
	1000	8.7×10^{18}						
	2500	2.2×10^{19}						

In order to see that this observed reduction in blistering is, in fact, due to higher target temperatures, several irradiations were done with target temperatures controlled at 300°C. Figures I-6a and I-6b show scanning electron micrographs of polycrystalline molybdenum surfaces irradiated at 300°C with 40-keV D^+ in continuous and pulsed modes, respectively, to a total dose of 2500 pulses or its equivalent. During continuous irradiation, the heating current was adjusted so as to keep the target temperature at $\sim$ 300°C. No blisters could be detected either for the continuous (Figure I-6a) or for the pulsed (Figure I-6b) irradiation, and the irradiated area does not appear to be different from the unirradiated area (Figure I-6c). Similarly, for 60-keV D^+ irradiation at 300°C, no blisters could be detected for both continuous and pulsed irradiation for a dose of 2500 pulses or its equivalent. These results are similar to those observed[15] for 150-keV H^+ irradiation of Mo, where blisters were observed for irradiation at temperatures below 100°C for doses of 6×10^{18} ions/cm^2, but no blisters were detected for irradiation at 400°C. This reduction in blistering in Mo at 300°C can be attributed in part to increased permeability of D^+ in Mo at 300°C compared to room temperature. The permeability of H_2 in Mo increases by more than two orders of magnitude with increase in temperature from room temperature to 300°C.[16] The trapping of D^+ by defects produced by irradiation appears to be negligible even at this temperature of 300°C. Thus, it appears that if the molybdenum surfaces can be maintained at 300°C or above, blistering due to D^+ irradiation can be reduced for the irradiation parameters studied here.

TZM-Alloy - D^+ irradiations of TZM alloy were performed only for a few selected energies and doses. Since very little blistering was observed for Mo irradiated with 120-keV D^+, the irradiation of TZM was done for only 40- and 60-keV D^+. Figures I-7a and I-7b show scanning electron micrographs of polycrystalline TZM irradiated in a continuous mode with 40-keV D^+ to a dose of 4.3×10^{18} ions/cm^2 (equivalent of 2500 pulses) and with 60-keV D^+ to a dose of 8.1×10^{18} ions/cm^2 (equivalent of 2500 pulses), respectively. For the 40-keV D^+ irradiation only a few blisters (estimated blister density $< 1 \times 10^3$ blisters/cm^2) could be seen over the entire bombarded area (Figure I-7a), whereas for the 60-keV D^+ irradiation, no blisters could be detected (Figure I-7b). Figures I-7c and I-7d show micrographs of TZM surfaces irradiated in the pulsed mode for 2500 pulsed with 40- and 60-keV D^+, respectively. For both 40- and 60-keV irradiations, only a few blisters (estimated density of $< 3 \times 10^3$ blisters/cm^2) were observed over the entire irradiated area. Comparing these results with those obtained for Mo (see Figures I-4a, I-4b, I-4d and I-4e), one can see that blistering is reduced in TZM alloy for both pulsed and continuous irradiation with 40- and 60-keV D^+. The largest blister diameter observed for TZM irradiated with 60-keV D^+

---

[15] G. J. Thomas and W. Bauer, J. Nucl. Mat. 53, 134 (1974).

[16] R. W. Roberts and T. A. Vanderslice in Ultrahigh Vacuum and its Applications, Prentice-Hall, Inc., N.J., p. 110 (1963).

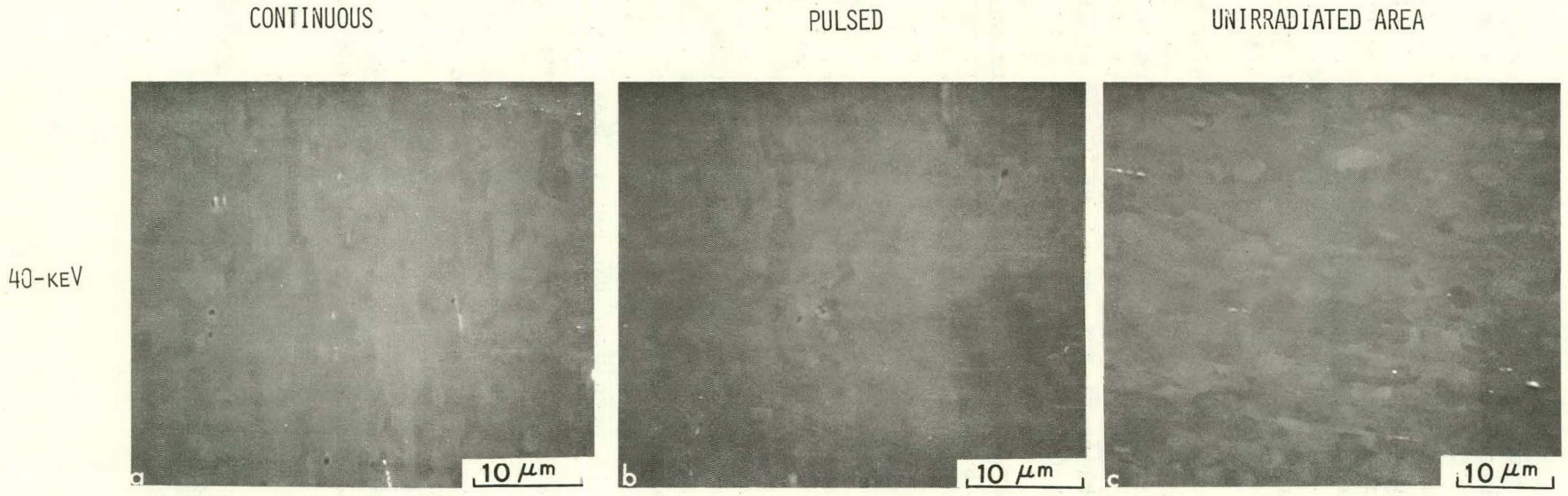

Figure I-6. SEMs cf polycrystalline Mo irradiated at 300°C for a dose of 2500 pulses or its equivalent (a) with 40-keV D^+ in continuous mode; (b) with 40-keV D^+ in pulsed mode; (c) an unirradiated area of the target surface.

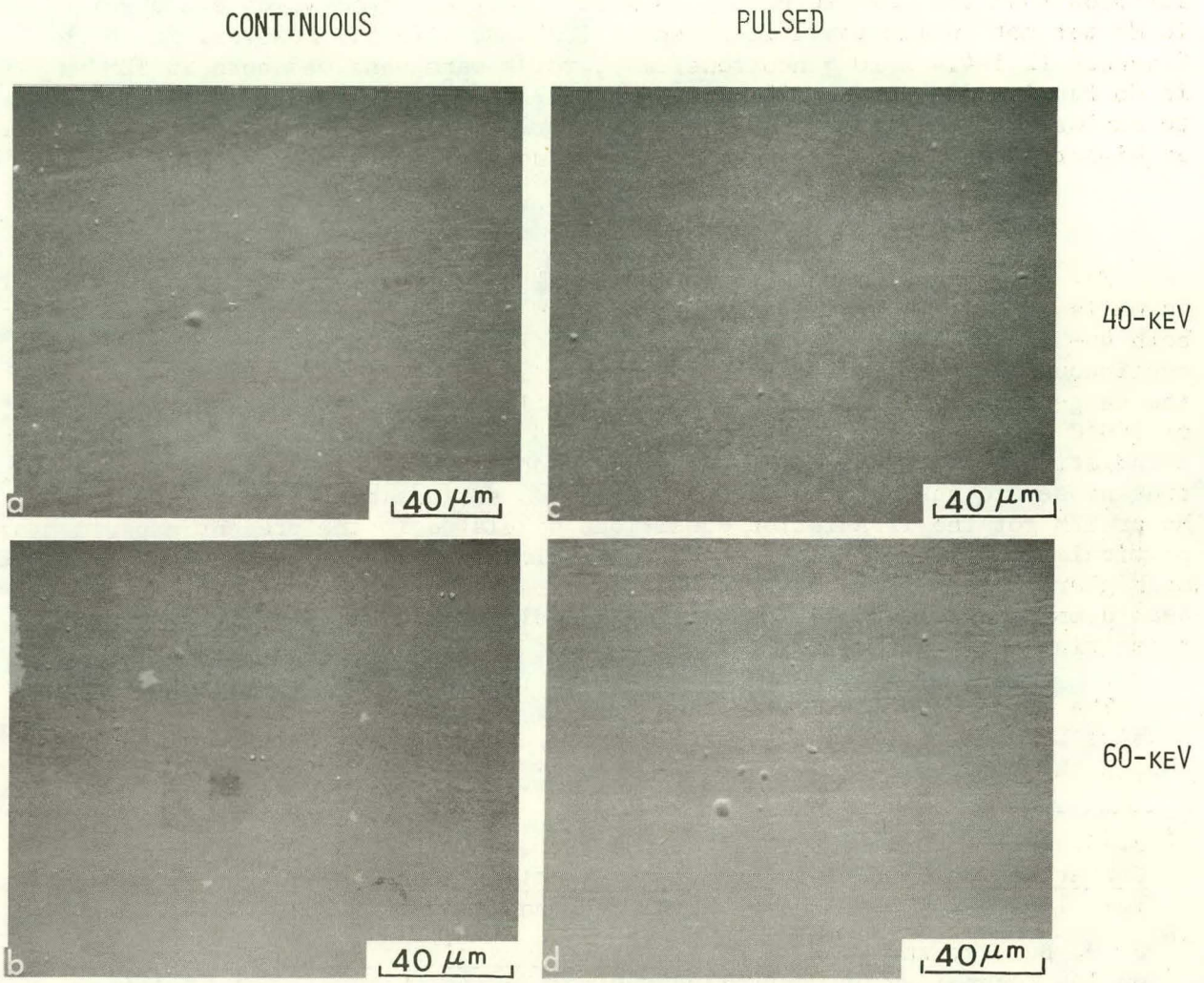

Figure I-7. SEMs of polycrystalline TZM alloy irradiated to a dose of 2500 pulses or its equivalent with (a) 40-keV D^+ in continuous mode; (b) 60-keV D^+ in continuous mode; (c) 40-keV D^+ in pulsed mode and (d) 60-keV D^+ in pulsed mode.

in a pulsed mode is only ∿ 9 μm as compared to ∿ 20 μm for the case of Mo irradiated under similar conditions. The reason for this reduction in blistering in TZM alloy as compared to Mo is not clear at present but it may be related to the increased yield strength of TZM as compared to molybdenum. Some recent studies[17] on void swelling in neutron irradiated Mo and TZM show that for low fluences (1.3×10^{20} neutrons/cm^2) voids are observed in Mo but not in TZM for irradiated at 1023 and 1123 K. However, for high fluences ($2.5\text{-}4.4 \times 10^{22}$ neutrons/cm^2), voids were observed both in TZM and in Mo for irradiation at 858, 1063, and 1273 K.[18] It appears desirable to explore if the difference in blister formation in TZM and Mo will disappear at higher doses than those used in the present experiments.

c. Conclusions

For the same deuteron energy and total dose, the average blister diameter in Mo is smaller for continuous irradiation than for pulsed irradiation for both 40- and 60-keV D^+ irradiation. This difference between the pulsed and continuous modes of irradiation appears to be related to the difference in the target temperatures during the irradiations. For target temperatures of 300°C or above, no blisters are observed in either pulsed or continuous irradiation. On the basis of the results obtained for Mo and TZM, it appears that no severe surface erosion will be expected in a beam dump made out of Mo or TZM for the irradiation conditions simulated in the present experiments; particularly if the surfaces can be maintained at elevated temperatures (300°C or higher). Based on limited results, TZM appears to be a better choice as a beam dump material, since for similar irradiation conditions, it showed less blistering than molybdenum.

The authors would like to thank Dr. J. L. Cecchi of Princeton Plasma Physics Laboratory for the initial encouragement and for helpful discussions during the course of these studies.

---

17 J. H. Bentley, D. L. Eyre, and M. H. Loretto, Proceedings of International Conference on Radiation Effects and Tritium Technology for Fusion Reactors, Vol. 1, J. S. Watson and F. W. Wiffen (eds.) CONF-750989, (1976), p. 297.

18 J. H. Bentley and F. W. Wiffen, Proceedings of the Second Topical Meeting on The Technology of Controlled Nuclear Fusion, Vol. 1, G. L. Kulcinski, (ed.) CONF-760935, (1976), p. 209.

3. Ion Nitriding of Titanium and Zirconium by a D.C. Discharge Method

Ming-Biann Liu, D. M. Gruen, A. R. Krauss, A. H. Reis, Jr., and S. W. Peterson, Chemistry Division

Virtually no data exist on the plasma impurity release properties of metal nitrides. The potential for lowering the effective Z of metal first walls together with an attendant lowering of the total sputtering yield of the nitrides compared with the metals makes a study of nitride coatings of interest from the point of view of impurity control. An added incentive to work on nitride coatings is the higher ion sputter yields anticipated for these materials.

The work in our laboratory is directed at developing methods for producing nitride coatings in situ at rates that are of practical interest. Furthermore, we are making measurements of plasma impurity release rates on these materials.

In recent work, we have found that the kinetics of metal nitride formation is enhanced by about a factor of three in the dc discharge technique compared with either rf discharge or thermal nitriding methods.

Nitrided surfaces of titanium and zirconium have been prepared by operating a dc glow discharge in a mixture of 20% N_2 and 80% H_2 at 20-40 torr. The discharge was confined between a stainless steel anode and the sample at ca. 500 ma with a dc potential of 360-400 V. The temperature of the sample was ca. 900°C.

The golden-yellow nitrided surfaces were characterized by energy-dispersive X-ray and electron diffraction techniques. The results show that the nitrided surfaces contain mononitride phases. Depth profile measurements were performed by argon ion etching and surface analysis by means of XPS.

Metallographic Observation - A micrograph of the cross section of the nitrided titanium disk, which was later examined by electron diffraction, is shown in Figure I-8. The 40 μm thick nitride layer may be readily distinguished. Similarly, a micrograph of the cross section of a nitrided zirconium disk (Figure I-9) shows that 43 μm thick nitride layer formed after 16 hr nitriding.

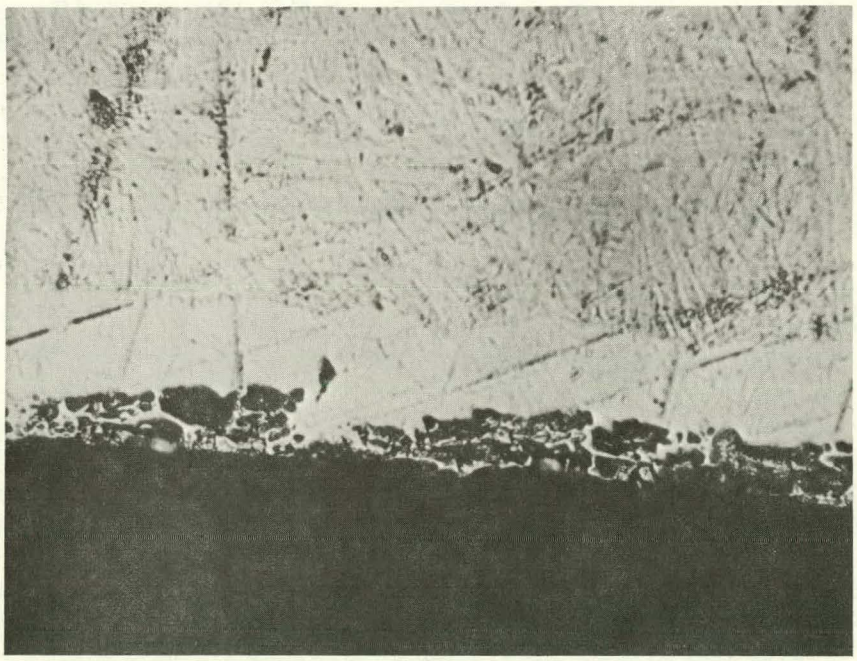

Figure I-8. A micrograph of the cross section of the nitrided titanium (nitriding time 810 min), x 500.

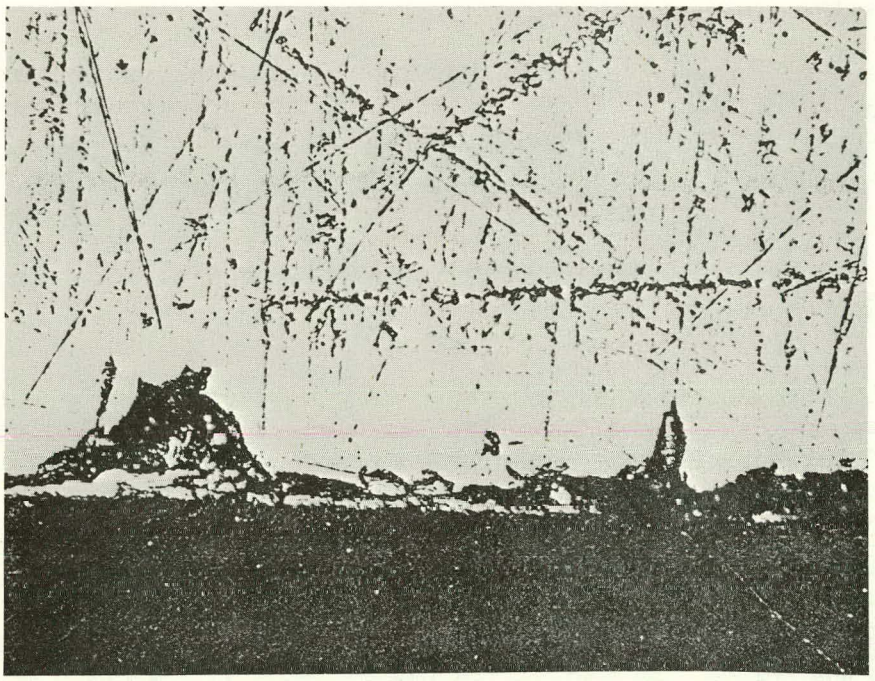

Figure I-9. A micrograph of the cross section of the nitrided zirconium (nitriding time 960 min), x 500.

Energy-Dispersive X-ray Analyses - Figures I-10a and I-10b show the X-ray diffraction spectra of the titanium surfaces and the nitrided surface of titanium described previously; both were taken with $2\theta = 16.95°$, a resolution of 56 eV/channel, and a counting time of 800 s. Figures I-11a and I-11b show the diffraction spectra of zirconium and nitrided zirconium with nitriding time of 315 min, $2\theta = 12.95°$, a resolution of 28 eV/channel, and a counting time of 2000 s. An instrumental background peak appeared on all the spectra.

Fluorescent emission lines were observed on both spectra in I-11 and were used to calibrate the energy scale. Intensities of the Ti K series emission lines decreased after nitriding. This may indicate that the reaction took place primarily on the near-surface of the titanium disk.

It can be seen from Figure I-11 that the Ti(110) diffraction peak is the most intense after nitriding; the intensity is not a function of the orientation of the surface with respect to surface normal. This may be associated with thermal enhancement of recystallization during nitriding.

Figures I-10 and I-11 illustrate that new diffraction peaks appear after the disks have been nitrided. The d-spacings were calculated using Bragg's law,

$$d_{hkl} = \frac{6.199}{E \sin \theta} , \qquad (1)$$

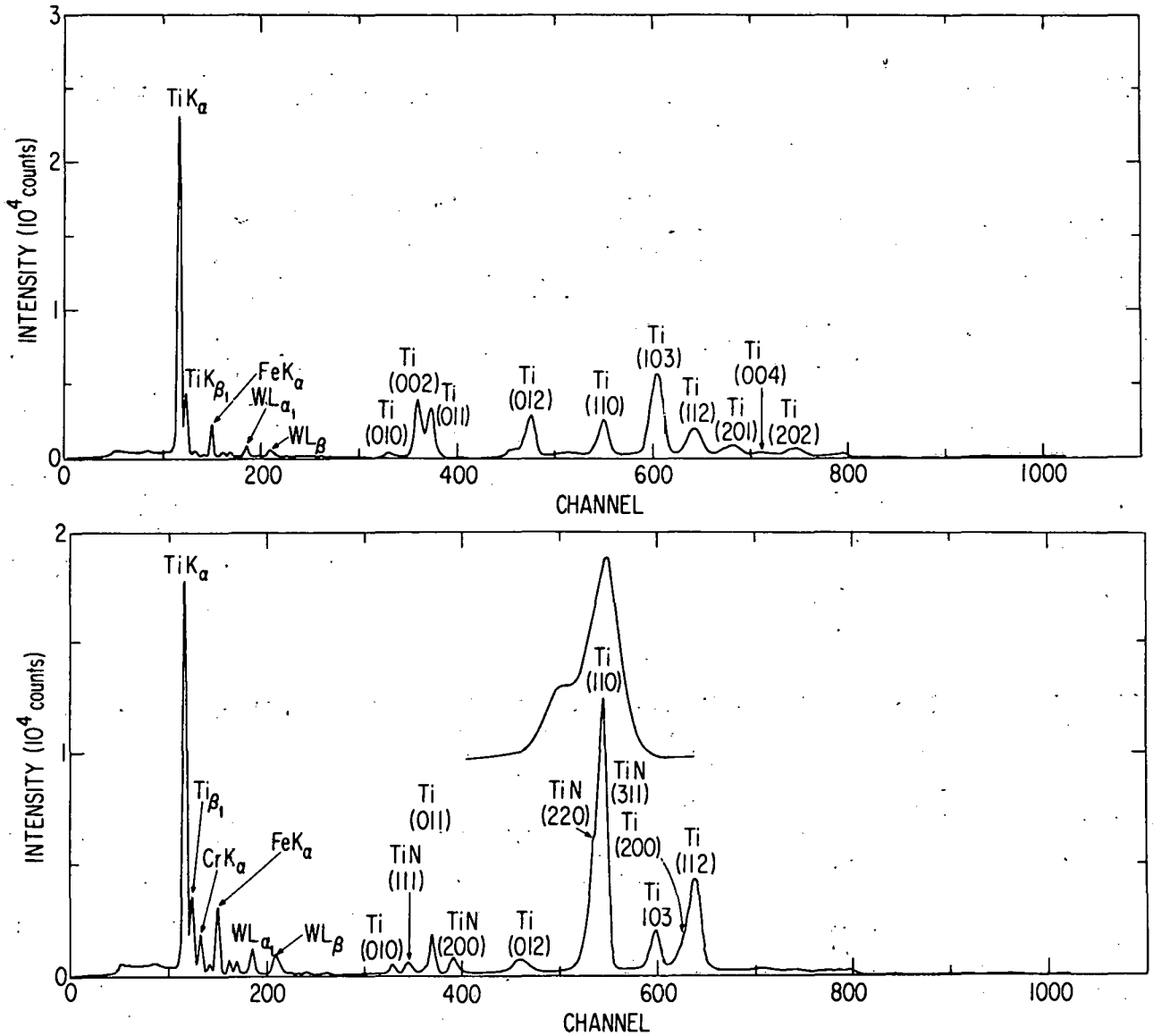

Figure I-10. (a) Spectrum of X-ray emissions and diffraction of titanium; (b) spectrum of X-ray emissions and diffraction of a nitrided titanium surface (nitriding time 810 min).

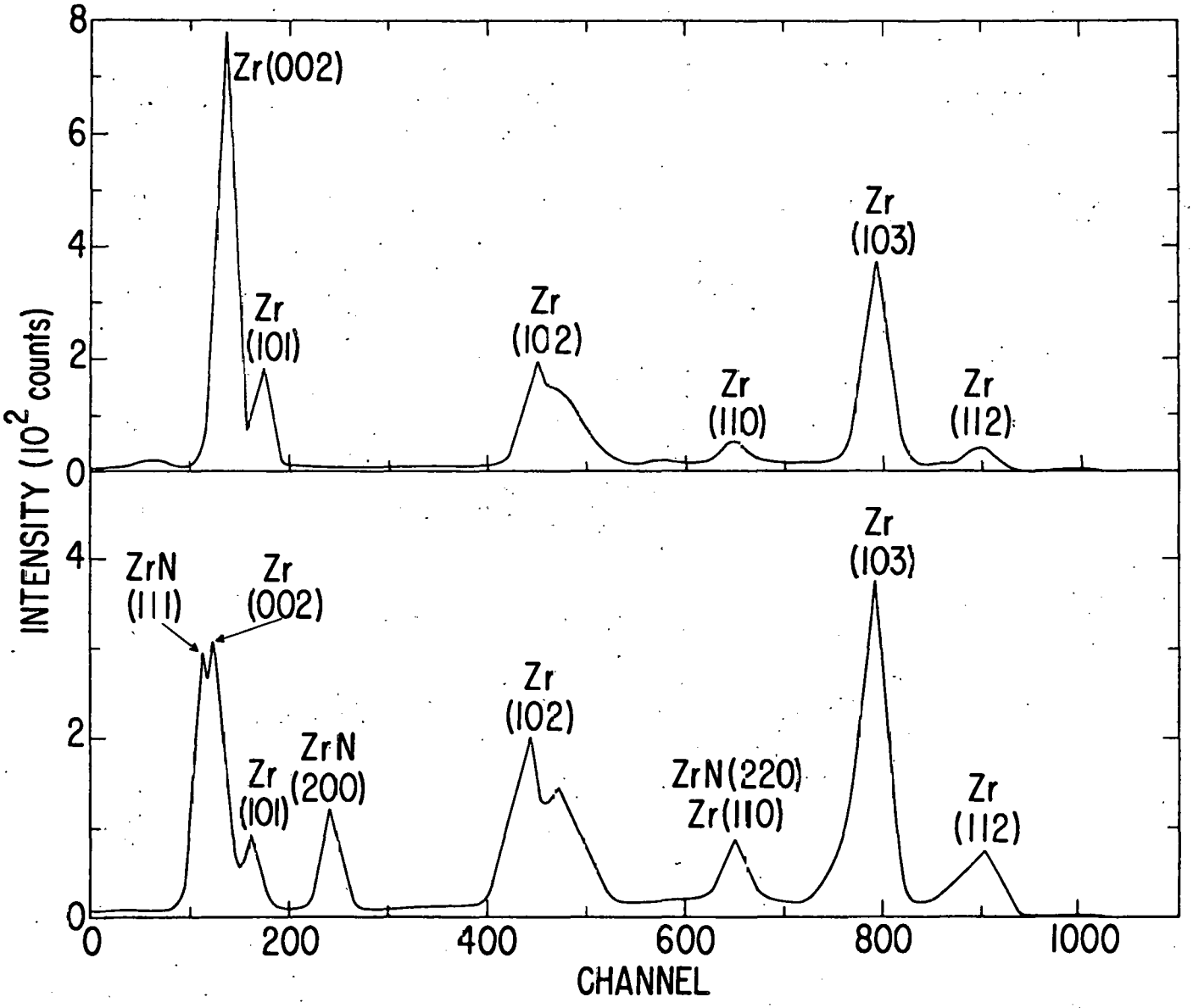

Figure I-11. (a) Diffraction spectrum of zirconium surface (top); (b) diffraction spectrum of nitrided zirconium surface (nitriding time 315 min) (bottom).

where energy, E, is in keV and d-spacing with index hkl, d_{hkl}, is in Å. The calculated d-spacings are 0.8% higher than those given in the ASTM files. The agreement is considered to be satisfactory since errors caused by misalignment and X-ray penetration into the sample are difficult to correct and may be large in magnitude; probably larger than errors arising from energy calibration. The errors caused by misalignment and X-ray penetration into the sample can be reduced by calibration using an internal standard. Since both diffraction peaks of metal and its nitride are contained in the same spectrum, the metal peaks can serve as suitable standards. The d-spacings of zirconium nitride were calculated using the d-spacings of zirconium given in ASTM file as the standards, and are in good agreement with those given in the ASTM file of zirconium nitride.

Electron Diffraction Analyses - Electron diffraction patterns were obtained by focusing electron beams on thin metal and nitrided metal foils. A titanium pattern was used as the standard for analyzing a diffraction pattern taken on the portion of the nitrided titanium foil which contains TiN. Again, the calculated d-spacings of TiN are considered to be in good agreement with those given in the ASTM file.

Depth Profile Measurements - A depth profile of plasma-nitrided titanium (Figure I-12) shows that the surface region is not the mononitride observed in the bulk by X-ray diffraction. Instead, there is a nitrogen-rich region in the first 400-600 Å with a composition TiN_x with $x \sim 2$. In this region the level of impurity oxygen is depressed. At depths greater than 600 Å, the oxygen concentration returns to a level more characteristic of polycrystalline foil which has been exposed to air and not subsequently outgassed. At the same time, the N/Ti ratio drops to about half its initial value and remains relatively constant throughout the remainder of the 4500 Å layer analyzed. The data suggests that the excess nitrogen near the surface is accommodated by interstitial oxygen displacement rather than the formation or a distinct higher nitride phase.

The results of the X-ray analyses and the electron diffraction experiments carried out in this study confirm that metal mononitride phases were produced for titanium and zirconium by ion nitriding. The dc discharge method appears to give superior nitriding rates than either the rf discharge or thermal nitriding methods. Future work will be directed to extending these results to Nb, Mo, V and Be.

B. Dosimetry and Damage Analysis Work in Support of the MFE Materials Program

L. R. Greenwood and R. R. Heinrich, Chemical Engineering Division

1. Neutron Dosimetry

a. Characterization of the $^9Be(d,n)$ Environment at the U.C. Davis Cyclotron at E_d = 30 MeV

A joint experiment was conducted in late July at the University of California at Davis Cyclotron involving our group, M. Guinan of Lawrence Livermore Laboratory, and H. Farrar IV and D. Kneff of Atomics International.

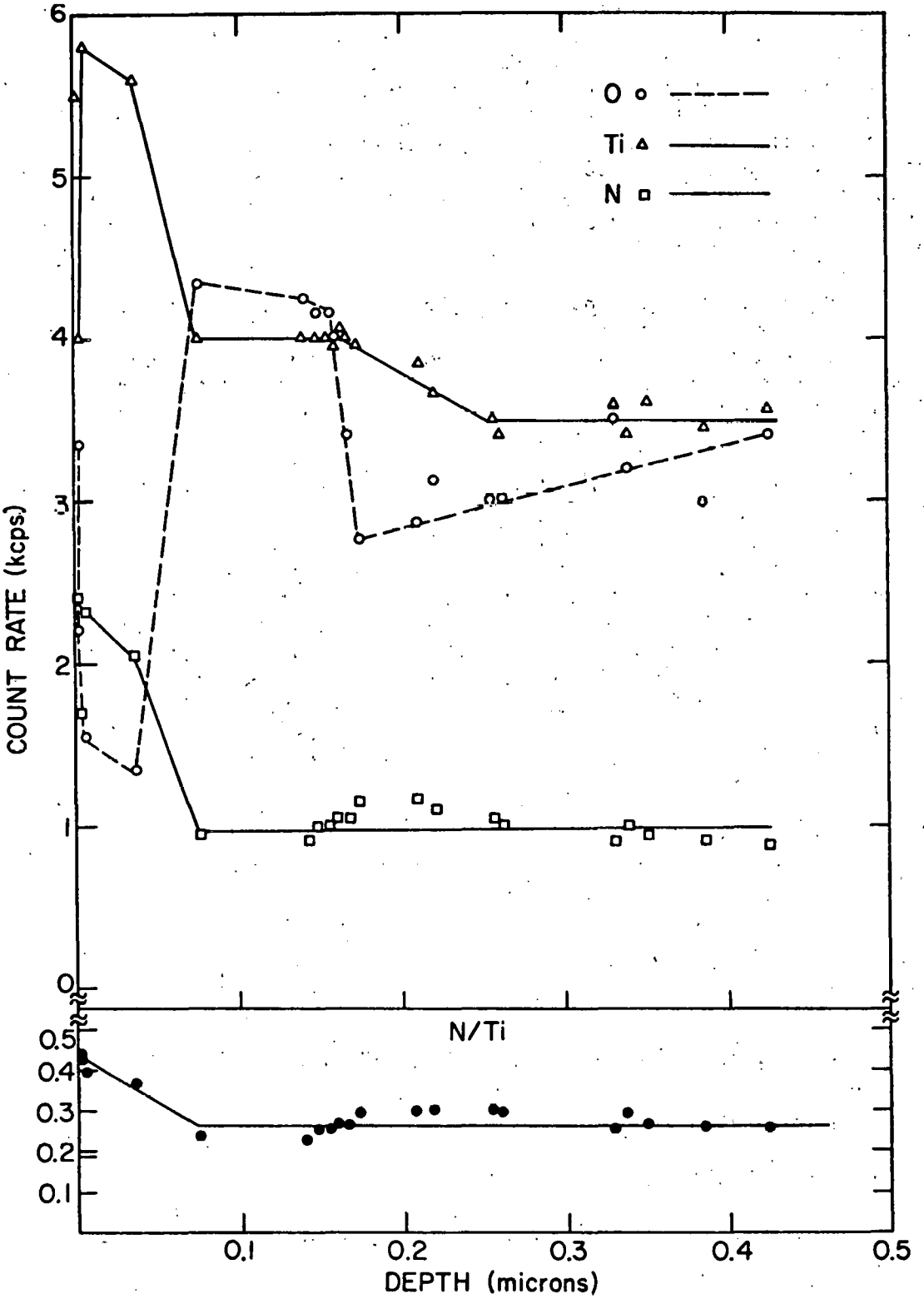

Figure I-12. Depth profile of nitrided titanium disk.

The purpose of the experiment is to extensively map the neutron flux and spectra produced by stopping a 30 MeV deuteron beam in a thick beryllium target. Foil packets and helium accumulation monitors were placed at a variety of locations and angles from the end of the beam stop out to 30 cm. Inducted activities with short half-lives were gamma counted at LLL and all others are now being analyzed at Argonne. The results will be used to unfold the neutron fields using the SAND II code.

Another experiment at U.C. Davis was also initiated in April. D. Styris of Pacific Northwest Laboratories irradiated tensile specimens (wires) in very close proximity to the beam stop in order to maximize the neutron fluence. We designed a foil packet which was segmented for Ge(Li) counting in order to obtain as fine a flux map as practical. Counting is complete and spectral analysis is now being done.

b. Characterization of the $^{9}Be(d,n)$ Environment at the ORNL Cyclotron at E_d = 40 MeV

A joint experiment with M. Saltmarsh of the Oak Ridge National Laboratory was conducted in June 1976 at the ORNL cyclotron. The purpose of the experiment was to determine the neutron flux and spectra in a well defined geometry for comparison with previously measured time-of-flight results. In this way we hope to assess the accuracy of high energy neutron cross sections required for neutron dosimetry at accelerator-based facilities. In order to do this comparison we had to extend our dosimetry cross section files to 44 MeV using data which generally does not extend above 20-30 MeV. Preliminary results are highly encouraging in that most of the activation cross sections are found to roughly agree in the integral tests within 10-20%. Figure I-13 shows our preliminary results for the neutron spectra at 7.5 cm from the target at 0° for E_d = 40 MeV. The 90% sensitivity limits are shown for the activation reactions. The $^{54}Fe(n,p)\ ^{54}Mn$ reaction was rejected since we know that at least 30% of the activity comes from the $^{56}Fe(n,nd)$, (n,t), or (n,2np) reactions. By combining these results with previous data obtained at lower neutron energies we thus expect to derive a consistent foil set for routine dosimetry in high-energy neutron fields.

2. Damage Analysis

We have improved our capabilities for calculating damage parameters including displacement rates, PKA distributions, and gas production rates. The DISCS package has been updated to include the new materials manganese and lithium increasing our files to 21 elements. The spectrum averaging routine has been modified to print out the average damage energy and PKA energy both with and without the Lindhard cut-off. The PKA energy grid has also been expanded at low energies to provide more detailed distributions and improved accuracy.

We have also developed a new capability for calculating the errors associated with the damage parameters due to uncertainties in our knowledge of the neutron spectrum. The code SANDANL does a Monte Carlo error analysis of the unfolded neutron spectrum considering errors in the cross sections, foil activations, and starting solution. We have added a routine which calculates the variation in the spectral averaged damage parameters to these

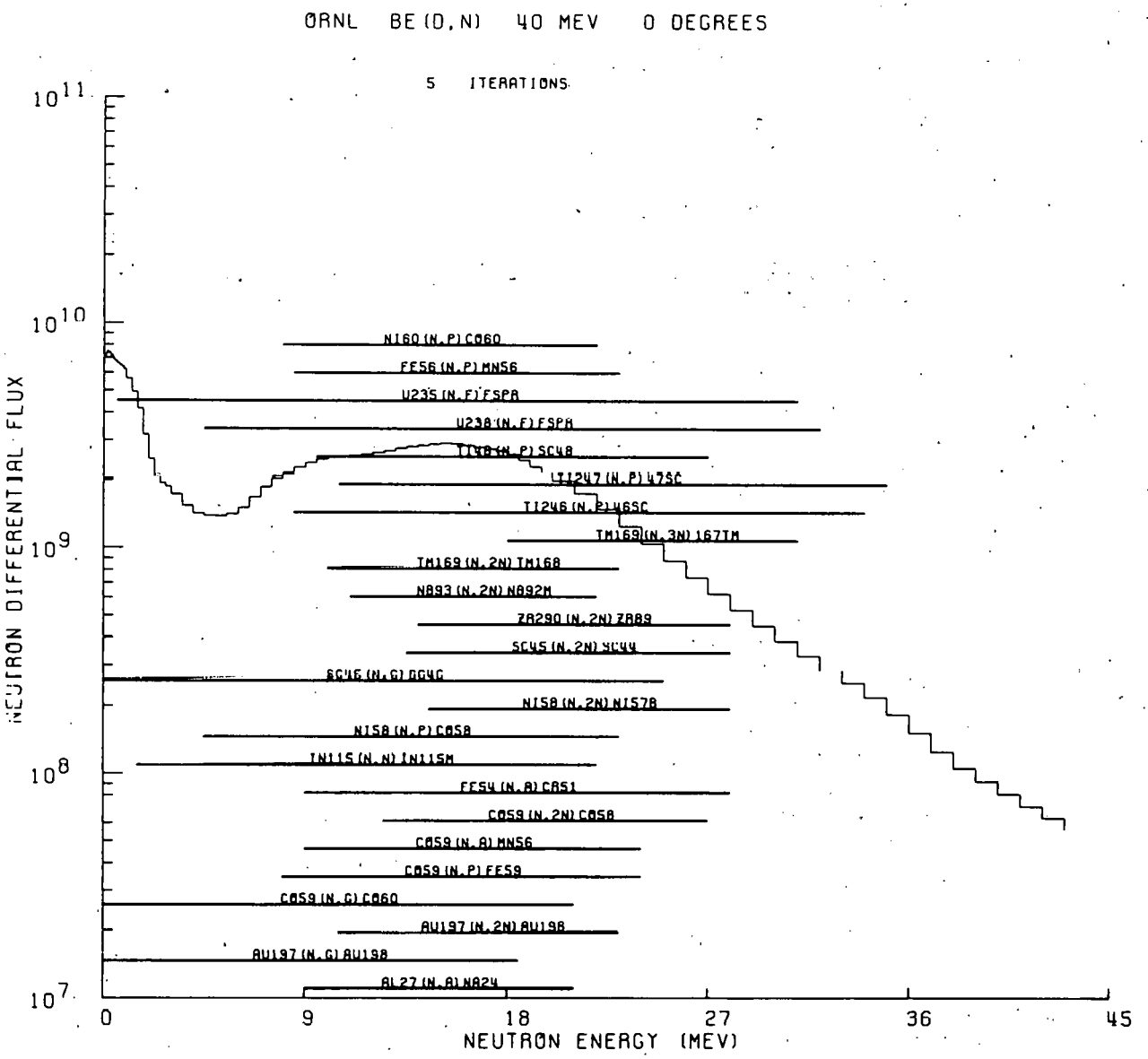

Figure I-13. The neutron spectrum generated by stopping the 40 MeV deuteron beam from the ORNL cyclotron in a thick beryllium target is unfolded with the SAND-II code. The 90% sensitivity limits are indicated for the 24 foil activation reactions.

uncertainties. This feature should be highly useful for making sensitivity studies of required dosimetry accuracies and for giving the experimenter a more practical feeling for the quality of an unfolded neutron spectrum. As an example, calculations for the VT53 ^{235}U converter in CP5 (T. Blewitt and M. Kirk, ANL) show that our previously reported spectral mapping leads to damage parameter errors of only 5-10%.

C. Alloy Development

1. Hydrogen Permeation and Materials Behavior in Alloys of Interest to the Fusion Power Program

Recent emphasis in this program[19] has been directed towards (1) studies of hydrogen permeation in representative austenitic and nickel base alloys as a function of temperature and hydrogen driving pressure and (2) construction of a small (∿ 1-liter capacity) stainless steel-clad vanadium alloy lithium loop. Progress in these two areas during the fourth quarter of FY-1977 is summarized below.

a. Hydrogen Permeation Studies

E. H. Van Deventer and V. A. Maroni, Chemical Engineering Division

A series of studies has been initiated to determine the hydrogen permeation characteristics of selected austenitic and nickel-base alloys over a range of driving pressures (10^{-3} to 10^{2} torr) and temperatures (200 to 800°C). The principal objectives of these studies are (1) to search for departures from square-root of pressure dependence and evaluate their causes, (2) to determine the effects of various impurity and radiation environments on permeation rates, and (3) to expand and augment the permeation data base for alloys that have been employed as substrates in our barrier development work and for materials that are of current interest to the fusion program in general. A comprehensive study of 321-SS (a previously used barrier substrate) has been completed and an investigation of Inconel 625 (the vacuum vessel material selected for Doublet III) is presently underway.

The permeation data measured for 321-SS are plotted in Figure I-14 together with the least squares refined curve obtained from the data of Rudd and Vetrano.[20] Log-log plots of permeation rate versus upstream hydrogen pressure are given in Figure I-15 for two separate temperatures. The half-power dependence on pressure is reasonably well obeyed over the studied

---

[19] W. M. Stacey, Jr., et al., Fusion Power Program Quarterly Progress Report, April-June, 1977, Argonne National Laboratory, ANL/FPP-77-2 (1977).

[20] D. W. Rudd and J. B. Vetrano, "Permeability of Metals and Enameled Metals to Hydrogen," Atomics International, NAA-SR-6109 (October, 1961).

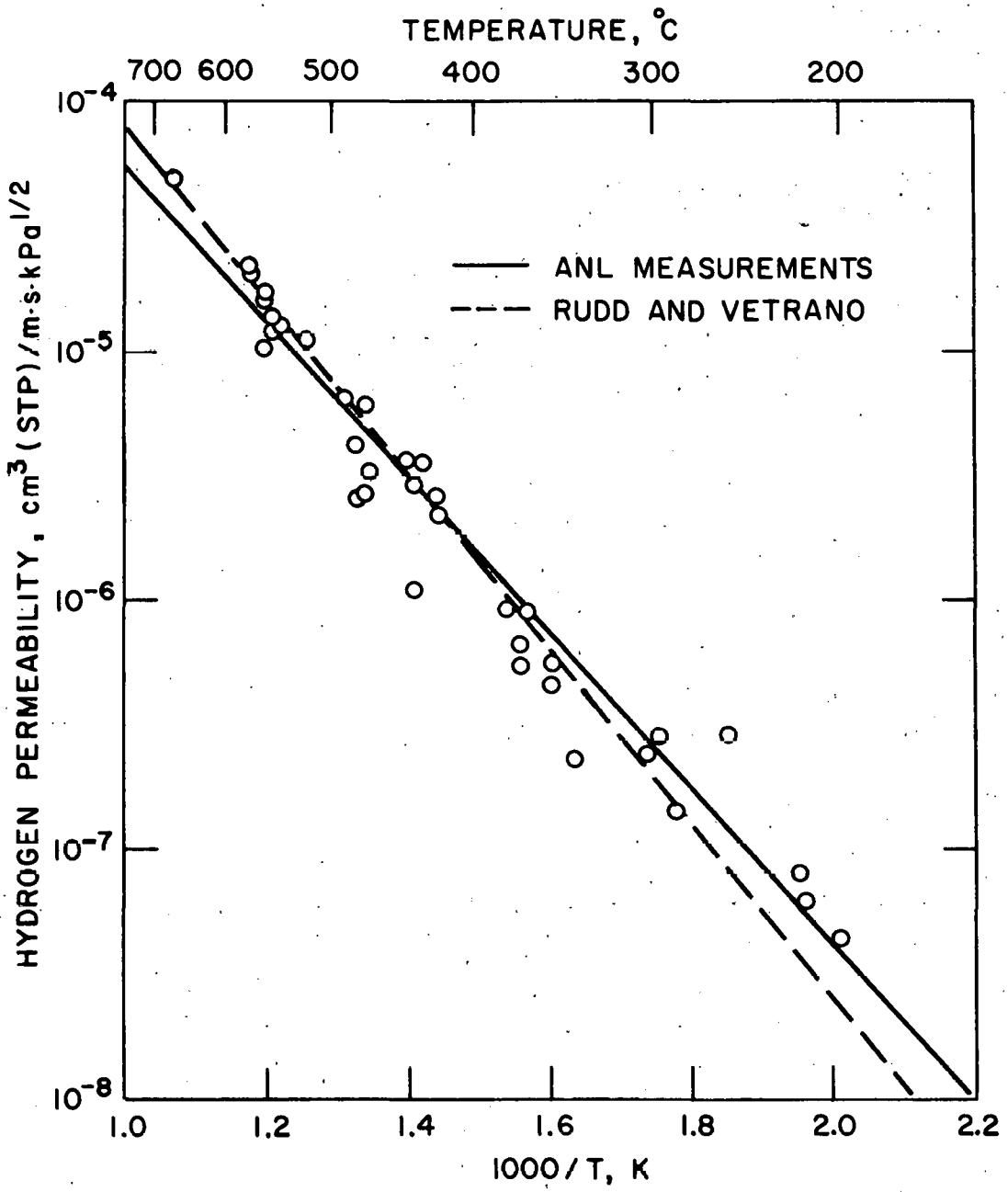

Figure I-14. A comparison of ANL Hydrogen Permeation Data for 321-SS with the extrapolated data of Rudd and Vetrano.[20]

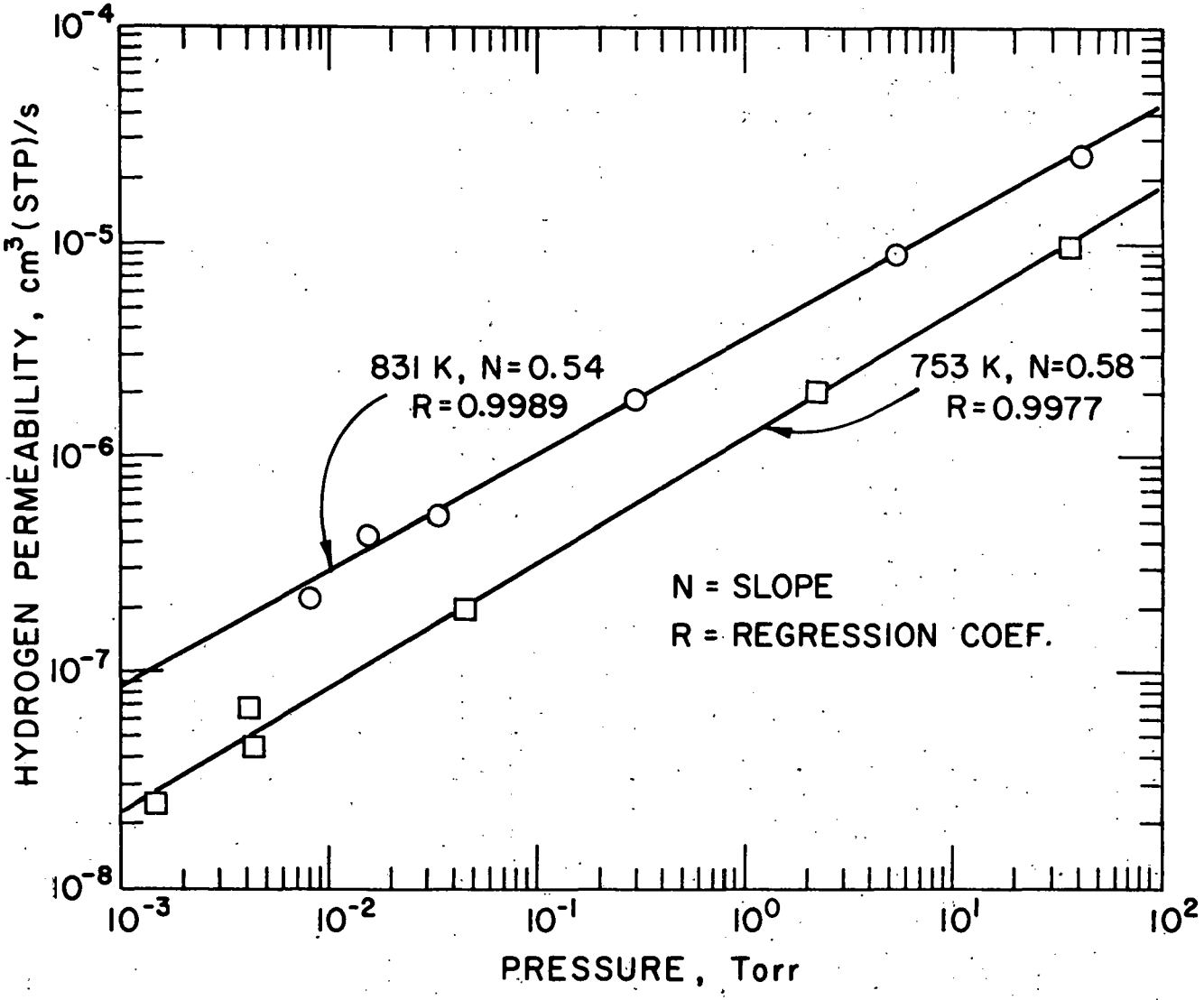

Figure I-15. Log-log plot of permeation rate versus upstream hydrogen pressure for 321-SS at 753 and 831°K.

pressure range at each temperature. The permeation equation derived from our data (assuming a half-power dependence over the entire temperature range of the study) is given by

$$\phi \left[\mathrm{cm^3(STP)/m \cdot s \cdot kPa^{\frac{1}{2}}}\right] = 6.733 \times 10^{-2} \exp(-14{,}198/RT)$$

An interesting observation was made during the course of the 321-SS study that is worthy of mention. Continuous monitoring of the upstream gas composition (using a partial pressure analyzer[19]) revealed that at low upstream hydrogen pressures water, CO/N , argon and helium combine to make a significant contribution to the total pressure in the upstream compartment. In some cases the molecular hydrogen partial pressure constituted as little as 20% of the total pressure. The point of this observation is that a total pressure measurement may not represent an accurate determination of the molecular hydrogen activity when the upstream pressure is relatively low. By applying continuous slow evacuation (with hydrogen makeup to maintain the H_2 pressure) using a throttled ion pump, it was possible to effect a moderate reduction of the fractional contribution of impurities to the total pressure. Use of a liquid nitrogen cold trap on the upstream compartment was somewhat less effective in this regard. More recently, we have been using a temperature controlled uranium hydride bed to regulate H_2 pressure. The presence of uranium metal in the upstream system causes a substantial reduction in the active gases (e.g., H_2O, O_2, N_2,

Permeation studies on the alloy Inconel 625 are nearly completed and will be reported on in a subsequent progress report. We are also investigating methods of incorporating 0.1 to 1.0 mCi alpha and/or gamma sources into our permeation assemblies,[21] as near as possible to the upstream and/or downstream faces of the sample membrane. Triplicate studies of a given sample would be carried out without, with, and again without the source(s) present in order to fully evaluate the effects of an ionizing radiation environment on permeation characteristics.

---

[21] E. H. Van Deventer, et al., J. Nucl. Mater. 64, 241 (1977).

b. Tests of Vanadium Alloy Performance in a Liquid Lithium Environment

D. L. Smith, Materials Science Division, and V. A. Maroni, Chemical Engineering Division

Selected vanadium-base alloys are of interest for fusion reactor blanket applications. Since information on the fabricability of vanadium alloys is sparse, a small lithium loop is being constructed of a vanadium-15% chromium alloy to investigate and assess certain fabrication procedures and to evaluate the integrity of the system under conditions of interest. An electromagnetic pump has been installed to circulate the lithium and a magnetic flowmeter will be used for flow measurement. The horizontal legs of the rectangular loop are 45 cm long and the vertical legs are 30 cm. An extension on one of the

vertical legs serves as a sample retrieval port. The vanadium alloy tubing (1.25-cm OD x 0.125-cm wall) was extruded from a billet by the Materials Science Division's Materials Processing and Development Group. The vanadium alloy tubing was expanded inside of a 1.56-cm OD x 0.125-cm wall Type 304 stainless steel tube to form a duplex tube. The stainless steel cladding serves to protect the vanadium alloy from atmospheric oxidation. The cladding was stripped from the vanadium alloy near the beveled ends to form joints as shown in Figure I-16(a). The beveled stainless steel couplings, which slide over the cladding, serve to protect the bared ends of the vanadium alloy tube. One of the vanadium alloy weld joints is shown in Figure I-16(b) prior to welding of the stainless steel coupling. Welding of the vanadium alloy was done in a helium glovebox by the TIG method, since this method is of practical interest. All four vanadium alloy joints have been successfully welded with little discoloration of the vanadium alloy surface and no detectable leaks at the welds. Sample welds of the vanadium alloy showed good weld penetration and weld toughness, although significant grain growth was observed in the heat-affected zone. In addition, a transition weld (TIG) from the vanadium alloy to stainless steel was successfully made at the top of the entry port.

2. Irradiation-Induced Void Swelling and Solute Segregation in a Heavy-Ion Irradiated V-15 wt % Cr Alloy

S. C. Agarwal, L. E. Rehn, A. Taylor, and F. V. Nolfi, Jr., Materials Science Division

A homogeneous single-phase V-15 wt % Cr alloy was prepared and irradiated at 650°C with 3.5-MeV $^{51}V^{+}$ ions to dose levels between 5 and 60 dpa. Voids were observed in the irradiated specimens over the entire range of doses studied. The computed swelling varied from 0.02% at 5 dpa to $\sim$ 20% at 60 dpa. The void size increased linearly as the dose increased from 76 Å at 5 dpa to $\sim$ 900 Å at 60 dpa. The observed swelling in the high-dose regime (30-60 dpa) is more than two orders of magnitude larger than for unalloyed vanadium from the same stock. Unalloyed vanadium contains a high density of precipitates after irradiation to high doses, whereas the present V-15 Cr alloy undergoes no precipitation during irradiation. A cellular dislocation structure, consisting of dense dislocation tangles separated by low dislocation density areas was observed at 5 dpa. The size of the dislocation tangles increased with dose to $\sim$ 30 dpa and remained unchanged at higher doses. Voids tended to be concentrated in areas where dislocation density was relatively low, i.e., in the regions away from the dislocation tangles. Auger spectroscopy of the irradiated specimens showed considerable solute enrichment near the surface, suggesting that Cr segregates to defect sinks during irradiation. These results provide the first experimental evidence of irradiation-induced solute segregation in bcc alloys.

3. Microstructural Development During Irradiation

B. Okray Hall and H. Wiedersich, Materials Science Division

A comprehensive time-dependent nucleation and growth model that includes dislocation loops, voids and helium bubbles is being developed to describe aspects of microstructural evolution in a metal during irradiation with

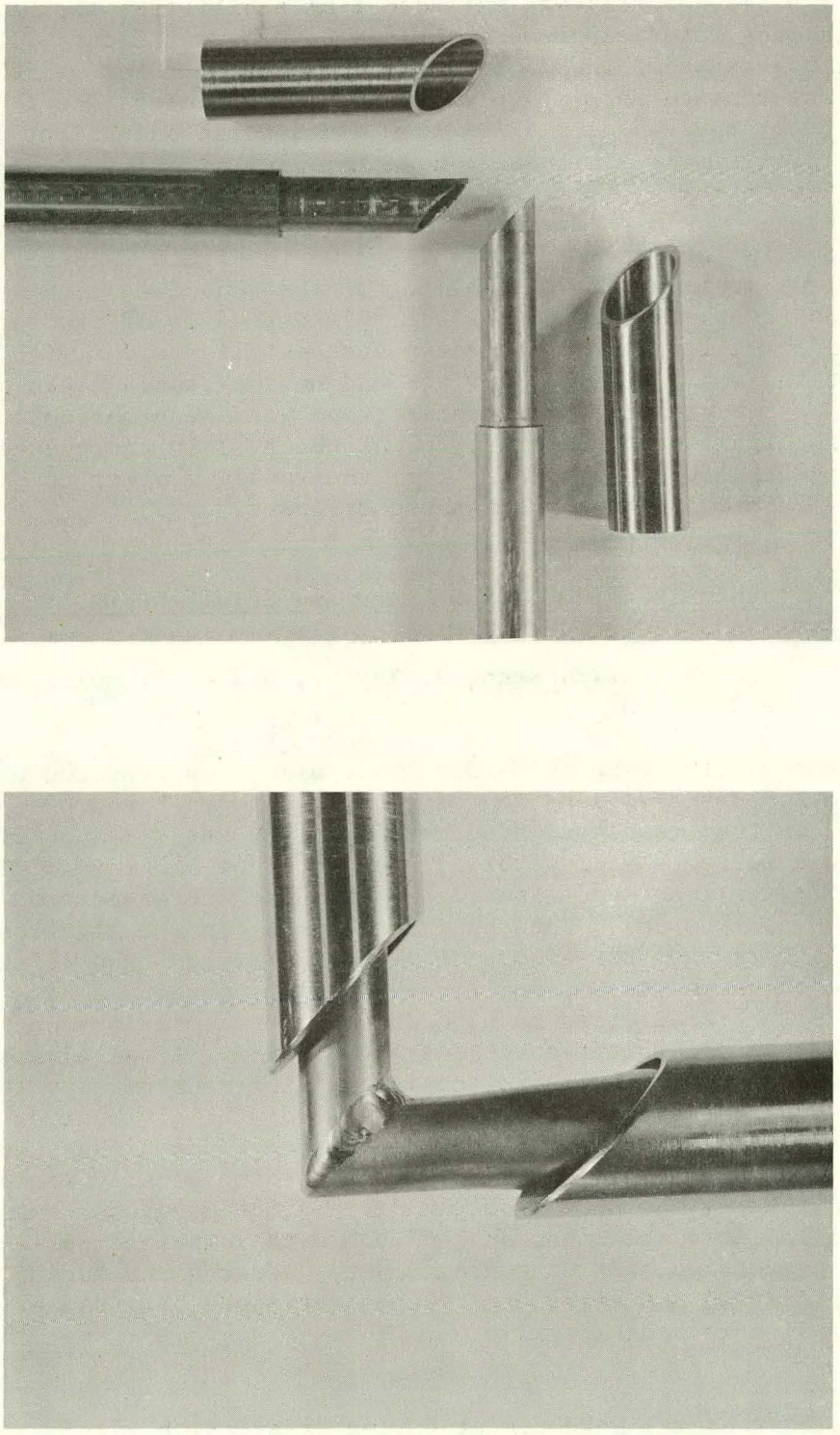

Figure I-16. Elbow of lithium loop constructed of vanadium alloy/stainless steel duplex tubing. (a) Before welding and (b) after TIG welding vanadium alloy.

simultaneous helium production. Results obtained using the first stage of the model, which treats interstitial loop nucleation, were presented in a previous report.[22] The model has been extended to include dislocation loop growth and the initial stages of vacancy clustering and void nucleation.

At the beginning of irradiation, the point-defect concentrations require time to establish quasi-steady-state values. In the temperature regime where recombination is important (below the swelling peak), the interstitial concentration peaks during the initial transient and then decreases to the steady-state value. When the maximum interstitial concentration is reached, the vacancy concentration is well below its steady-state value. Hence, the driving force for loop nucleation is very large and the formation of vacancy clusters is suppressed. As the vacancy concentration increases monotonically, the loss of point defects by recombination becomes significant and drives the interstitial concentration down, cutting off interstitial loop nucleation. At a dose of $\sim 10^{-5}$ dpa, loop nucleation is essentially complete and the loops grow during the remainder of the transient. During the loop growth stage, the vacancy and divacancy populations build up as shown in Figure I-17. By the time quasi-steady-state is reached, the loops are large enough to be visible in the electron microscope (Figure I-18).

[22] W. M. Stacey, Jr., et al., Fusion Power Program Quarterly Progress Report, January-March, 1977, Argonne National Laboratory, ANL/FPP-77-1 (1977).

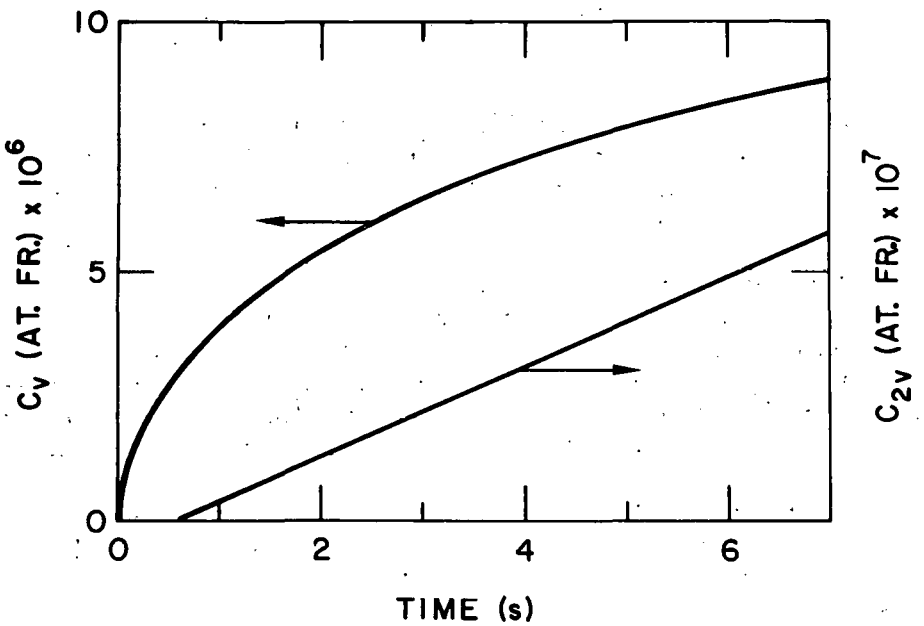

Figure I-17. Vacancy and divacancy concentrations as a function of time before quasi-steady-state is reached. (Loop-growth regime.) Irradiation parameters displacement rate $\dot{n} = 10^{-4}$ dpa-s^{-1}, T = 673°K, and sink-annihilation probability p = 10^{-6}.

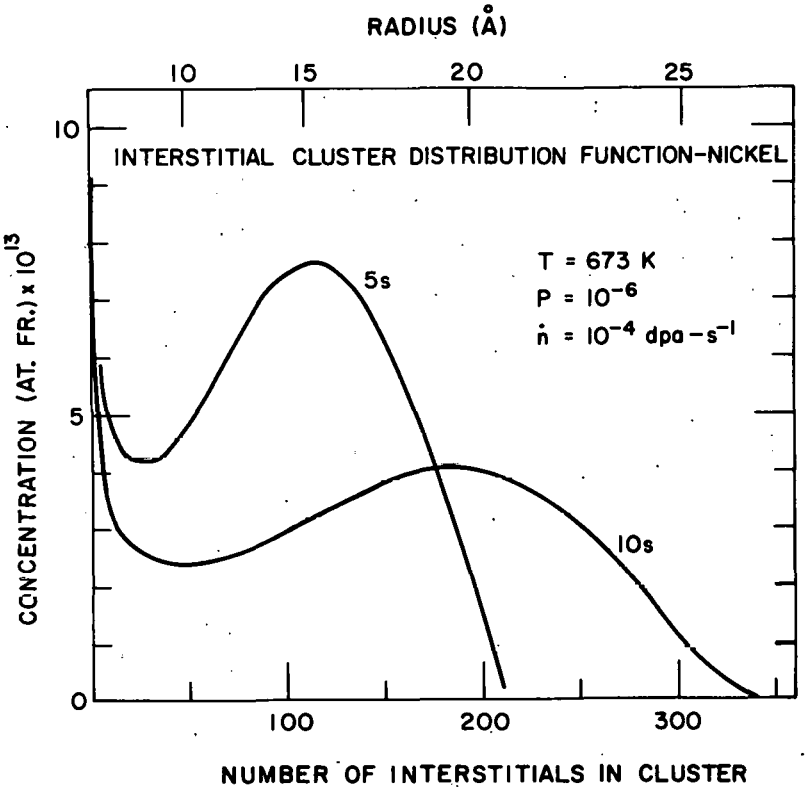

Figure I-18. Interstitial-loop distribution function as a function of the number of interstitials in the loop for two different irradiation times.

The model assumes the existence of a size-independent bias that favors interstitial over vacancy capture by loops. During the transient, the presence of the bias is unimportant, even though it enhances loop formation slightly. The bias does not become important until quasi-steady-state is approached; then the interstitial and vacancy fluxes become approximately equal, and the bias is essential for vacancy clustering and void nucleation.

An experiment designed to study nickel and several nickel alloys irradiated with Ni^+ ions to doses ranging from 0.001 to 0.6 dpa has been performed in cooperation with D. I. Potter under BES funding. The specimens are currently being examined.

4. Radiation Damage of Diagnostic Windows in TFTR

W. Primak, Solid State Science Division

At the request of the Princeton Plasma Physics Laboratory, a project has been initiated to assess radiation damage in diagnostic windows for use in the TFTR. The proposed windows are a vitreous silica disk 9 inches in diameter by 2 inches thick and a crystal quartz window with a clear 1 inch

aperture. Spectra of neutrons, hard and soft x-radiation, and tungsten emission (very soft X-rays) that are anticipated at the windows during operation have been supplied by K. Young of PPPL.

The primary objective of this investigation is a calculation of the stress to be anticipated from radiation-induced dilatation to assess the danger of mechanical failure. The vitreous silica window is for use in optical diagnostics, hence the optical absorption is also of concern.

Initially, the dose was calculated for each spectrum. By combining experimental data from reactor exposures, electron bombardments and gamma ray irradiations, functions for the damage dependence on the dose were constructed, and by integration the total effects were obtained. It was estimated that the stresses caused by the neutrons and the hard X-rays would be of the magnitude 700 psi. How serious these would be would depend on applied stresses and the safety factor required in the design. Polarized light monitoring of the window was suggested. The differential stresses from the soft X-rays were over an order of magnitude greater and were more serious because their direction would make monitoring difficult. It was suggested that a thin cover slip be used with the window to shield the main structural element. Optical absorption of vitreous silica which had been exposed for a similar dose in CP-5 was measured. Absorption was high below 0.3 μ, but was low above 0.4 μ except for a small peak (10-20% absorption in the thickness of interest) in the vicinity of the red He-Ne laser emission.

The quartz window was investigated next. No data for quartz for the low dose involved were found. The closest data were from our laboratory, results obtained in the early 1950's and published in part. These were extrapolated to find the effects in quartz. Loss of crystallinity would be minimal for the neutrons, and hard and soft X-rays. Under the conditions stated, the dimensional changes would develop stresses similar to those found for the vitreous silica, but the problems of fracture would be different because quartz is a crystalline material. Instructions for selecting quartz suitable for the purpose was supplied.

The tungsten emission presented a special problem because the energy deposition in the surface layers of the windows would be some 60,000 cal/g sec. This is over an order of magnitude above what would normally be considered "safe". Its possible effects have not yet been evaluated.* Such absorption would be serious for any ceramic or insulating material that might be chosen for a window. While the luminescence expected from the other sources seemed to be small, it may be serious for this source.*

---

* This was evaluated in Primak to Price, 11/7/77.

II. EXPERIMENTAL POWER REACTOR

A. New Impurity Control Methods for EPR

J. Brooks, EPR Project

Previous EPR studies have developed the concept of using a low-Z coated first wall as an impurity control measure. Depending on the coating material used (e.g. Be, BeO, B_4C) and on the plasma edge temperature, a burn time of from 1-2 minutes can be achieved and a substantial amount of net electrical power can be produced. The low-Z coating technique, by itself, has an uncertain extrapolation to commercial fusion power reactors where a much longer burn time might be needed for economic operation. It has been generally felt that divertors would be used on post-EPR devices in order to achieve this end (low-Z coatings would still be required). Recent studies have been performed on two alternative impurity control techniques that may have significant potential. These are (1) a first wall having a helium retention capability and (2) a limiter-vacuum port system. The helium retention wall would work by retaining some fraction of the helium impinging on it during the plasma burn. It would have an effective reflection coefficient "R_α" less than unity. (The effective reflection coefficient includes the processes of outgassing and backscattering.) The importance of this coefficient can be shown by using the equation for helium buildup in the plasma:

$$\frac{dN_\alpha}{dt} = \frac{1}{4} < \sigma V > N_{DT}^2 - \frac{N_\alpha}{\tau_\alpha}(1 - R_\alpha)$$

The first term represents the production of helium by fusion and the second term is the loss of helium by diffusion to the walls. At equilibrium (assuming one could be reached), $dN_\alpha/dt = 0$ and the relative concentration of helium becomes:

$$\frac{N_\alpha}{N_{DT}} = \frac{F}{1 - R_\alpha} \frac{\tau_\alpha}{\tau_{DT}}$$

where F is the ratio of burn-up to transport, generally $F \approx 0.02$. For $R_\alpha = 1$, $N_\alpha = \infty$ since there is no sink. The concentration of N_α is thus extremely dependent on R_α for values of R_α near unity. The equilibrium concentration of wall sputtered impurity is also dependent on R_α because lower values of N_α result in less α sputtering. These conclusions are reflected in an analysis of the burn cycle performance of the ANL-EPR as a function of R_α, which is shown in Figure II-1. If no special steps are taken to reduce it, a value of $R_\alpha = 0.95$ is felt to be typical and this has been used in previous studies. The resulting burn time is about 1 minute. It is felt, however, that modest reductions in R_α are achievable (e.g. by driving out and pumping helium) between burn pulses).[1] If R_α can in fact be reduced to 0.85 or lower, then

[1] D. Smith, Materials Science Division, and S. D. Harkness, Fusion Power Program, private communication.

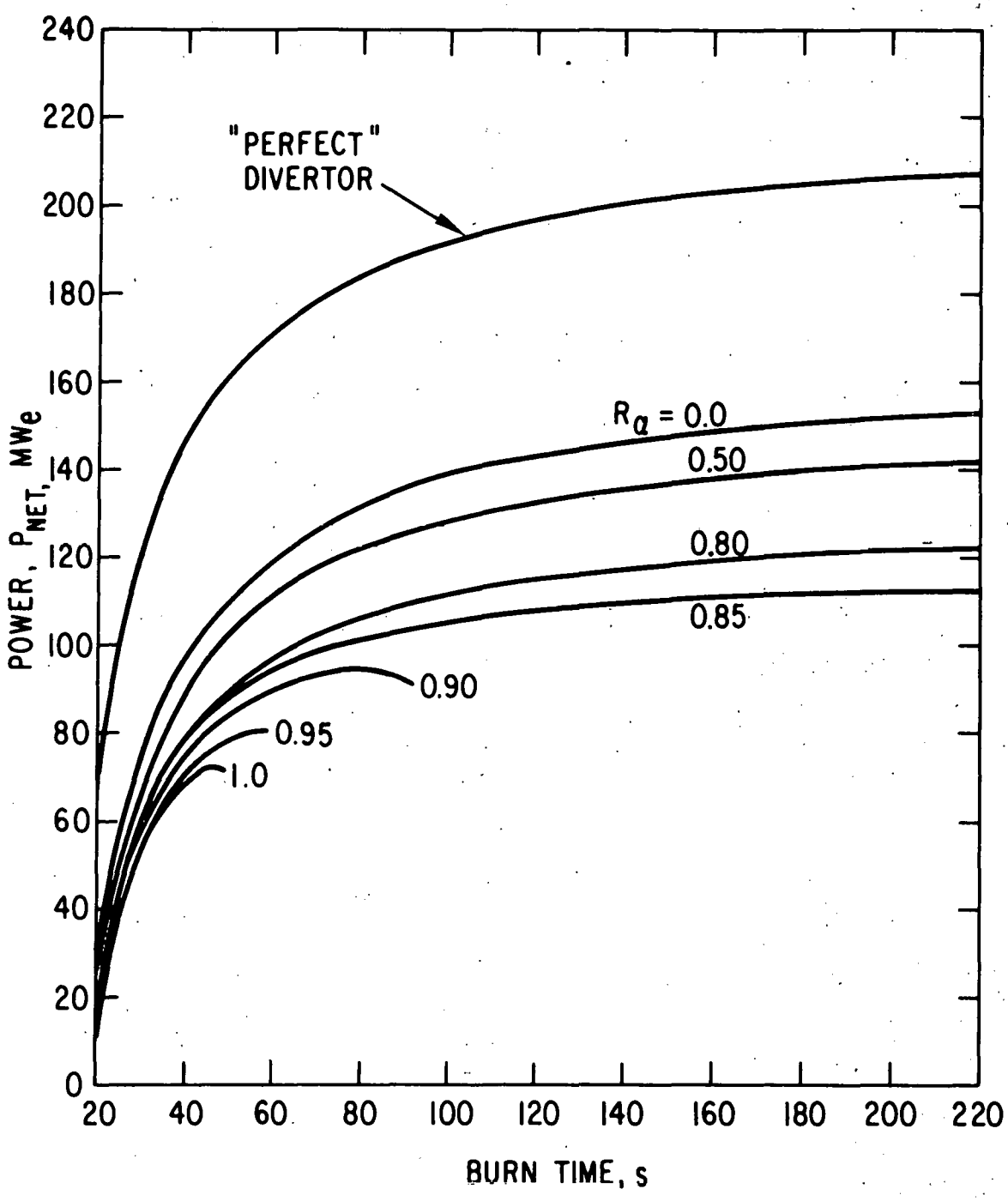

Figure II-1. Power performance of helium retention wall as a function of reflection coefficient.

the burn time becomes unlimited by impurities (it is still volt-second limited). Lowering R_α also increases the net power production because less DT is displaced, in the β-limited plasma, by He, Be ions, and their associated electrons. The power performance, for any R_α, is still less than that obtainable with a perfect divertor which reduces the N_α and N_{Be} concentrations to very low levels. Still, the long achievable burn time and the much easier implementation compared to a divertor, may make the helium retention technique look promising.

The idea of the limiter-vacuum system technique is to place vacuum ports near the limiter(s) in order to pump a high concentration of particles coming out of the plasma. This could not be done without limiters because too much of the wall area would have to be taken up with vacuum ports. Pumping during the burn effectively reduces the helium reflection coefficient as well as the DT and Be reflection coefficients, and also reduces the effective sputtering rate. The power performance of the ANL-EPR with one type of limiter-vacuum system is shown in Figure II-2. The parameter R_{DT} is the effective DT reflection coefficient and is equal to the fraction of DT ions hitting the limiter that scatter into the vacuum port. Since the pumping efficiency for helium is assumed to be only 60%, the effective helium reflection coefficient is always greater or equal to R_{DT}. A value of $R_{DT} = 0.80$ is required to achieve steady state operation. This appears to be a modest requirement in terms of achievable limiter geometries. As R_{DT} is reduced, significantly more power can be produced; the further reduction in helium density for $R_{DT} \lesssim 0.80$ is not significant but the reduction in Be is. The power performance for low values of R_{DT}, is similar (i.e. high pumping rates) to that obtainable with a divertor.

Both of these schemes offer the potential for greatly extending the burn time of an EPR by the use of relatively modest technology. Analysis is being continued on this subject to further define the requirements on these techniques.

B. Superconducting Magnet Systems for EPR Design

L. R. Turner, S-T. Wang, S. H. Kim, Y. C. Huang, and R. P. Smith, EPR Project

The magnet systems for the current Argonne experimental power reactor (EPR) design build on the earlier designs but incorporate a number of improvements. The toroidal field (TF) coil system consists of 16 coils of the constant tension shape, with NbTi, copper, and stainless steel as superconductor, stabilizer, and support material respectively. They are designed for 10 T operation at 3.7 K or 9 T operation at 4.2 K. Two changes from earlier designs permit a saving in material requirements. The coils are wound with the conductor in precompression and the support material in pretension so that when the coils are energized, the stainless steel experiences a stress of 60,000 psi while the copper stress does not exceed 15,000 psi. Both the copper and NbTi are graded, with higher current densities where magnetic and radiation effects are smaller.

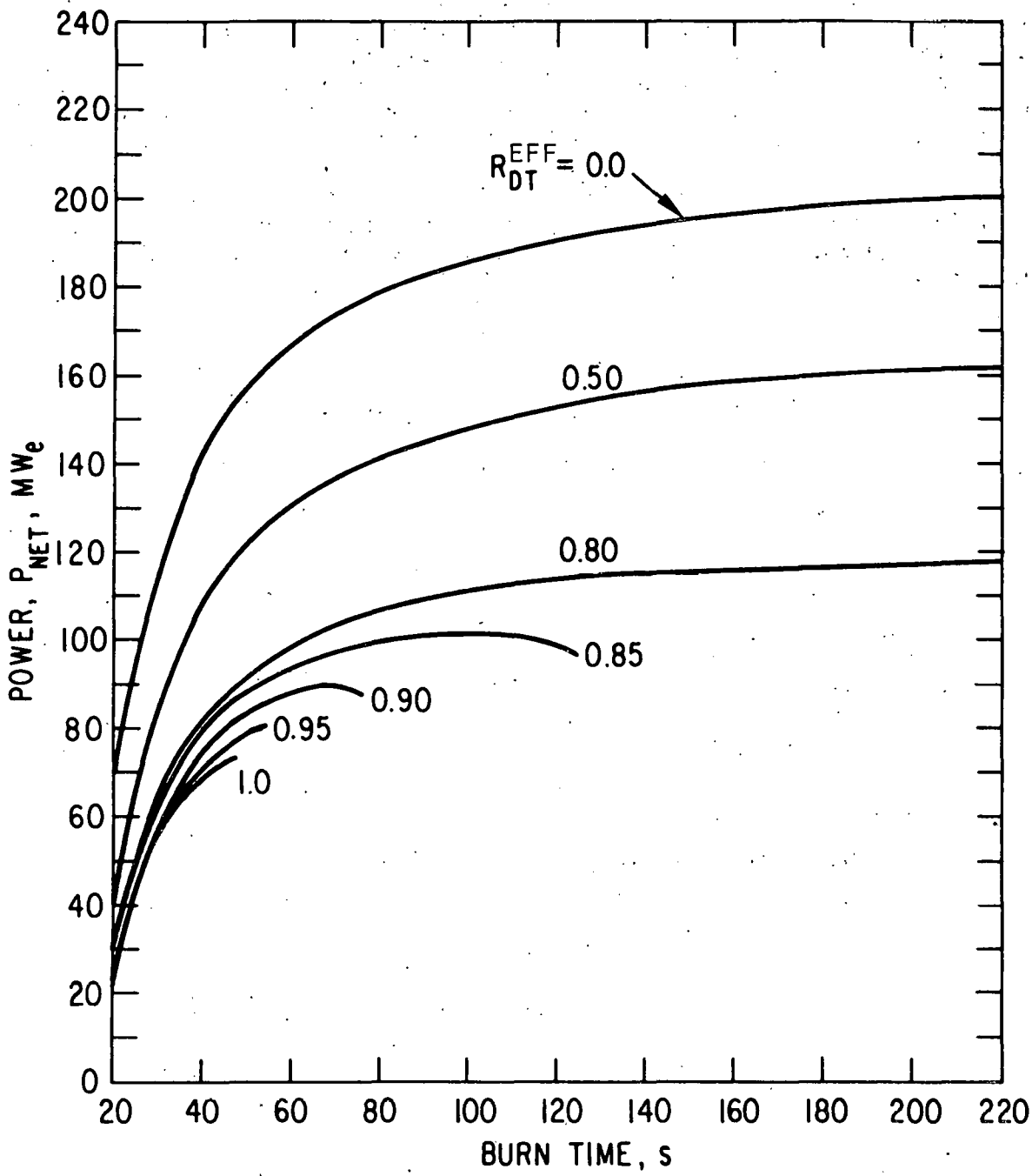

Figure II-2. Power performance of limiter-vacuum system for EPR, for different values of effective D-T reflection coefficient R_{DT}^{EFF} and with: $R_\alpha = 1 - 0.6\ (1-R_{DT})$, $R_z = 0.05$.

The ohmic heating (OH) coil system consists of a central solenoid plus ten other coils, all located outside the TF coils for ease of maintenance. The NbTi-copper coils are cryostable and operate at 4.2 K. The solenoid is segmented, with rings of insulation between segments to transfer the centering force from the TF coils to an insulating cylinder inside the OH solenoid. Locating the OH solenoid inside the support cylinder plus raising the central field to 8 T, enables the OH system to develop more volt-seconds (V-s) than the earlier designs, even though the plasma major radius is smaller.

The superconducting equilibrium field coils, also outside the TF coils, provide the field pattern required for a D-shaped plasma. Parameters for the TF coils and poloidal field (PF) coils are given in Tables II-1 and II-2. The magnet systems are shown in Figure II-3.

Table II-1. Toroidal Field Coil Parameters

Number of coils	16
Coil shape	Pure-tension D
Superconductor	NbTi
Stabilizer	Copper
Support material	Stainless Steel
Support cylinder	Fiberglass-reinforced plastic
Coil bore, vertical x horizontal	8.73 m x 5.64 m
Operating temperature	3.7 K (4.2 K)
Peak field	10 T (9 T)
Field at plasma	4.81 T (4.33 T)
Total amp-turns	115 MA-turns (104 MA-turns)
Operating current	60,000 A (54,000 A)
Turns per coil	60 x 2
Average current density	1540 A/cm^2 (1390 A/cm^2)
Inductance	7.9 H
Stored energy	14.3 GJ (11.6 GJ)

Table II-2. Poloidal Field Coil Parameters

	OH Coils	EF Coils
Number of coils	Solenoid + 10	12
Location	Outside TF coils	Outside TF coils
Superconductor/stabilizer	NbTi/Cu	NbTi/Cu
Operating temperature	4.2 K	4.2 K
Current density	1730 A/cm^2	1730 A/cm^2
Operating current	70 kA	70 kA
Total amp-turns	82.3 MA-turns	45.4 MA-turns
Maximum volt-seconds	90 V-s	37 V-s
Central field	8 T	0.3 T
Field at plasma	$< 10^{-3}$ T	0.56 T
Inductance	0.73 H	0.94 H
Coupling coefficient to plasma	- 0.25	- 0.175
Energy transferred	1.75 GJ	2.30 GJ
Inductive energy: OH, EF, and Plasma	3.75 GJ	

1. Ohmic Heating Coils

The OH and equilibrium-field (EF) coils are located external to the TF coils, to facilitate installation and maintenance and to allow them to be superconducting. The location of these coils is shown in Figure II-3, and the principal parameters are given in Table II-2.

The OH coils consist of a central solenoid and ten additional coaxial coils. The central solenoid is between the TF coils and the central support cylinder. This configuration maximizes the central flux core area for a solenoidal OH coil to provide the necessary volt-seconds. The OH coils are energized to give a negative flux before the plasma is formed then the current in the OH coils is reversed, inducing a current in the plasma.

The proposed TF coil support cylinder is made of a fiberglass-reinforced plastic such as G-10 or G-11. The cylinder is positioned inside the OH coil with axial support rings transmitting the load from the TF coils to the support cylinder as shown in Figure II-4. Each coil is 0.20 m thick, with 0.05 m between coils. Liquid helium is introduced to the bottom of the coils, and the gas is vented at the top of the coil. Both the liquid channels and the gas-venting channels are provided by micarta or G-10 strips, about 0.6 mm thick running radially outward.

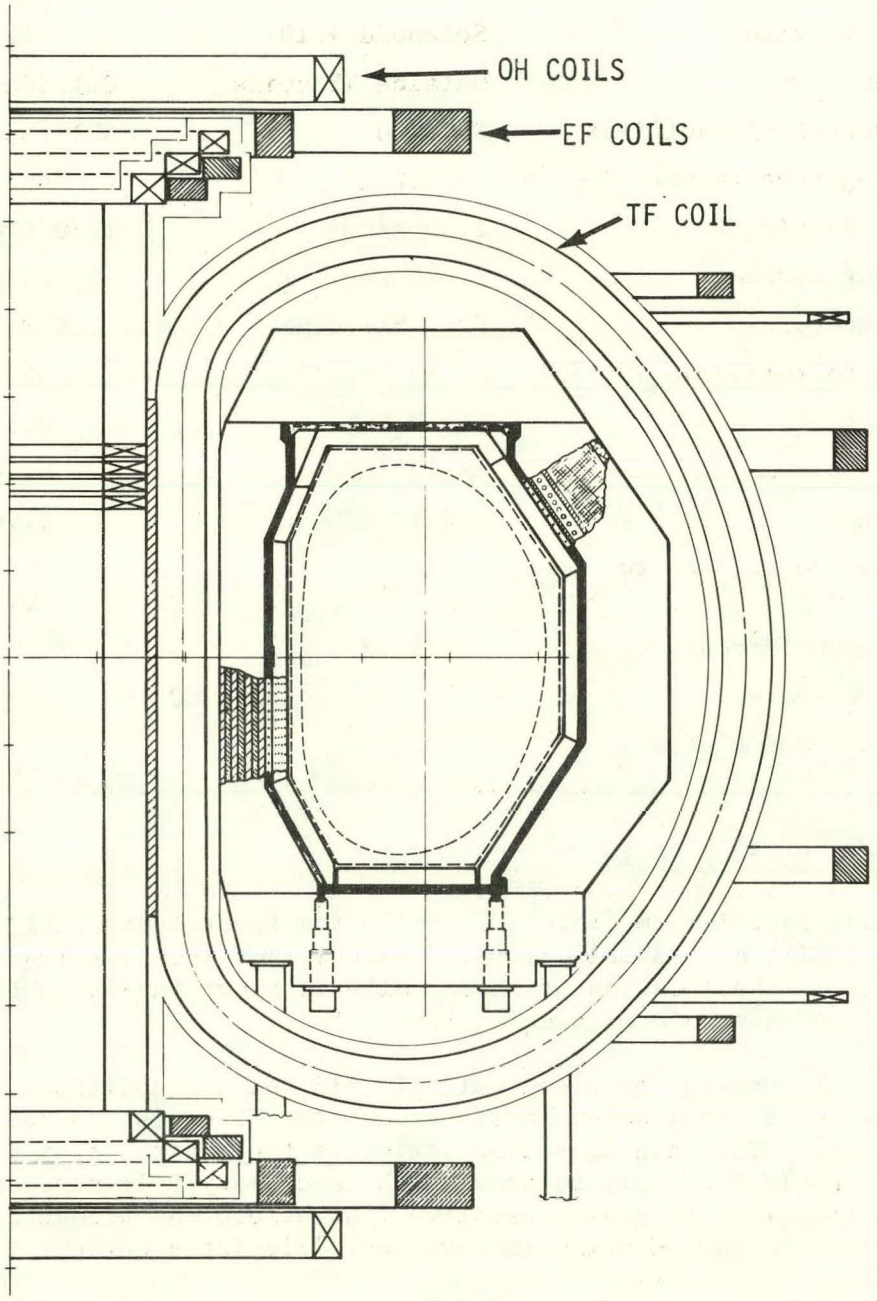

Figure II-3. EPR magnet schematic, showing TF, OH, and EF coils.

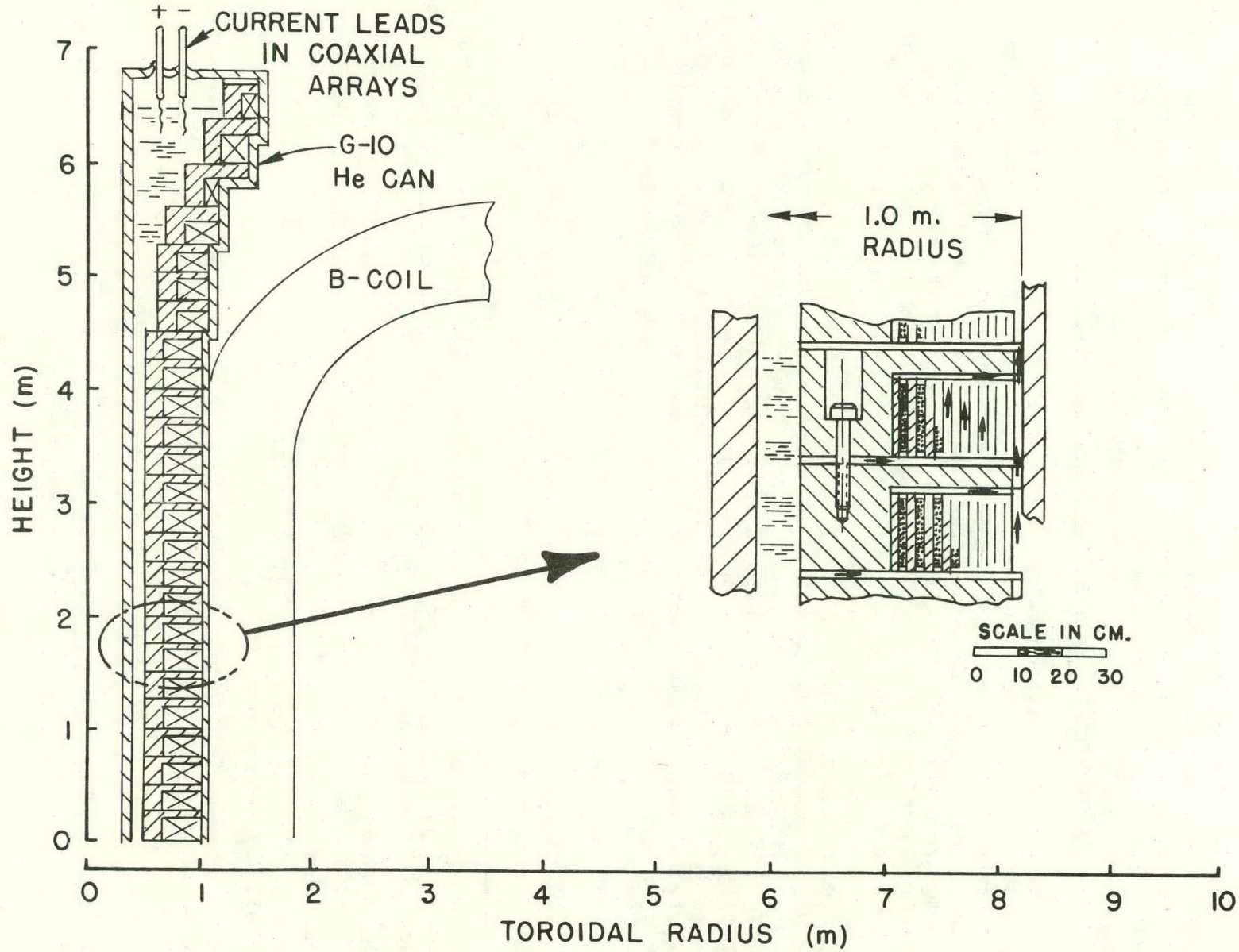

Figure II-4. Segmented OH solenoid and support.

2. Equilibrium Field Coils

Twelve coils comprise the EF coil system. An elongated, D-shaped plasma requires more current and energy in the EF coil than a circular plasma would, but the required field pattern can be achieved by EF coils outside the TF coils. The EF coil system is described in more detail in reference 2.

3. Reducing Field Ripple from Toroidal Field Coils

Using ferromagnetic segments of the shield to reduce field ripple is being studied. Improved access could be achieved if the sixteen TF coils were replaced by twelve with the same total ampere-turns. However, the field ripple in the outer part of the plasma (out to 6.0 m) is much worse with twelve coils than with sixteen. If segments of the blanket/shield directly inward from the outer leg of each TF coil were ferromagnetic, the ripple would be reduced.

The effect of adding the iron, both for a 16-coil system and a 12-coil system, was computed at the Rutherford Laboratory, using the magnet design program GFUN3D.[3,4] For the 16-coil system, the iron was assumed to be in the form of a block 0.5 m x 0.5 m x 5.0 m high inside the outer leg of each TF coil; with 12 coils each block was increased by 16/12 in cross sectional area. At 6.0 m, for example, the iron reduces the ripple from 1.3% down to 0.2% for sixteen coils, but only from 4.6% down to 2.9% for twelve coils and the specified amount of iron. Twice the iron reduces the ripple with 12 coils to 0.5% at 6.0 m. In an actual reactor, the ferromagnetic material could be incorporated as part of the blanket and shield system.

The magnet systems design was presented in more detailed at the Knoxville IEEE Symposium on Fusion Technology.[5]

---

[2] J. N. Brooks, et al., "The Equilibrium-Field Coil System for the ANL EPR Design," Proc. of 7th Symposium on Engineering Problems of Fusion Research, Knoxville, Tennessee (1977).

[3] M. J. Newman, C. W. Trowbridge, and L. R. Turner, "GFUN: An Interactive Program as an Aid to Magnet Design," Proc. 4th International Conference on Magnet Technology, Brookhaven 617-626 (1972).

[4] A. G. Armstrong, et al., GFUN3D User Guide, Rutherford Laboratory, RL-76-029/A (November, 1976).

[5] L. R. Turner, S-T. Wang, S. H. Kim, Y. C. Huang, and R. P. Smith, "Superconducting Magnet System for the ANL EPR Design," Proc. of 7th Symposium on Engineering Problems of Fusion Research, Knoxville (1977).

C. TNS and EPR Tritium Systems Studies

R. G. Clemmer and V. A. Maroni, EPR Project

Systematic analyses of tritium processing and torus evacuation requirements were carried out for two near-term tokamak-type fusion reactors, namely

the Experimental Power Reactor (ANL-FY 1977 EPR)[6] and the next step (GA/ANL TNS).[7] As a major part of this effort, a tritium systems code (TCODE) was developed with a broad range capability for performing both detailed reference-point analyses and many different types of parametric sensitivity studies. TCODE is a versatile tool for parametric analyses in that it handles 50 input parameters (including plasma characteristics, reactor dimensions and operating conditions), and produces 60 output parameters (including torus evacuation requirements, tritium facility requirements, fuel flow rates, inventories, and costs). A partial listing of the projected parameters as calculated by TCODE for the two near-term reactors, TNS[7] and EPR,[6] is shown in Table II-3. Many of the input parameters in Table II-3 were systematically varied and the effects of these variations on numerous output parameters were determined. From these variation studies, three plasma related parameters were found to have substantial effects upon the tritium and vacuum systems. These parameters are the particle confinement time, the reflectance coefficient, and the dwell period.

1. Particle Confinement Time

The sensitivity of fractional burnup and of tritium mass flow to the particle confinement time, τ_p, for the two near term reactors, TNS and EPR, is shown in Figure II-5. At τ_p values of less than 5 s there is a sharp decrease in achievable fractional burnup and a corresponding rise in tritium exhaust rate. Since the projected values of τ_p are $\sim$ 2 s for TNS and $\sim$ 5 s for EPR (Table II-3), potential deviations of τ_p from the anticipated values can have profound effects on the design of vacuum and tritium systems. This point is further illustrated in Figure II-6 which shows the effects of τ_D upon overall evacuation speed at the torus and pump capacity. Since a decrease in τ_p increases mass flow rates, required pumping speed must also increase. An increase in required effective evacuation speed (at the torus) has further implications. Since it is desirable from the standpoint of neutronic design to minimize both the number and size of penetrations, the torus evacuation systems are designed such that the duct conductance is minimized and the pump speed is chosen to be sufficiently high to achieve the required evacuation speed at the torus. As a result, an increase in required overall evacuation speed can cause a substantial increase in the required pump speed. Since τ_p significantly affects tritium throughput rates, required pump capacities are correspondingly affected, as shown in Figure II-6.

---

[6] W. M. Stacey, et al., "EPR-77: A Revised Design for the Tokamak Experimental Power Reactor, Argonne National Laboratory Report ANL/FPP/TM-77 (March, 1977).

[7] TNS SCOPING STUDIES, Interim Status Report: October 1976 - March 1977, General Atomic Company Report GA-A14412 and Argonne National Laboratory Report ANL/FPP/77-2 (May 1977).

Table II-3. Tritium Facility and Vacuum System Parameters for Two Near-Term Tokamak Reactor Designs

Parameter	GA/ANL TNS	ANL/FY 1977 EPR
Plasma and Burn Cycle		
* Burn Time (s)	30.	64.
* Dwell Time (s)	270.	16.
* Lag Time (s)	2.	2.
* Power Per Burn Pulse (MW)	340.	325.
* Ion Density (Particles/m^3)	1.47×10^{20}	1.30×10^{20}
* Plasma Volume (m^3)	255.	360.
* Particle Confinement Time (s)	1.63	5.00
* Reflection Coefficient	0.97	0.95
* Energy/Fusion (pJ)	2.82	2.82
* Fractional Burnup	0.124	0.161
Torus Evacuation		
* Volume of Torus (m^3)	314.	450.
* Surface Area (m^2)	349.	430.
* Duct Diameter (m)	0.50	0.80
* Duct Length (m)	8.00	6.00
* Number of Pumps, Operating/Total	3/6	12/24
Speed/Pump (m^3/s)	25.0	80.0
* Capacity/Pump (Pa-m^3)	3333.	10666.
Post Burn Gas Pressure (Pa)	0.551	1.09
Preburn Pressure (Pa)	4.00×10^{-3}	4.00×10^{-3}
Post Burn Gas Load (Pa-m^3)	173.	490.
Required Pump Capacity (Pa-m^3)	2766.	7350.
Required Pump Speed (m^3/s)	3.84	37.05
Tritium and Fuel Processing		
Tritium Input/day gas loading (g)	27.17	126.4
Tritium Fueling/day (g)	20.97	120.6
Tritium Exhaust/day (g)	42.18	207.2
Helium Exhaust/day (g)	7.95	53.0
Protium Exhaust/day (g)	0.32	1.65
Carbon Exhaust/day (g)	1.93	9.88
Oxygen Exhaust/day (g)	0.15	0.79
Nitrogen Exhaust/day (g)	0.14	0.69
Argon Exhaust/day (g)	1.28	6.59
* Neutral Beam Power (MW)	60.0	60.0
* Beam Energy (keV)	150.0	150.0
* Neutral Beam Duration (s)	5.00	5.70
Total Gas Load/Beam Injector (Pa-m^3)	33.6	8.20
* Number of Injectors	6	12
Deuterium Injected/day (g)	11.95	51.10
Deuterium in Beam Pumps/day (g)	47.67	99.47
Tritium in Beam Pumps/day (g)	0.57	2.60
Tritium Inventory: Fuel Processing (g)	14.3	20.8
Tritium Inventory: Storage (g) (30 days burn)	178.9	1192.5
Tritium Inventory: Fuel Delivery (g)	60.5	110.3
Total Tritium Inventory (g)	258.3	1343.7
* Volume of Reactor Building (m^3)	1.00×10^5	1.00×10^5
Maximum Conceivable Tritium Release (g)	65.2	130.4
* Cleanup Time (Hours)	48.0	48.0
Flow Rate to EDS (m^3/s)	6.9	7.4

* Input Parameters

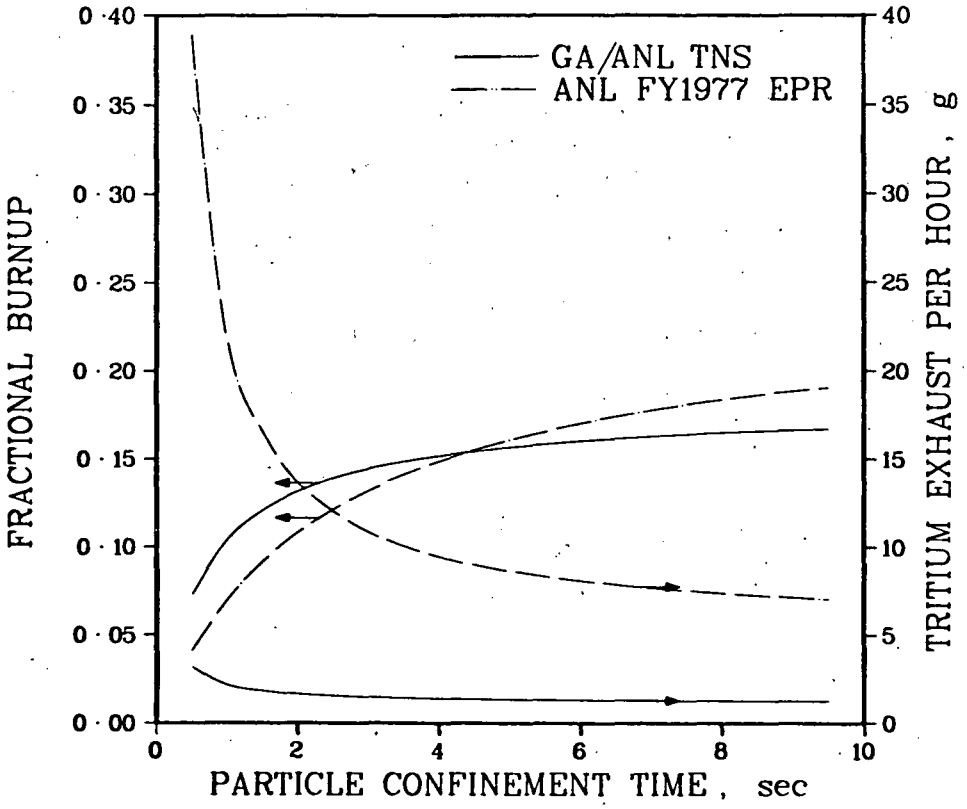

Figure II-5. The effect of τ_p upon fractional burnup and mass flow rates.

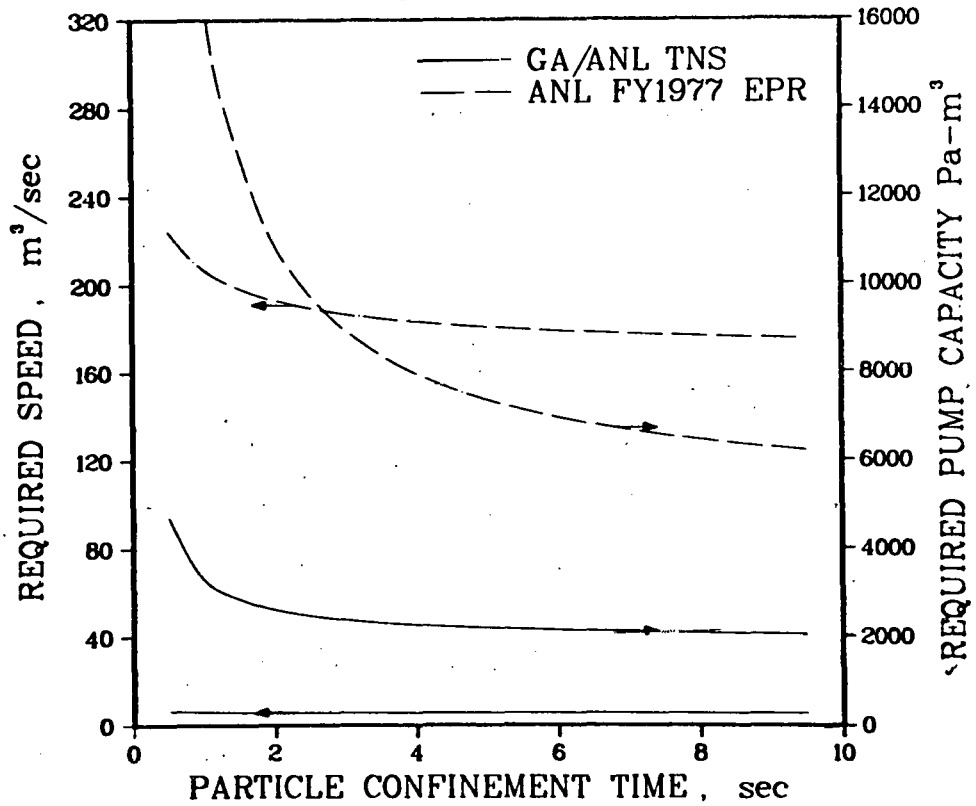

Figure II-6. Required overall torus evacuation speed and tritium inventories as functions of τ_p.

2. Reflectance Coefficient

The reflectance coefficient, R, is defined as the probability that an escaping particle will eventually recycle back into the plasma. In a near-term tokamak reactor, such as TNS or EPR, with passive impurity control, R is expected to be very close to unity, i.e., greater than 0.90. On the other hand, a reactor having a divertor of 90% efficiency would have R $\simeq$ 0.10. The fractional burnup is a reciprocal function of (1-R) and, therefore, the tritium exhaust rate is a linear function of (1-R) as shown in Figure II-7. Since tritium inventories depend on throughput rates, the inventories are also linear functions of (1-R). Required pumping speed is moderately sensitive to R, provided the reactor does not have a divertor.

3. Dwell Time

In the case of EPR or an upgraded TNS it is necessary to operate the reactor at as high a duty factor as is possible. Because the maximum burn time for a reactor having passive impurity control is rather limited, there is incentive to minimize the dwell period. As shown in Figure II-8, when the dwell time is decreased to below 20 s, the required overall evacuation speed, (at the torus) rises dramatically. As previously discussed, since

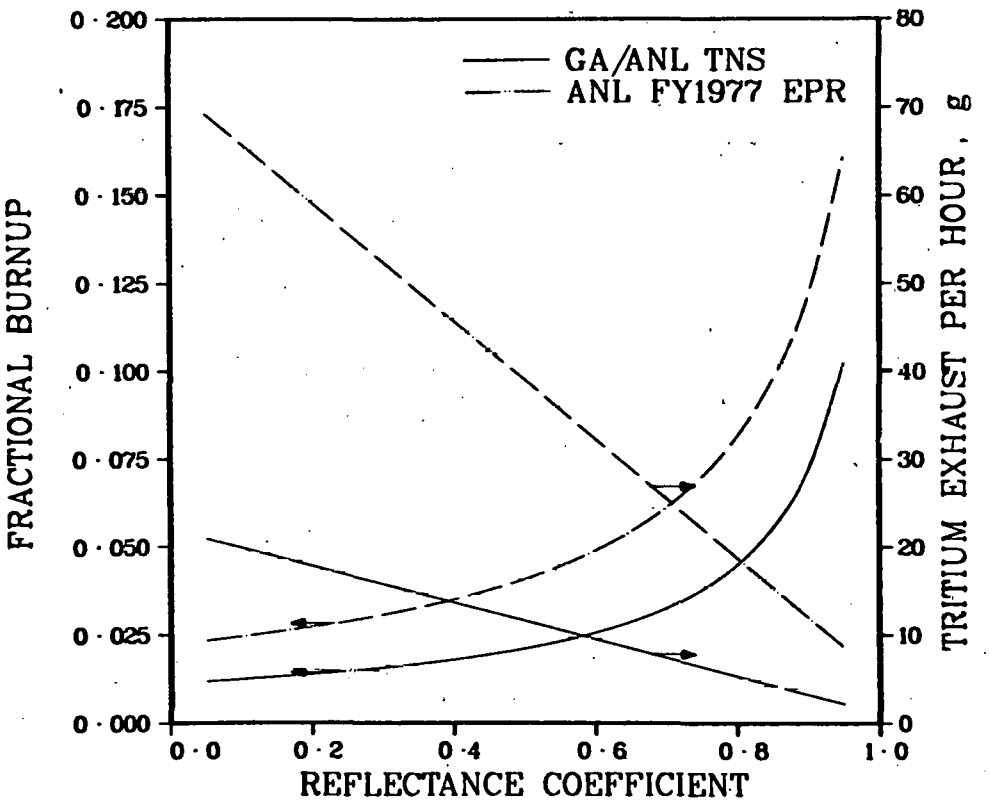

Figure II-7. The effect of the reflectance coefficient upon fractional burnup and mass flow rates.

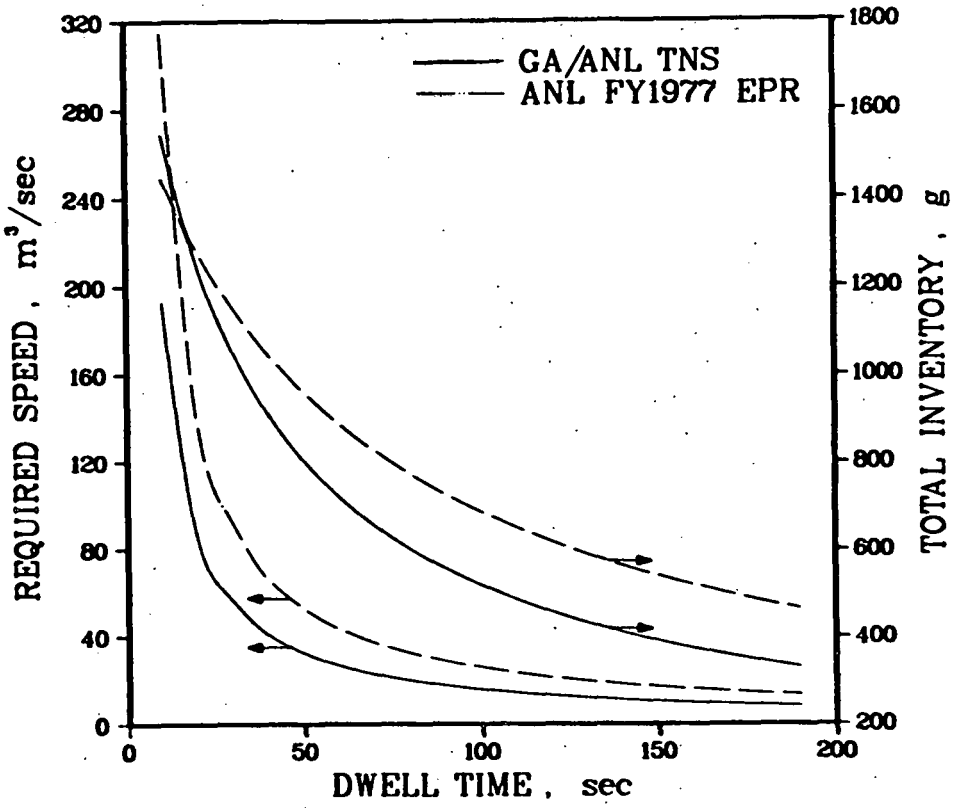

Figure II-8. The impact of dwell time upon torus evacuation requirements and tritium inventories.

an increase in required overall speed affects both pump design and the number and size of the vacuum penetrations, the dwell time is a parameter of considerable significance to vacuum system design. Because of the effect of changing duty factor, all tritium handling systems and system inventories are sensitive to the dwell time. This sensitivity is illustrated in Figure II-8.

4. Cost Considerations

The estimated capital costs of the tritium handling systems, including the tritium facility building, are shown in Table II-4. While the increase in size for EPR results in some significant cost increases for selected items, particularly in the case of the vacuum system, overall costs are dominated by large relatively fixed cost items such as the air detritiation system. The result is that on the whole the total costs are rather insensitive to reactor size and design.

Table II-4. Estimated Costs ($ Millions, 1977)

	GA/ANL TNS		ANL/FY 1977 EPR	
Torus Evacuation		0.8		3.5
Emergency Air Detritiation (EDS)		8.3		8.9
Tritium Processing				
Piping	0.7		0.8	
Distillation Cascade	0.7		0.9	
Gloveboxes & Purifiers	2.7		2.7	
Miscellaneous	0.7		1.1	
Tritium Processing Subtotal		4.8		5.5
Total		13.9		17.9

Two recently presented papers describe these TNS and EPR tritium facility studies in greater detail.[8,9]

[8] R. G. Clemmer, "Impact of Plasma Performance Parameters upon the Vacuum and Tritium System Design Requirements for Near-term Tokamak Reactors," presented at the International Atomic Energy Agency Conference and Workshop on Fusion Reactor Design, Madison, Wisconsin (October 10-21, 1977).

[9] J. M. Mintz, R. G. Clemmer and V. A. Maroni, "Tritium Handling Trade Studies and Design Options for the GA/ANL TNS," presented at the Seventh Symposium on Engineering Problems of Fusion Research, Knoxville, Tennessee (October 25-28, 1977).

III. TNS PROJECT

A. Development of Cryostable Superconducting Pulsed Coils

S. H. Kim and S-T. Wang, Accelerator Research Facilities

A set of superconducting ohmic-heating (OH) coils has been selected as the design for the ANL/GA TNS E-coil system[1] and in all likelihood for future tokamak reactor systems. The primary advantage of a superconducting OH coil over a water-cooled copper OH coil is the minimization of equipment and operational costs. ANL has proposed a five-year development program for superconducting OH coil and power supply to DOE/DMFE[2] and has started an aggressive development program in FY 1977.

The main objectives for FY 1977 were, to develop cryostable basic cable configurations with reasonably low losses, to develop 12 kA cryostable cable, using it to design and build a 1.5 MJ pulsed coil, and to develop a rather inexpensive large fiberglass reinforced helium cryostat for the 1.5 MJ pulsed coil. The principal objective in building the 1.5 MJ ac coil is to demonstrate ac cryostability of a large coil ranging from 2 T/S up to 12 T/s.

The objectives of FY 1978 are to study the parallel operation of pulsed coils, to develop a 50 kA cryostable cable, to build a small test coil with the 50 kA cable, and to perform a preliminary engineering design of a 100 MJ model coil. All of these efforts are important steps to the advancement in the state-of-the-art of pulsed superconducting magnet technology. The ultimate goal of the ANL pulsed coil program is to design, build and test a demonstration-size, 100 MJ pulsed superconducting coil. The coil would be tested with a 100 MVA motor-generator-flywheel set and energy conversion system available at ANL.

1. Basic Cable Studies

a. Principle of AC Cryostability

The requirements of low loss and cryostability are conflicting requirements. Compromise between the two must be made when selecting a cable design. The basic principle chosen is to achieve cryostability within the basic cables. The final cable may consist of many basic cables stranded with full transposition. To limit large eddy current loss, only limited current sharing among basic cables is allowed.

---

[1] "TNS Scoping Studies, Interim Status Report," Argonne National Laboratory, ANL/FPP/77-2, or General Atomic Company, GA-A14412 (May, 1977).

[2] R. L. Kustom and S-T. Wang, "The ANL Research and Development Program for Large Pulsed Superconducting Coils and Energy Storage and Transfer for Tokamak Fusion Reactors," Argonne National Laboratory (June, 1977).

b. Three Selected Basic Cable Configurations

Figure III-1 illustrates the three basic cables chosen. These are the simplest cable configurations formed by groups of three or groups of seven. The basic cables have a short sample value of 405 A at 5 T and a ratio of Cu/NbTi of 20:1. Each superconducting strand, 20 mils in diameter containing 2041 6-μ filaments with two twists per inch, will carry 135 A at 5 T. A sufficient number of pure OFHC copper wires are twisted around the superconducting composite strands to share the current in case of a normal transition. It was originally hoped that mechanical contact through stranding processes may provide enough electrical contact for current sharing and simultaneously fulfill the requirement of low loss. Each strand, superconducting composite or pure OFHC wire, is tinned with staybrite to provide cushion-like contact.

c. The Cryostability Test

The cryostability test was made using 1.2 m long noninductively wound samples. Figure III-2 shows the current-sharing characteristics of a basic cable. The current sharing of all three cables indicate that the minimum propagating current, I_{mp}, is slightly greater than the critical current, I_c, but the recovery current, I_r, is less than I_c. There is little difference in the current-sharing characteristics among the three basic cables.

2. 5 kJ Test Coils Studies

a. Coil Characteristics

To study the ac losses and the magnet current sharing, three small test coils were fabricated using each of the three cables of Figure III-1. The magnet characteristics are listed in Table III-1. The coils were wound on micarta coil forms as shown in Figure III-3. The cable is insulated with 3.5 mil thick sticky mylar tape with 90% coverage. Cooling channels between each layer are 1/16 inch thick and 1/8 inch wide. These coils were cycled many times between zero and 590 A (critical current at 3.1 T) with a ramping rate of as much as 7 T/s without going normal. However, when the coils were charged beyond 600 A, sections of the conductor in the coils went normal recovering completely at a current lower than the critical current.

b. Mechanical Perturbation Studies

To study the conductor motion and its frictional heating, a potentiometer is used to balance the inductive voltage of the test coil. A typical perturbation recording is shown in Figure III-4. It is interesting to see that perturbation amplitude increases as current increases toward I_c. In addition, we also observed that these mechanical perturbations occur only once (in the original run). During later runs the magnetic pressures are not large enough to induce mechanical perturbations since the coil has settled.

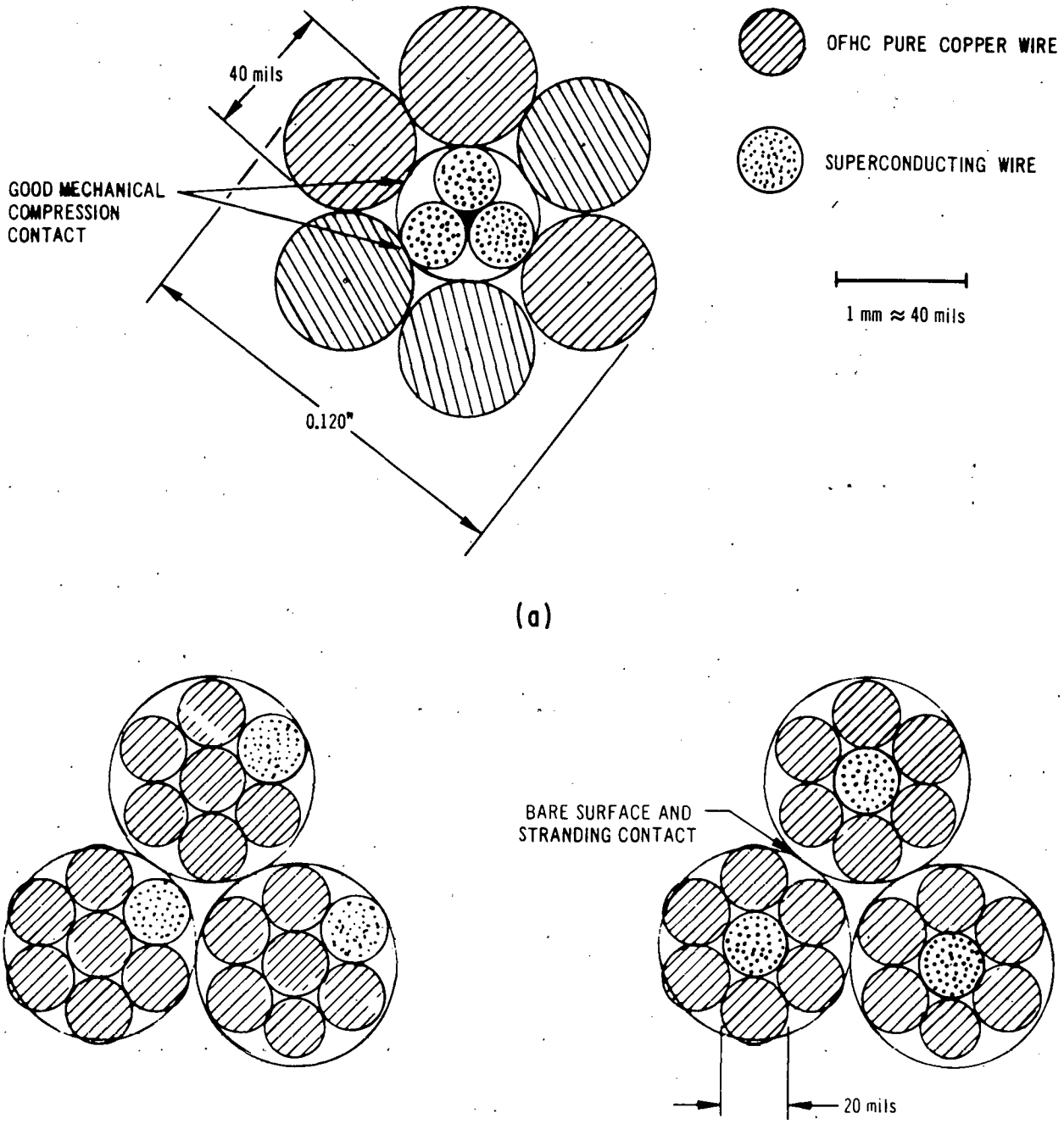

Figure III-1. Three cryostatic stable basic cables. Superconducting wire (SC): 20 mils diameter, 2041 filaments, Cu/SC = 1.8 and twisting pitch 1.27 cm (= 2 TPI). (a) three SC wires are twisted at 4 TPI and six Cu wires are twisted around the SC at 1.5 TPI, (b) and (c) six Cu wires and one SC wire are twisted at 2 TPI and those three subgroups are twisted at 1.5 TPI.

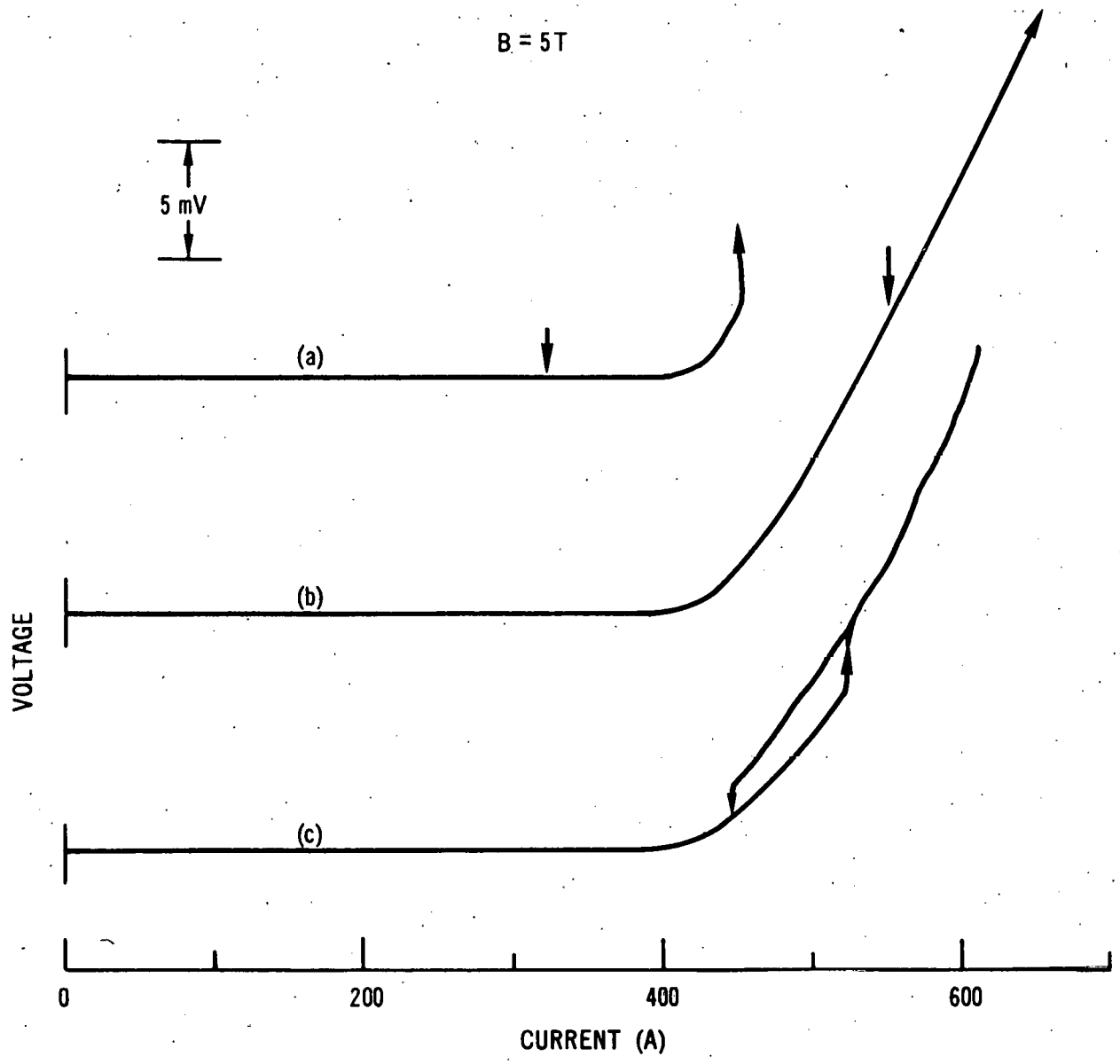

Figure III-2. Current-sharing characteristics of cable (c) of Figure III-1. (a) bare wires and stranding contact, (b) completely soldered and (c) subgroups are soldered and insulated.

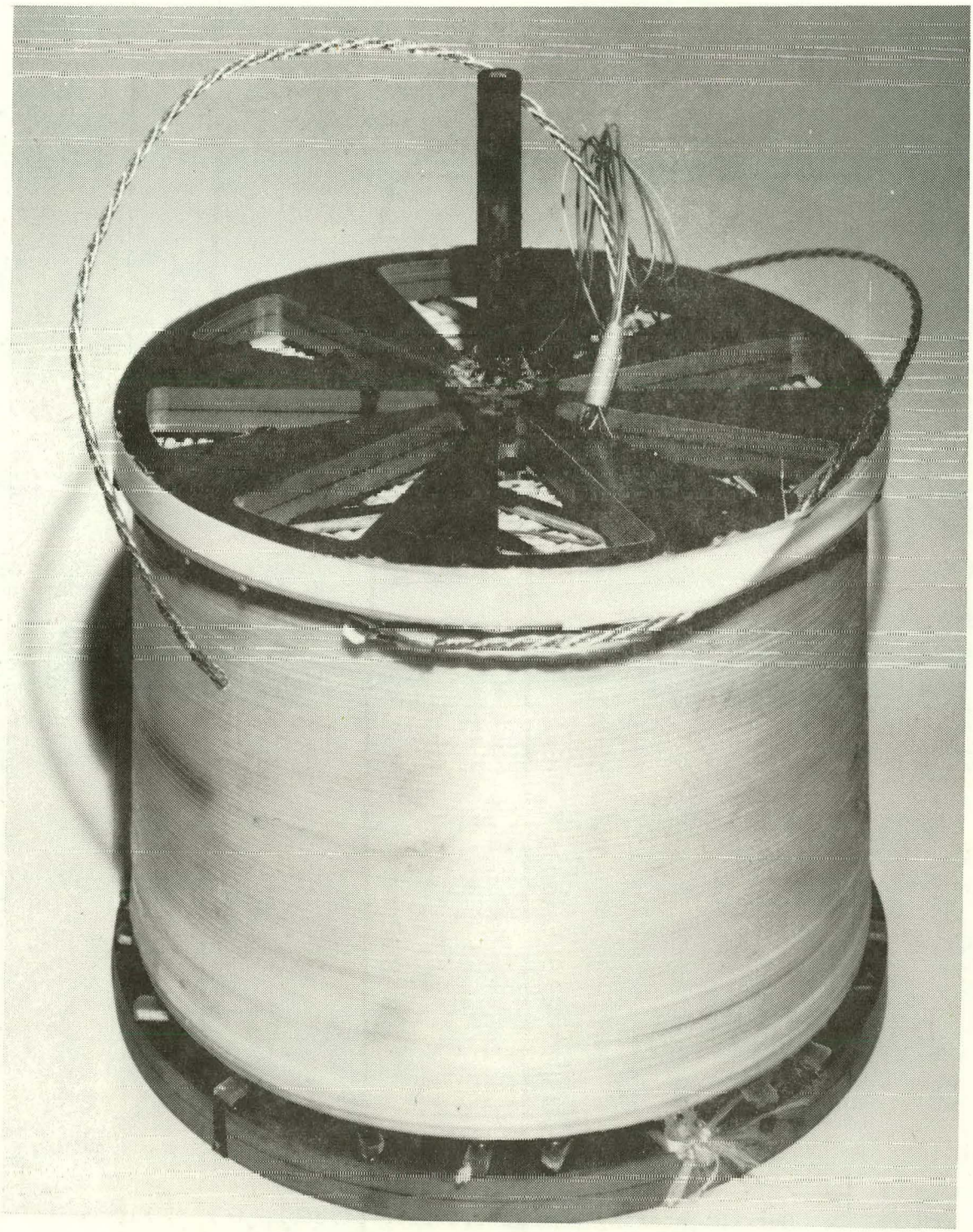

Figure III-3. 5 kJ test coil.

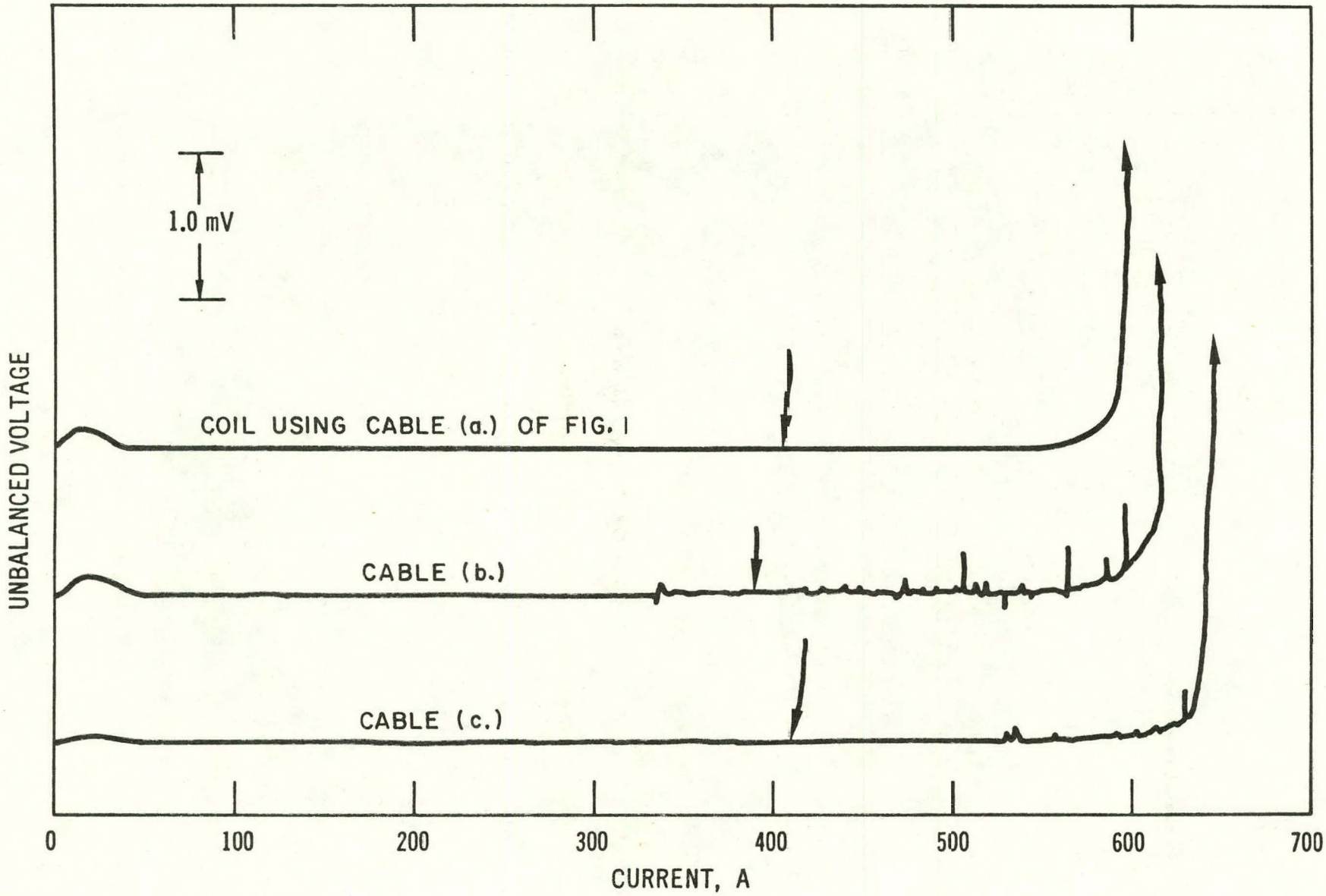

Figure III-4. Mechanical perturbation recording of test coils, (a) after several cycles, (b) and (c) first cycle.

Table III-1. Magnet Characteristics of Test Coils

Axial Length	5.4 inches
Coil Inside Diameter	1.25 inches
Coil Outside Diameter	8.5 inches
Central Field	3.1 T
Operation Current	590 A
Inductance	27.5 mH
Number of Turns	770
Number of Turns/Layer	40.5
Number of Layers	19
Stored Energy	4.8 kJ
Total Cable Length	300 m
Average Current Density	3850 A/cm^2
AC Losses at 7.1 T/s	56 W

c. AC Loss Measurements

AC losses have been measured by means of both calorimetric and electronic integrator methods. Hysteresis loss in the superconducting filaments is only about 1.5 J/cycle at B = 3.0 T. The dominant part of the ac loss is due to the eddy currents in the copper stabilizer. The eddy current loss can be expressed as

$$P_e = V\,(\ell p/2\pi)^2\,\dot{B}^2/\rho, \qquad (1)$$

where V is the volume of the cable, ℓp is the twist pitch and ρ is the effective transverse resistivity.

The experimental data in Figure III-5 shows that the eddy current loss is proportional to $\dot{B}^2$ and is in agreement with Eq. (1). Here the undetermined parameter ρ turns out to be approximately 10 times the value of OFHC copper at 4.2 K. Surprisingly, the coil using the cable in Figure III-1 (b) was found to have losses four times higher than the other two coils.

3. High-Current Cable Development

a. Selected Basic Cable Design

Current-sharing characteristics of the cable shown in Figure III-1 (c), under various conditions are illustrated in Figure III-2. Since stranding contact does not provide enough of a margin for current sharing (curve a),

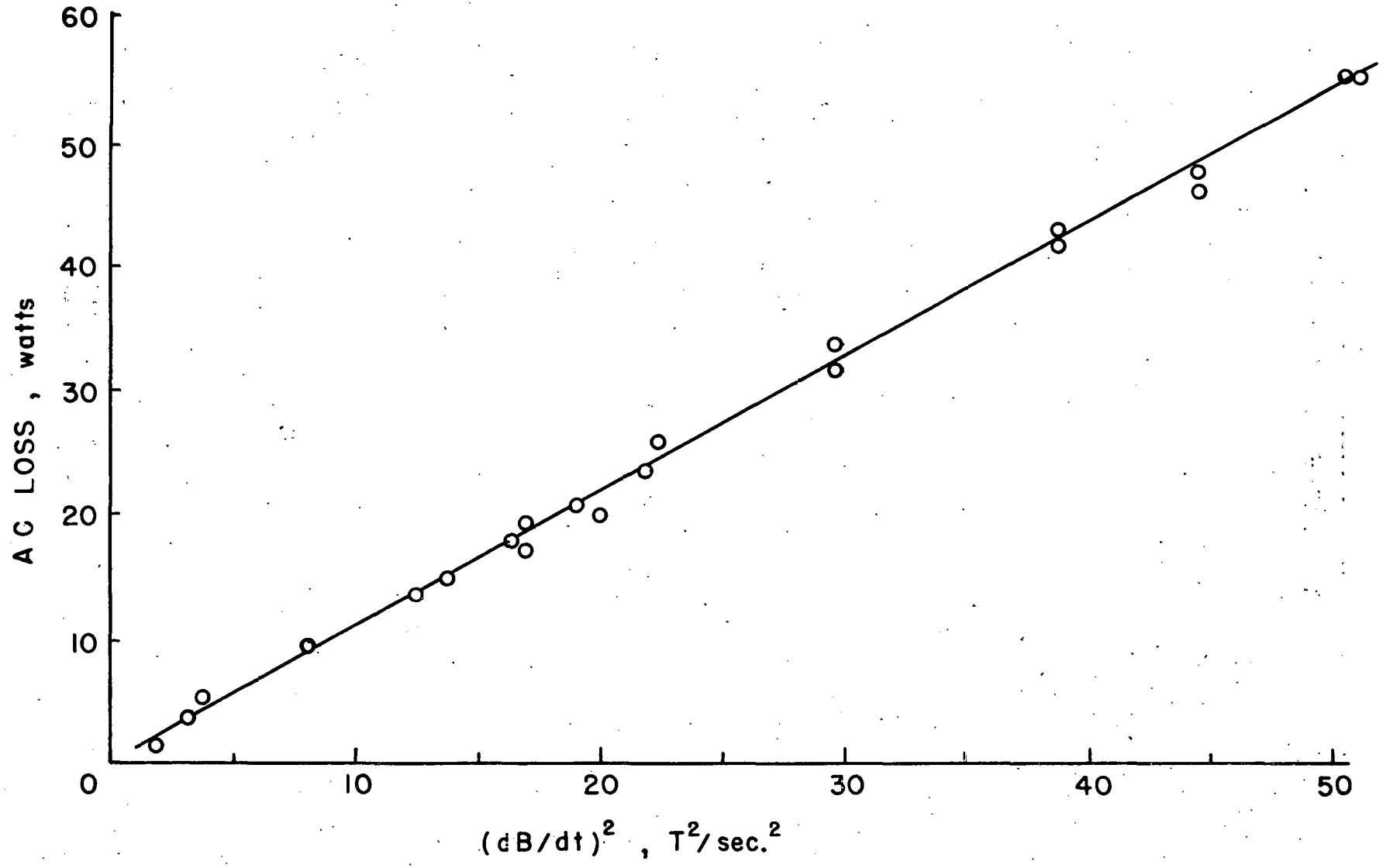

Figure III-5. AC losses of the test coils.

the current-sharing terminal characteristics for the case where the entire cable is soldered together were investigated. The results indicate that both I_r and I_{mp} are much greater than I_c as shown in curve b of Figure III-2. However, it is quite obvious that the ac losses of the soldered cable would be rather large.

The cable configuration giving the best compromise between cryostability and ac loss is shown in Figure III-6 (a). The six pure copper wires are soldered to the superconducting composite forming an essential current-sharing subgroup. A thin coating of glyptal varnish is brushed on the surface of each of the three subgroups in the basic cable. The high dielectric strength coating serves to reduce the eddy current losses among the subgroups. The coating is thin enough ($\sim$ 0.0125 mm), however, so that limited current sharing among subgroups will be allowed. Also, the heat transfer of the boiling helium is not affected because the coating is thin. In fact, the minimum film boiling heat-transfer rate will be enhanced as a result of the thin coating. The current sharing of the selected basic cable was tested and shown in curve c of Figure III-2.

b. 12 kA Cable Development

To form the 12 kA cable, twenty-four basic cables are twisted around 1/32 inch thick by 1-1/4 inch wide stainless steel strip at a twisting pitch of 4.5 inches as shown in Figure III-6 (b). The stainless steel strip, which is well insulated from the basic cables, serves as the backbone in the cabling processes and as the structural member against hoop stress of the 1.5 MJ coil. Supercon Inc., has been commissioned to produce a 600 m long cable. The first 69 m of the cable will be fabricated for the purpose of testing the design. The remaining 531 m will be used to wind a prototype superconducting OH coil with a central field of 4.3 T and a stored energy of 1.5 MJ.

4. 1.5 MJ Pulsed Coil

a. Design

The design of the pulsed coil and fabrication of G-10 bobbin are completed. The magnet characteristics are tabulated in Table III-2. The coil should be cryostable and its ac losses will be rather large although tolerable. The large ac losses are mainly due to the long twist pitch of the superconducting composite.

b. Test

The coil will be cooled down in a large plastic dewar as shown in Figure III-7. It will be tested with a 7 MW power supply. Prior to the coil test, a pair of 15 kA current leads for the 1.5 MJ coil will be tested. AC losses will be measured by an electronic integrator method. For this purpose, a liquid nitrogen cooled linear inductor has been fabricated. Conductor motions and energy release due to the frictional heating in the coil will be measured by unbalanced voltage methods and a pressure transducer.

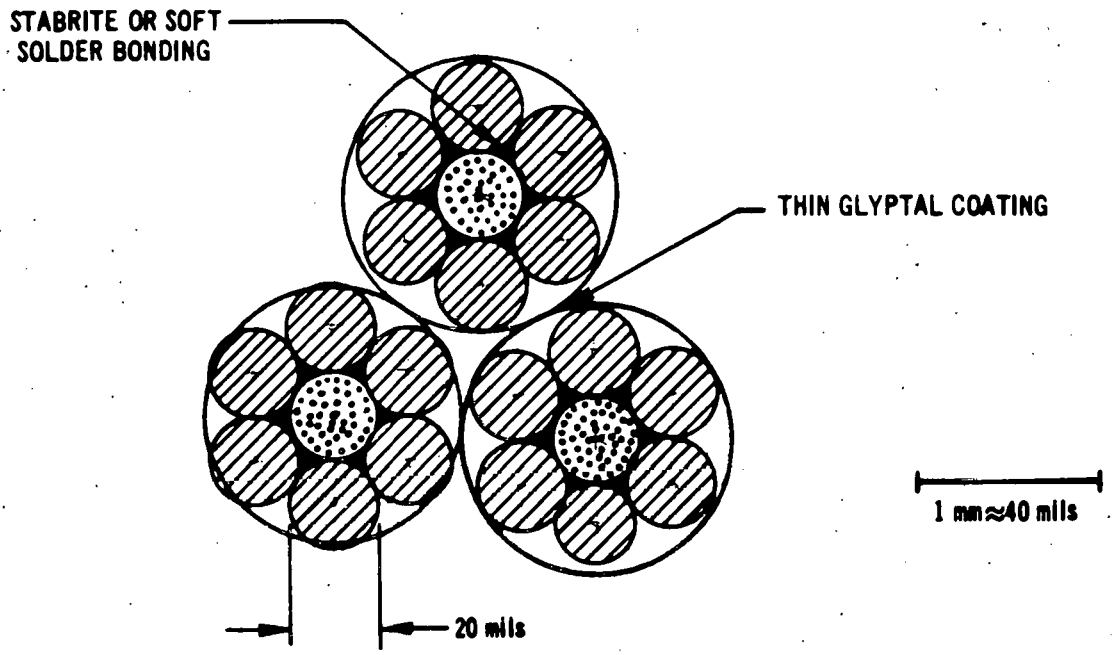

(a)

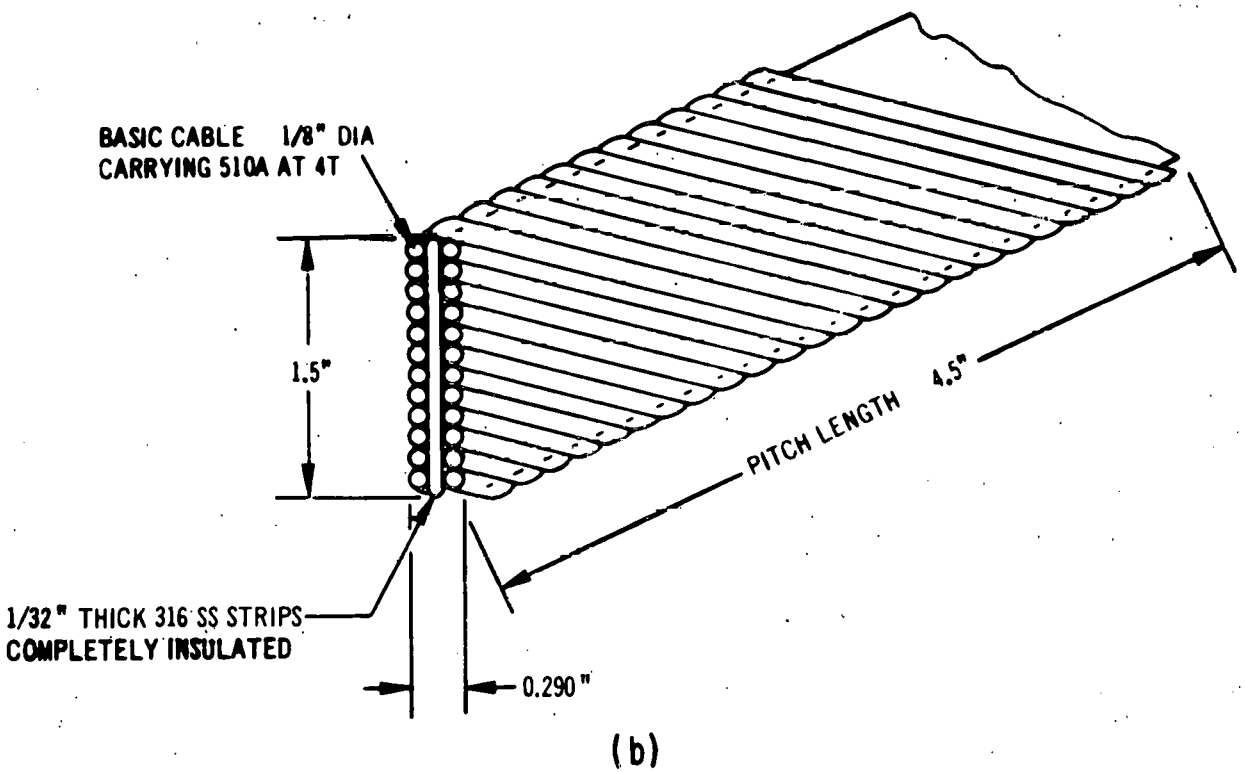

(b)

Figure III-6. (a) Selected basic cable, and (b) 12 kA cryostable cable.

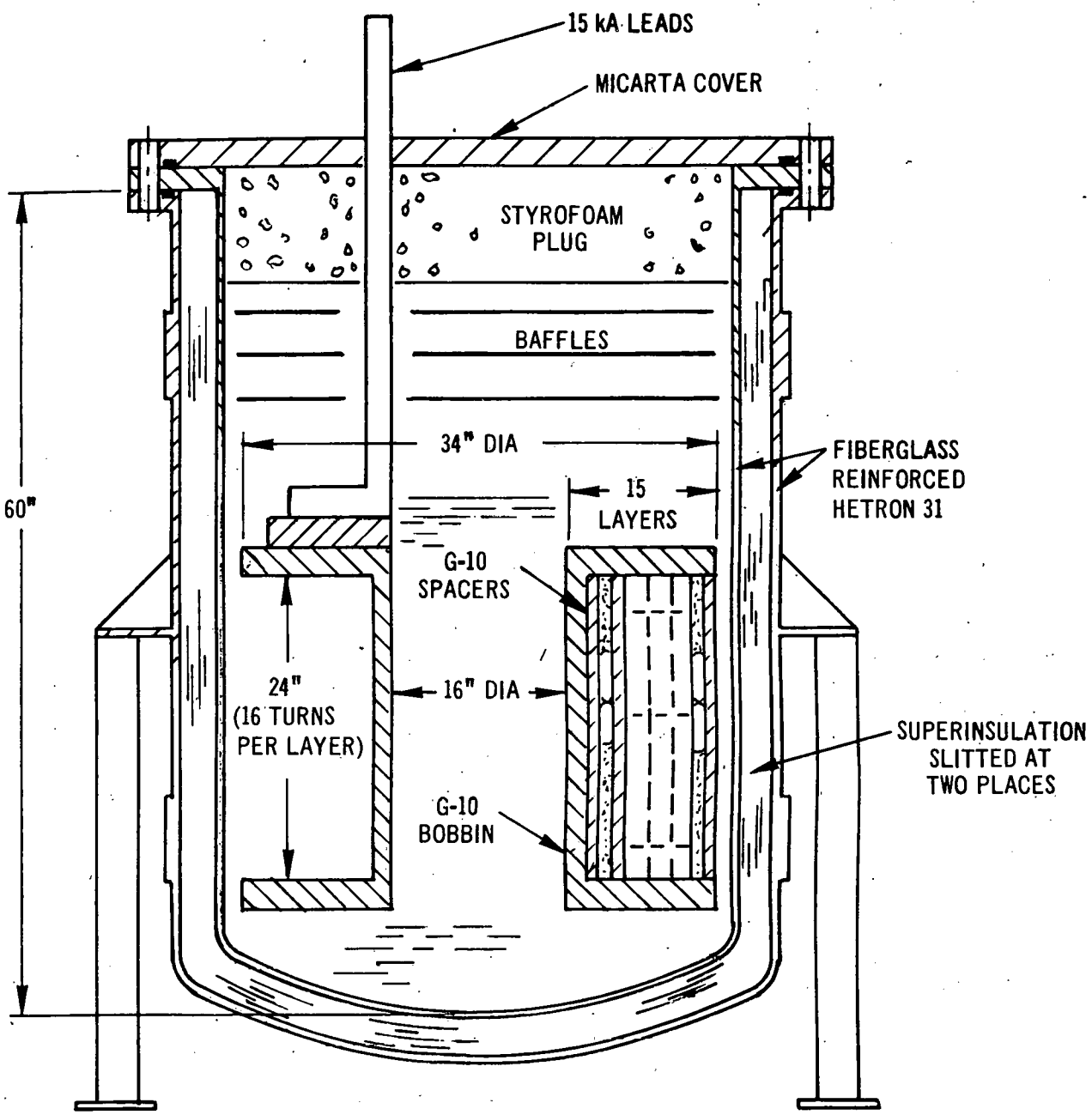

Figure III-7. Fiberglass-reinforced plastic dewar and 1.5 MJ coil.

Table III-2. Magnet Characteristics of 1.5 MJ Prototype Superconducting OH Coil

Central Field	4.3 T
Peak Field	4.7 T
Operational Current	11 kA
Inductance	24.9 mH
Stored Energy	1.5 MJ
Coil Inside Diameter	41.6 cm
Coil Outside Diameter	86.4 cm
Axial Length	58.1 cm
Number of Layers	18
Number of Turns/Layer	15
Total Number of Turns	270
Layer-to-Layer Spacing	4.76 mm
Conductor Current Density	5760 A/cm^2
Cryostat Recovery Heat Flux	0.35 W/cm^2
Average Current Density	2274 A/cm^2
AC Losses	3.7 kW at 8 T/s
Maximum Radial Magnetic Pressure	12 ksi
Maximum Axial Magnetic Pressure	4 ksi

5. Development of Large Fiberglass-Reinforced Plastic Dewars

For superconducting OH coils, a stainless steel helium cryostat would have excessive ac losses. Therefore, a non-metallic cryostat with low helium permeation must be developed. As a first step, a plastic cryostat was developed for the 1.5 MJ pulsed coil. The plastic cryostat, as shown in Figure III-8, consists of two tanks with 100 layers of superinsulation between. The metallic superinsulation is slit to reduce the eddy current heating. The inner tank has an inside diameter of 91.4 cm, a depth of 152.4 cm and a wall thickness of 0.95 cm; while the outer tank has an inside diameter of 107 cm, a depth of 156.5 cm and a wall thickness of 1.27 cm. Both tanks are made of fiberglass reinforced Hetron 31 polyester with 35% glass component.

The cryostat was filled with liquid nitrogen without the superinsulation. Afterwards, many patch-like small cracks were found on the inner surface of the inner tank. Therefore, the inner tank was reinforced by about 1-cm thick wet-wound fiberglass epoxy. The cryostat cover is a 6.3-cm thick micarta plate. A 30-cm thick styrofoam radiation shield was cut to fit the diameter of the inner tank and is attached to the micarta cover. With 100 layers of superinsulation, the cryostat was filled with 80 cm of liquid helium. The steady state heat leak measured was about 0.85 W. A 10^{-7} Torr vacuum was achieved with cryopumping. Helium permeation was not detectable over a period of 48 hours.

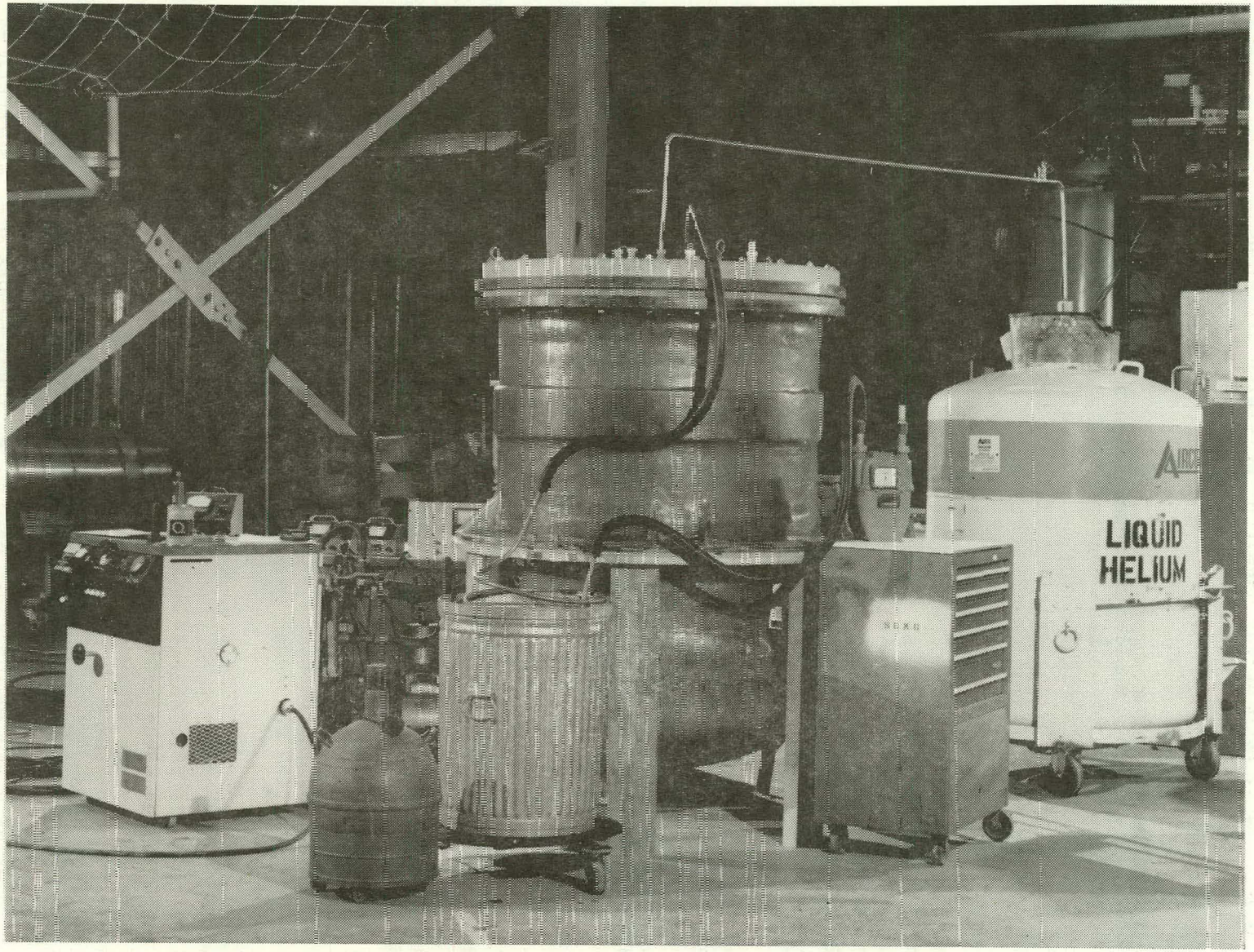

Figure III-8. Plastic helium cryostat.

B. Limits on B for a Graded OH Solenoid

L. R. Turner, Accelerator Research Facilities Division

Because the outer diameter of the superconducting OH solenoid of a tokamak influences many other dimensions of the device, that diameter should be as small as possible to minimize overall cost. However, providing a given flux change, $\Delta\phi$, with a smaller diameter solenoid requires that the field be higher, and the diameter is thus constrained by the highest field B that can be attained in the solenoid and the maximum rate of change $\dot{B}$ of that field. The field is limited by the critical field of the conductor, and $\dot{B}$ is limited by eddy current and filament heating losses.

However, it turns out that for an ungraded cryostable superconducting solenoid the lowest outer diameter, D_o, is not achieved at the highest field. The mean diameter decreases as $B^{-1/2}$, but higher fields require more superconductor, more copper, more stainless steel for support and larger helium channels for added cooling. There is an optimum B which minimizes D_o, the sum of the mean diameter and the thicknesses of NbTi, copper, stainless steel and helium. Reference 3 describes the calculations in more detail.

However, if the solenoid is graded, that is if the amount of superconductor, support material and copper per turn vary across the solenoid, then D_o continues to decrease with increasing B until the inner radius of the solenoid becomes zero or the critical field is reached. This was pointed out by Roger Boom[4] in the following argument. Into a solenoid with minimum D_o for a given $\Delta\phi$, as described above, we insert a smaller solenoid with a higher B. The overall $\Delta\phi$ then increases; we can reduce it to its initial value by decreasing D_o, in contradiction to the claim that D_o was minimized.

In fact, the above argument suggests how a graded solenoid can be calculated. Because a long solenoid has no external field, each incremental thickness of the OH solenoid can be calculated without knowledge of the part of the solenoid inside it. A computer code, BGRADE, a modification of BBDOT, has been written. An outer radius, background field and increment of field are specified; and the superconductor, copper, stainless steel and helium requirements for each successive layer of the magnet are calculated, along with the cumulative field, volt-seconds and material volume. The field increment can be small, to establish the theoretical limits, or large, to represent an actual coil graded every several turns.

Figures III-9 and III-10 show the results of computations on continuously-graded OH solenoids, using BGRADE. Figure III-9 shows how the field, attainable volt-seconds and current density vary across a graded coil with a fixed outer radius of 1.0 m. Figure III-10 shows how the cost of superconductor increases with the volt-second requirement, for three

---

[3] L. R. Turner, "Limits on the Field and Rate of Change of Field in the Ohmic Heating Solenoid for TNS," Argonne National Laboratory, ANL/FPP/TM-82 (April, 1977).

[4] Roger Boom, private communication.

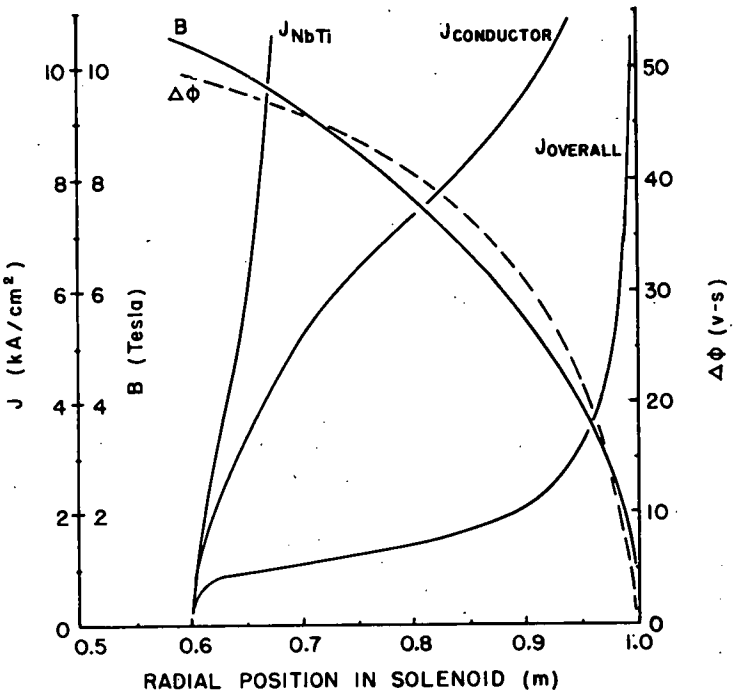

Figure III-9. Field, volt-seconds available, and current density as functions of radial position in a graded (OH) solenoid with outer radius 1.0 m.

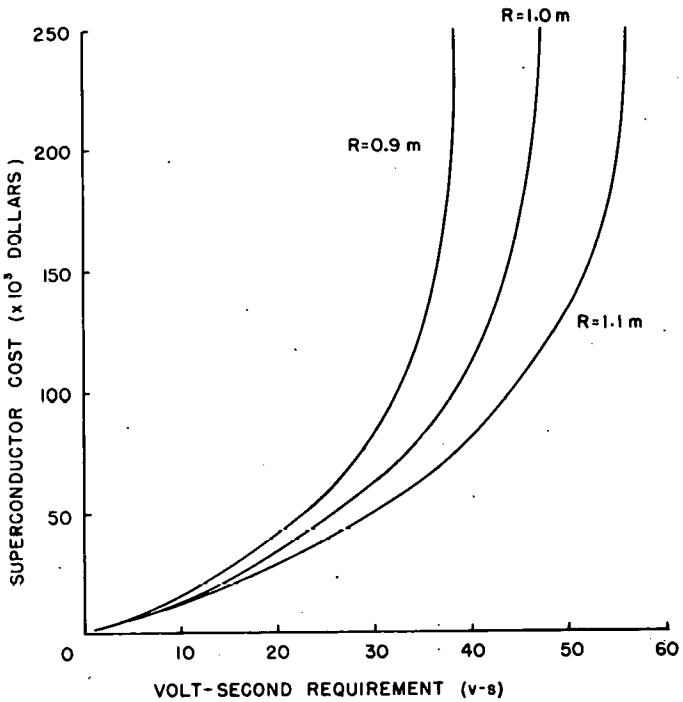

Figure III-10. Variation of superconductor cost with volt-second requirement in a graded OH solenoid, for three outer radii.

different values of the outer radius. The superconductor is costed at $60/kg, and the solenoid is assumed to be 10-m high. These results suggest that there is an economical limit to the available volt-seconds for a specified outer radius.

The graded coil, like the ungraded, is sensitive to the value of the parameters in the computation. Unlike the graded coil, the ungraded shows no clearcut optimum field and minimum diameter. The increasing cost of a smaller solenoid operating at a higher field must be balanced against the savings of an overall smaller TNS.

These results were presented in more detail at the Knoxville IEEE Symposium on Engineering Problems of Fusion Research.[5]

---

[5] L. R. Turner, "Limits on the Field of Ohmic Heating Solenoid Applied to a Tokamak TNS," Proc. of 7th Symposium on Engineering Problems of Fusion Research, Knoxville, TN (1977).

C. Penetration Shield Analysis

J. C. Jung and M. A. Abdou, Applied Physics Division

In order to study the problems associated with the radiation streaming through the rf waveguides, we have considered a labyrinth shown in Fig. III-11. A system with two bends was modeled because: (1) it is doubtful that more than two bends could be required, and (2) all the required data for zero and one bend systems can be well assessed from the two bend results.

The system in Fig. III-11 was modeled using a Monte-Carlo technique (VIM). It was found that the right angle bends were quite efficient in reducing the neutron flux streaming down the penetration. Table III-3 shows the neutron flux at various positions for a neutron wall load of 1 MW/m^2. The radiation dosage at possible window locations is also indicated. It is seen from Table III-3 that if a dielectric window is placed in duct 2, the neutron dose accumulation becomes about 1.6×10^{25} m^{-2} over a one-year reactor operation. This neutron dose corresponds to an absorbed radiation dose of $\sim 7 \times 10^{11}$ rad in an Al_2O_3 ceramic window. Removing the window to a location in waveguide 3 reduces the radiation level in the window by more than an order of magnitude compared to case (1). Indications are that the neutron induced radiation damage will not be a serious problem with the rf system at this dose level.

It is noteworthy that the neutron flux of $\sim 5 \times 10^{14}$ ($m^{-2}sec^{-1}$) at the end of duct 3 is about a factor of 2 to 6 lower than that at the end of a typical neutral beam duct of $\sim$ 5 m in length and $\sim$ 0.5 m in diameter. These results demonstrate that: (1) the radiation streaming to the vacuum pumps of the rf system is much less than that to the pumping panels in the neutral beam injector, and (2) radiation leakage to the reactor building is much higher with neutral beam systems than it is with rf systems.

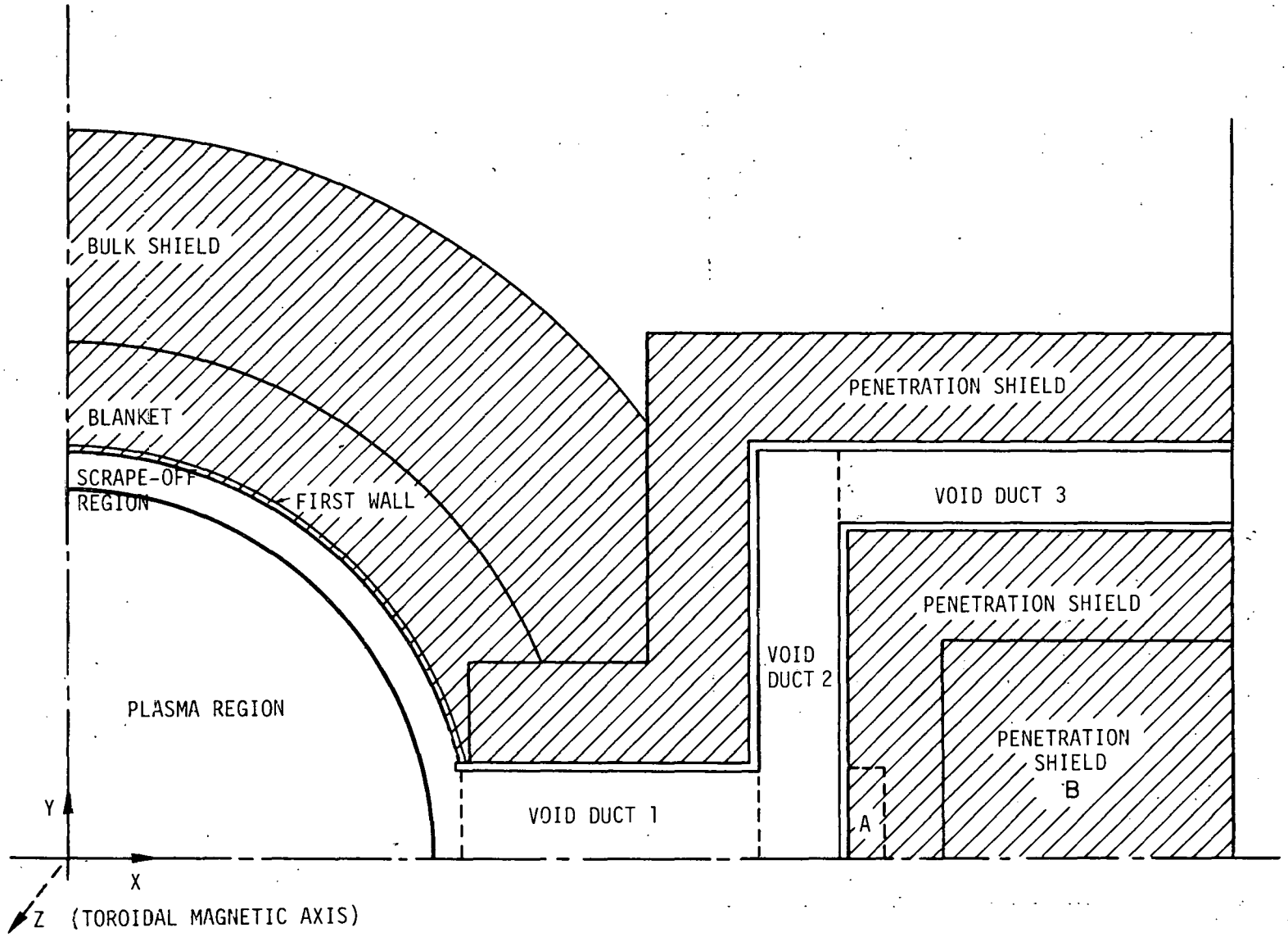

Figure III-11. A schematic of a typical rf waveguide system.

Table III-3. Neutron Dose and Flux in LHRH System

(A)	Neutron Dose in Dielectric Window (m^{-2}-yr^{-1})	
	(1) in Duct 2	1.57 (25) (± 7%)
	(2) in Duct 3	9.34 (23) (± 27%)
(B)	Neutron Flux (m^{-2}-sec^{-1})	
	(3) Along the walls of Duct 1	
	Maximum	4.69 (18) (± 2%)
	Minimum	7.89 (17) (± 10%)
	(4) Along the walls of Duct 3	
	Maximum	4.68 (16) (± 24%)
	Minimum	4.67 (14) (± 40%)

IV. FUSION SYSTEMS ENGINEERING

A. Fusion Reactor Systems Studies

M. A. Abdou, Applied Physics Division

Progress has continued in the areas of detailed subsystem studies and global parametric analyses for tokamak power plants. The present phase of the studies on the plasma, plasma driving and primary energy conversion subsystems was completed. A global parametric study on the impact of major design parameters on the economics of tokamak power plants was also completed. The results of all these studies have been documented in detail in several reports listed at the end of this section as references 1 through 11. The systems studies project has also provided support to an investigation of the goals for MFE alloy development. The results of this study have been documented in reference 12.

The following is a brief summary of the key conclusions that can be drawn from the present phase of the ANL systems studies. The reader is encouraged to consult references 1 through 12 for a more precise interpretation of these conclusions and for greater details on each specific topic.

1. In the entire range of variables examined, the cost of energy for tokamaks varies from $\sim$ 25-50 mills/kWh ($\sim$ 1200-2500 \$/kWe). This is comparable to the present range of cost estimates for LMFBR. Cost estimates for other nuclear and coal power plants are in the range of $\sim$ 14-20 mills/kWh. Since the fuel cost is negligible in tokamak fusion power plants the present trend of escalation in the fuel cost for other energy sources will make tokamaks competitive in $\sim$ 2-4 decades.

2. Tokamaks exhibit an "economy of scale". Increasing the reactor thermal power from 3000 to 5000 MWt reduces the cost of energy by $\sim$ 10-15%. The saving from further increase in reactor power is smaller. The values of parameters that characterize an optimum reactor system are, in many instances, very sensitive to the design value of thermal power output. It is very desirable for the fusion community to select a "target" thermal power for design, analysis and planning.

3. The cost of energy is very sensitive to β_t. The choice of the best parameter space for tokamaks is strongly affected by the operating value of β_t. Determining the stability limit of β_t should be a high priority goal for the fusion program.

4. Much of the economic advantages of tokamaks can be realized at a β_t of $\sim$ 6%. Most of the economic potential of tokamaks is achievable with $\beta_t \sim 8\%$. Higher β_t values -- if achievable -- are always desirable but not crucial to the prospect for economic competitiveness of commercial tokamaks.

5. The highest desirable toroidal-field strength is $\leq$ 9 T, which can be achieved by NbTi, if the β_t stability limit is $\gtrsim$ 6%. If β_t < 4%, higher fields (> 9 T) would be desirable. Such high field ($\sim$ 12 T) reactors have to be designed for large power and/or large aspect ratio. The necessity of large aspect ratio for high-field reactors implies poor utilization of the β_t stability limits that will further reduce their benefits if the attainable β_t is inversely proportional to the aspect ratio.

6. The optimum aspect ratio, A, is sensitive to the variation of β_t with A. If $\beta_t \sim 1/A$, then a favorable aspect ratio is A $\sim$ 3.5. If $\beta_t \sim 1/A^2$, then A $\sim$ 3 results in an economically favorable design.

7. The increase in the plasma current and the equilibrium field at larger elongation reduces the benefits of highly shaped plasmas. Assuming the equilibrium-field (EF) coils are located outside the bores of the TF coils, the following conclusions can be derived. If the β_t stability limit is independent of κ there is no motive for employing elongated plasmas. If $\beta_t \sim \kappa$ there is a very shallow minimum in the cost of energy in the range $1.3 < \kappa < 1.6$. A significant economic benefit from increasing κ is obtainable if $\beta_t \sim \kappa^2$.

8. Tokamaks with reactor thermal power in the range of $\sim$ 3000-6000 MWt have favorable economic conditions with plasma major radii of $\sim$ 5-8 m.

9. With proper design concepts, the blanket/shield thickness (distance in midplane from first wall to the point inside the toroidal magnet where the maximum field occurs) can be kept as small as 1 m.

10. Favorable economic conditions occur when the annealing of the superconducting magnets coincides with the replacement of the first wall.

11. Experimental data on the radiation damage to organic insulators at low temperatures ($\sim$ 4°K) are required. There is an economic incentive to develop insulators suitable for the TF coils that can operate satisfactorily up to 10^{10}-10^{11} rad.

12. Advanced structural alloys (e.g. vanadium alloys) offer the potential of reducing the cost of energy by $\sim$ 20-25% compared with stainless steel.

13. In order to limit the increase in the cost of energy due to the downtime associated with the replacement of the first wall to less than 10%, a long structure lifetime, t_w, and a short downtime, t_d, for replacement are required to meet the following criteria:

$$t_d(\text{days}) < 30 \cdot t_w(\text{years}).$$

14. The recommended highest priority goals for structural alloy development are 3 MW/m^2 neutron wall load and 4-year lifetime. More ambitious goals that can lead to a very significant economic payoff are 5 MW/m^2 and 6 years.

15. Detailed engineering and structural analysis of the first wall and blanket is required to quantitatively define the end of life criteria for the structural materials.

16. Ignoring the application of advanced power conversion cycles, there is little incentive for structural temperatures in excess of 650°C in lithium-cooled reactors. Reasonable values for the maximum operating temperature of the structure is 500°C for stainless steel and 650°C for vanadium alloys.

17. With lithium cooling and a maximum toroidal field of 8 T, the thermo-mechanical response of the first wall limits the maximum allowable neutron wall load, in the absence of a divertor, to $\sim$ 8 MW/m^2 for vanadium and 2 MW/m^2 for stainless steel. Higher fields result in a significant reduction in the allowable neutron wall load. Fields as high as 12 T may preclude the lithium cooling option.

18. The presence of a divertor (or equivalent mechanism to reduce surface heating) can increase the maximum allowable neutron wall load by $\sim$ 40 to 90% with both helium and lithium coolant.

19. For the helium coolant option, a maximum structural temperature of > 600°C is necessary to assure the attainment of attractive operationg conditions (i.e. reasonable thermodynamic efficiency).

20. The power supplies for the poloidal coils represent a significant cost item. The use of a conventional motor-generator-flywheel set as a central energy storage device leads to an increase in the plant cost as large as 10%. There is a strong economic incentive for the development of homopolar generators and superconducting energy storage devices.

---

1 M. A. Abdou, J. N. Brooks, C. Dennis, D. A. Ehst, K. Evans, Jr., R. Kustom, V. A. Maroni, R. Mattas, J. Norem, B. Misra, D. L. Smith, W. M. Stacey, Jr., H. C. Stevens and L. R. Turner, "Parametric Systems Analyses for Tokamak Power Plants," Argonne National Laboratory, ANL/FPP/TM-97 (October, 1977).

2 W. M. Stacey, Jr. and M. A. Abdou, "Tokamak Fusion Power Reactors," Argonne National Laboratory, ANL/FPP/TM-83 (1977).

3 D. Ehst, K. Evans, Jr. and W. M. Stacey, Jr., "A Systematic Survey of Tokamak Reactor Physics Design Parameters," Argonne National Laboratory, ANL/FPP/TM-95 (1977).

4 J. Brooks, R. L. Kustom and W. M. Stacey, Jr., "Plasma Driving Systems Requirements for Commercial Tokamak Fusion Reactors," Argonne National Laboratory, ANL/FPP/TM-87 (1977).

5 L. R. Turner and M. A. Abdou, "Computational Model for Superconducting Toroidal-Field Magnets for a Tokamak Reactor," Argonne National Laboratory, ANL/FPP/TM-88 (1977).

[6] R. F. Mattas and D. L. Smith, "Modeling of Life-Limiting Properties of Fusion Reactor Structural Materials," Argonne National Laboratory, ANL/FPP/TM-84 (1977).

[7] B. Misra and V. A. Maroni, "Thermal Hydraulic Analysis of Two Fusion Reactor First-Wall/Blanket Concepts," Argonne National Laboratory, ANL/FPP/TM-94 (1977).

[8] B. Misra, H. C. Stevens and V. A. Maroni, "Thermal Hydraulic and Power Cycle Analysis of Liquid Lithium Blanket Designs," in Proc. 1977 National Heat Transfer Conference, August 15-17, 1977, Salt Lake City, Utah.

[9] L. R. Turner and M. A. Abdou, "Computational Model for Superconducting Toroidal-Field Magnets for a Tokamak Reactor," in Proc. 7th Symposium on Engineering Problems of Fusion Research, Knoxville, TN., 1977 (IEEE), to be published.

[10] J. Brooks, "Plasma Driving System Requirements for Commercial Tokamak Fusion Reactors," Proc. 7th Symposium on Engineering Problems of Fusion Research, Knoxville, TN., 1977 (IEEE), to be published.

[11] M. A. Abdou, "Radiation Considerations for Superconducting Fusion Magnets," Argonne National Laboratory, ANL/FPP/TM-92 (1977).

[12] M. A. Abdou, S. D. Harkness, S. Majumdar, V. Maroni and B. Misra (Argonne National Laboratory) and B. Cramer, J. Davis, D. Defreece and D. Kummer (McDonnell Douglas Astronautics Company), "The Establishment of Alloy Development Goals Important to the Commercialization of Tokamak-Based Fusion Reactors," Argonne National Laboratory, ANL/FPP/TM-99 and McDonnell Douglas, MDCE-1743 (November, 1977).

B. Development of Blanket Processing Technology for Fusion Reactors

The program[13-15] under way in the Chemical Engineering Division to initiate the development of processing technology for liquid lithium fusion reactor blankets is continuing. Progress during the fourth quarter of FY-1977 is summarized below.

---

[13] W. M. Stacey, Jr., et al., "Fusion Power Program Quarterly Progress Report: April-June, 1977," Argonne National Laboratory, ANL/FPP-77-2 (1977).

[14] W. M. Stacey, Jr., et al., "Fusion Power Program Quarterly Progress Report: January-March, 1977," Argonne National Laboratory, ANL/FPP-77-1 (1977).

[15] W. M. Stacey, Jr., et al., "Fusion Power Program Quarterly Progress Report: October-December, 1976," Argonne National Laboratory, ANL/FPP-76-6 (1977).

1. Lithium Processing Test Loop (LPTL)

J. R. Weston and V. A. Maroni, Chemical Engineering Division

Construction of the LPTL is nearly completed. The thermocouples, trace heating units, leak detection and containment wraps and insulation have all been installed. Work on the instrumentation console, power buss interface and terminal box hookups is finished. Connection of the heaters, thermocouples, leak circuits and dump valve circuits to the terminal boxes is nearing completion. Some portions of the counter weighting system and the valve operator hookups remain to be installed. Installation of the hydrogen meter detection and cover gas control systems has been completed and checkouts of these systems are progressing. The lithium carboy containing $\sim$ 210 lbs. of lithium, has been received from the vendor and preparations for the filling operation are being made. A series of tests of the thermal expansion characteristics of the LPTL piping system and completion of documentation for the LPTL design/safety/operation review (to be conducted in-house) are the major items remaining to be completed prior to startup.

2. Support Activities

B. Misra and R. M. Yonco, Chemical Engineering Division

The electrical short in the lithium mini-test loop (LMTL)[13] leak detection circuit has been repaired and the trace heating system is presently being modified to permit higher thermal power operation and more easily controlled temperature distributions. As soon as these modifications have been completed we will resume tests of the zirconium getter-trap. Operating temperatures of 550°C in the main loop and 650°C in the getter trap are planned. Results of sampling studies performed just prior to the LMTL shutdown[13] at the end of the third quarter of FY-1977, indicated that the nitrogen level was in the range of 280-310 wppm during the final stages of the operating campaign carried out with a 600°C getter temperature.

The half-scale glass mockup of the salt processing tank built into the LPTL is nearly ready for testing. This experiment will use an aqueous phase and a denser organic phase (probably bromobenzene) to simulate the lithium and salt phases that will be present in the LPTL. An acid-base titration reaction employing an indicator dye (ethyl red) and involving addition of benzoic acid to the organic phase and ammonia to the aqueous phase will be used to evaluate interface mixing kinetics by following the color change of the indicator. Fabrication of a set of electrical shorting probes to monitor liquid level locations in the glass mockup has been completed and final installation of the microprocessor driven control circuit[13] is in progress.

C. Safety Studies of Fusion Concepts

I. Charak, Reactor Analysis and Safety Division

In this quarter, the first-wall thermal model was refined to account for time-dependent burn-cycle heating rates. Also, the consequences of a plasma dump on the first wall were studied.

1. First-wall Thermal Model

The quasi-steady-state temperature calculations described in the previous quarterly progress report[16] have been refined and extended. In particular, whereas the earlier calculations were based on a constant heating rate over the burn time, the present results were based on the actual burn cycle dynamics calculated for the ANL/EPR. The power profile was based on the distribution given earlier.[17] The resulting curve for neutron heating normalized to a neutron wall loading of 1 MW/m^2 is shown in Fig. IV-1. This work is based on a total surface area of 400 m^2.

Two basic first-wall configurations have been studied: a bare, water-cooled steel wall and a 1-cm thick graphite first wall (or liner) which radiates its absorbed energy to a water-cooled steel vacuum vessel. The peak steel and peak graphite-and-steel temperatures for these cases are shown in Figs. IV-2 and IV-3, respectively, for a neutron wall loading of 1 MW/m^2, a 65-s burn time and a 30-s dwell time. Similar calculations have been performed for other values of wall loading and dwell time, as well as for variable material thermophysical properties.

A summary of important temperature differences for both wall configurations for an average neutron wall loading of 1 MW/m^2 is given in Table IV-1.

2. Plasma Dump Thermal Model

As noted earlier,[16] an effort is underway to determine the thermal effects of a plasma quench on the first wall. Since deposition of the stored plasma energy might occur over a very short burst time (e.g., milliseconds) and over less than the full first-wall surface area, the potential for material removal by ablation during such a burst certainly exists. In order to study this phenomenon, a code developed as a component of a larger LMFBR accident analysis code was appropriately modified and used.[18] This code treats a section of the first wall in one dimension. The innermost (i.e., plasma-facing) region is considered an ablation region and is dimensioned thick

---

[16] W. M. Stacey, Jr., et al., "Fusion Power Program Quarterly Progress Report, April-June, 1977," Argonne National Laboratory, ANL/FPP-77-2 (1977).

[17] W. M. Stacey, Jr., et al., "Fusion Power Program Quarterly Progress Report, January-March, 1977," Argonne National Laboratory, ANL/FPP-77-1, p. 35 (1977).

[18] S. J. Hakim and R. J. Henninger, Argonne National Laboratory, private communication.

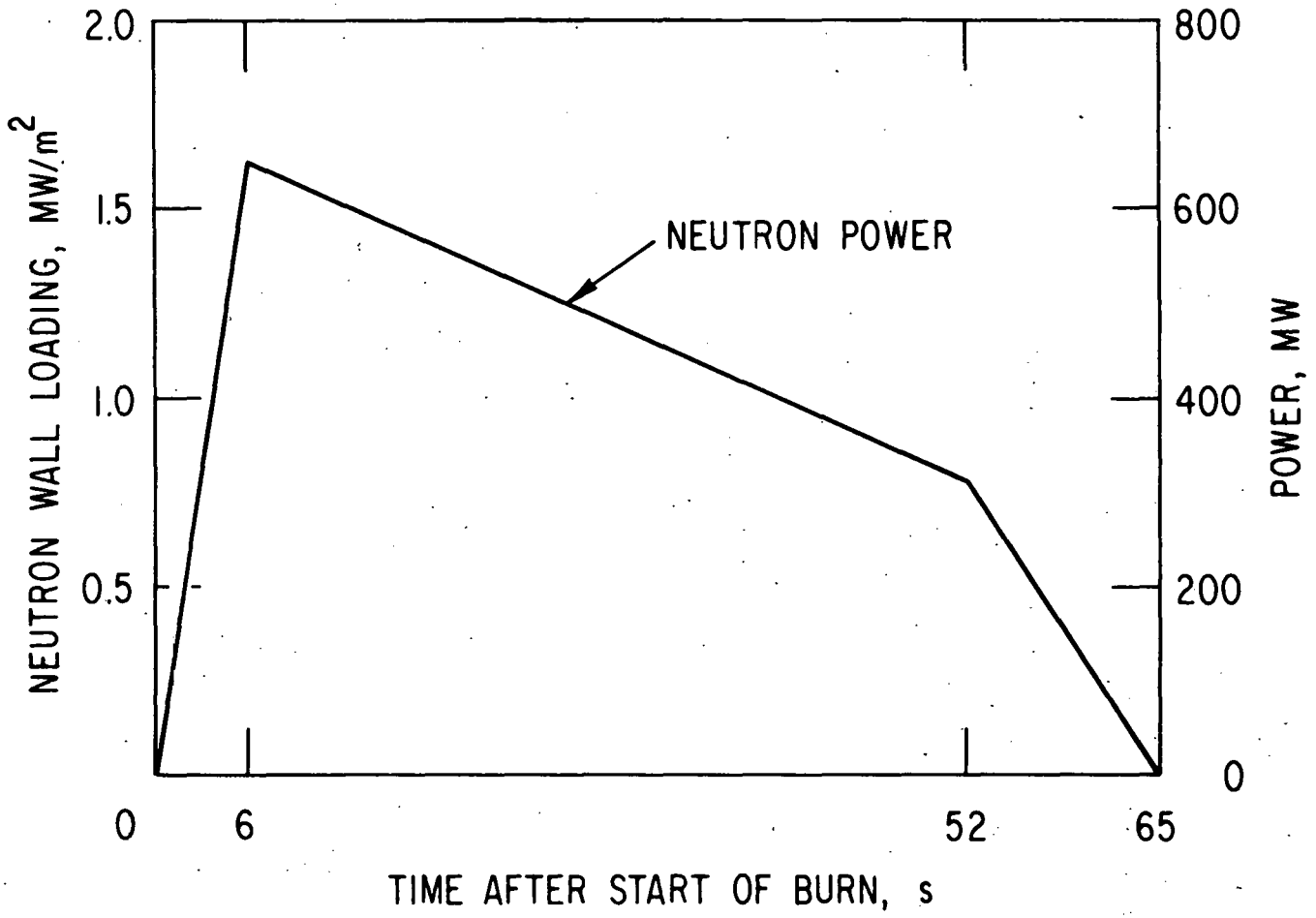

Figure IV-1. Neutron power for reference burn cycle normalized to a wall loading of 1 MW/m^2.

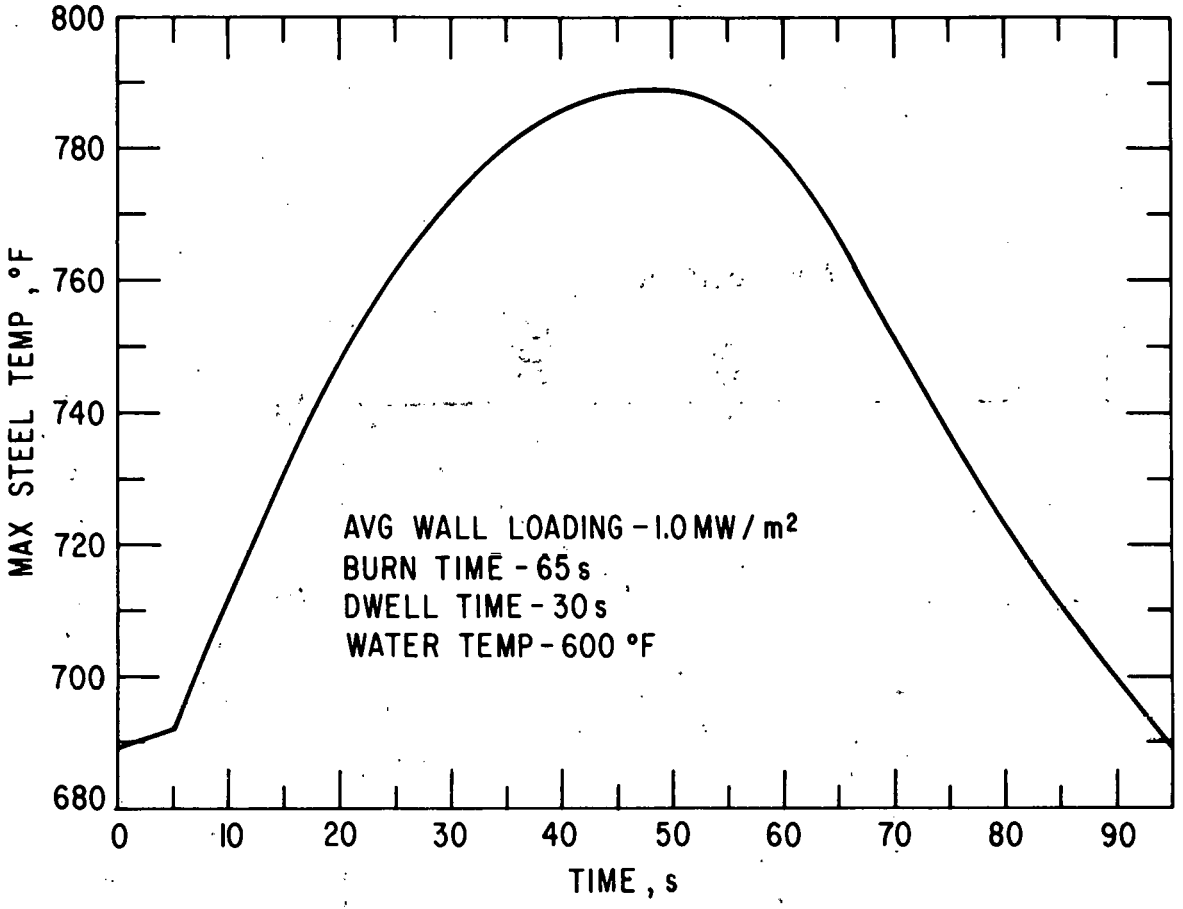

Figure IV-2. Peak Steel Temperature for Typical Burn Cycle.

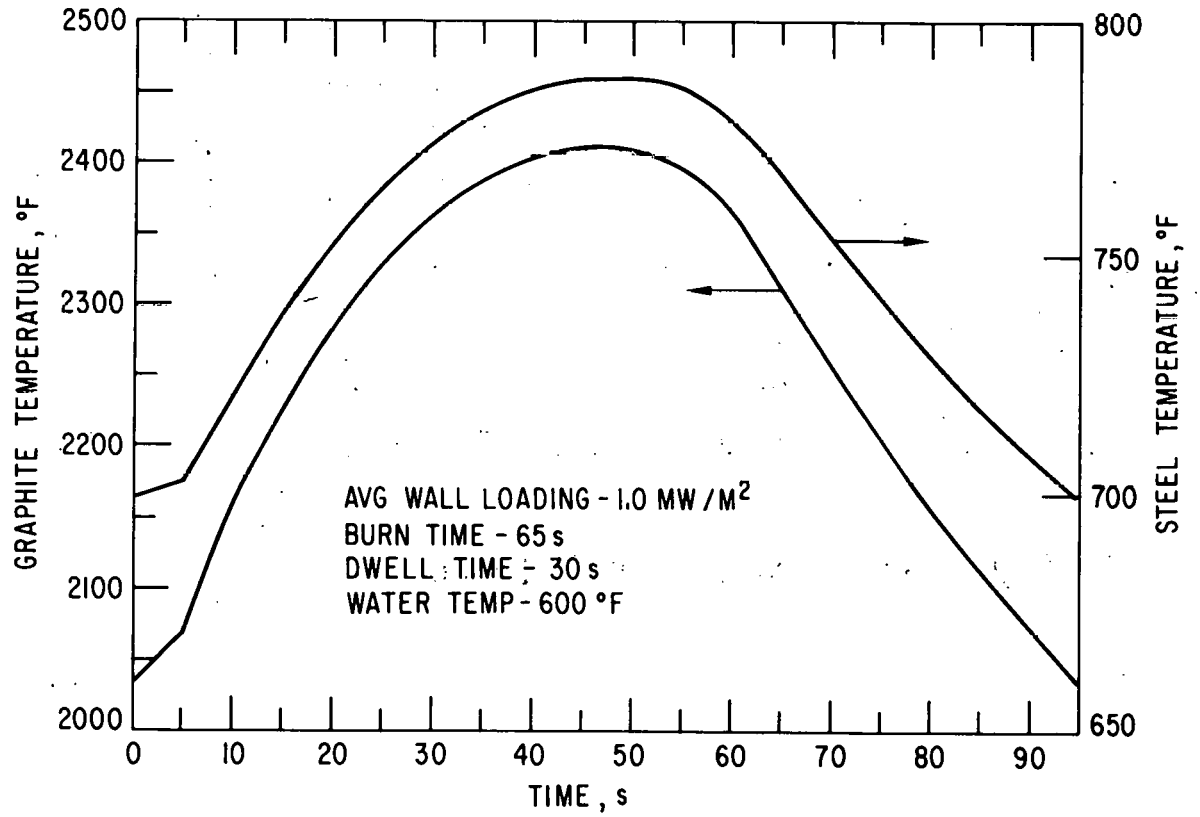

Figure IV-3. Peak steel and graphite temperatures for typical burn cycle.

Table IV-1. First Wall/Vacuum Wall Temperature Differences [F(C)]

Composite Wall	Dwell Time, s	
	15	30
Liner ΔT		
End of burn	62(34)	58(32)
End of dwell	44(24)	36(20)
At peak temp.	112(62)	100(56)
Steel ΔT		
End of burn	93(52)	85(47)
End of dwell	70(39)	46(26)
At peak temp.	102(57)	93(52)
ΔT over burn cycle		
Liner hot spot	293(163)	338(188)
Steel hot spot	67(37)	80(44)
Bare Steel Wall		
Steel ΔT		
End of burn	143(79)	135(75)
End of dwell	111(62)	77(43)
At peak temp.	113(63)	104(58)
ΔT over burn cycle at hot spot	74(41)	100(56)

enough so that some material would remain even if all the energy were available to ablate the material. This region is then subdivided into as many small subregions as desired. The remainder of the wall is divided into two equally thick regions. Although the model can account for heat loss from the wall, the time scale for the burst is so short that, for practical purposes, a heat sink is ineffective.

Calculations of material ablation were done for both a steel and graphite first wall. The heat of ablation (vaporization for the steel and sublimation for the graphite) was taken as 1,564 and 14,250 cal/gm, respectively. The results are given in Figs. IV-4 and IV-5, with the total stored energy commensurate with an average operating wall loading of 1 MW/m^2. Note that the maximum theoretical material ablation loss (i.e., with instantaneous energy deposition) is essentially achieved for very small area fractions (e.g. $\sim$ 10%) or very short disruption times (e.g. $\sim$ 0.1 ms).

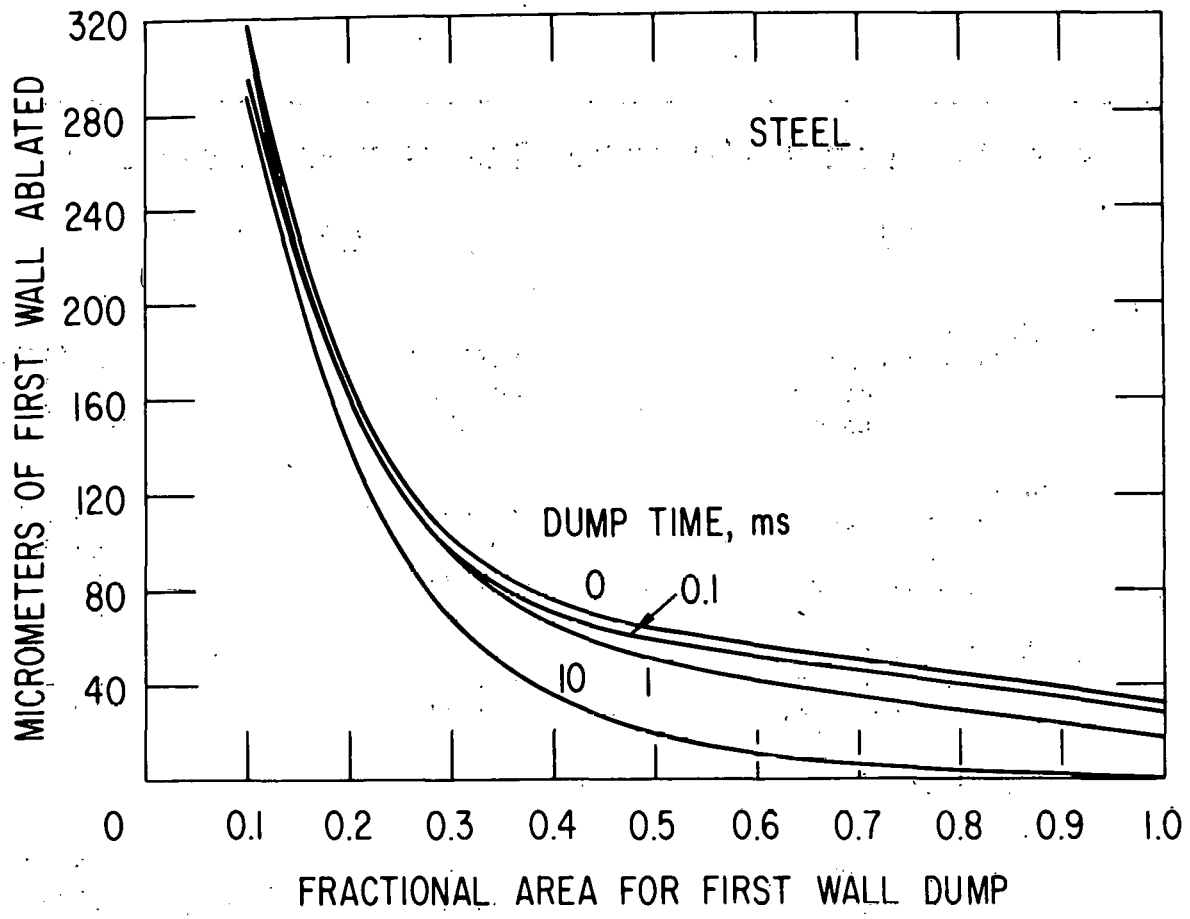

Figure IV-4. Ablation of stainless steel first wall following plasma disruption.

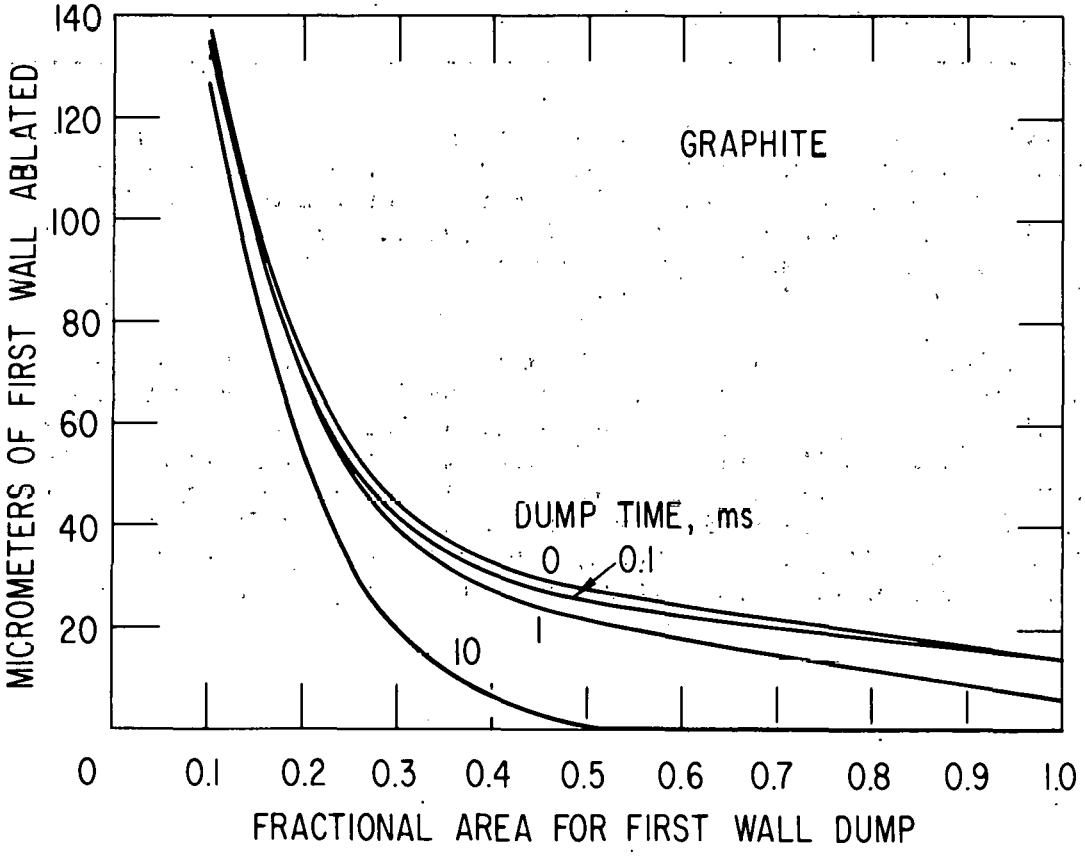

Figure IV-5. Ablation of graphite first wall following plasma disruption.

3. Analysis of Tritium Soaking Mechanisms

R. G. Clemmer, R. H. Land and V. A. Maroni, Chemical Engineering Division

This activity has involved a family of coordinated studies[19-22] aimed at developing a basis for understanding the effects of selected reaction and soaking mechanisms on large-scale air detritiation operations. A computer code (TSOAK) has been formulated to model these mechanisms[19,22] and a small-scale experimental apparatus has been set up to test selected features of the model.[21,22] Progress during the fourth quarter of FY-1977 is described below:

Following the experimental studies described in the previous progress report,[21] an attempt was made to derive $H_2O + T_2 \rightarrow HTO + HT$ reaction rate constants, HTO adsorption coefficients and HTO desorption coefficients for the experimental enclosure[21] using the results presented in Fig. IV-7 of reference 21. This was done by adjusting the corresponding reaction, adsorption and desorption (release) parameters in TSOAK until a fit to the experimental cleanup curves was obtained. By properly adjusting these three parameters it was, in fact, possible to obtain exact fits to the experimental curves. The observed cleanup curves for two experimental cases are compared to the corresponding ideal cleanup curves in Fig. IV-6. Also shown in the figure are the data points for the TSOAK fit to the observed curve. (An asymptote of 4 $\mu Ci/m^3$ was used in both the ideal and TSOAK calculations, and it is this asymptote which causes the curvature in the ideal curve.)

The experiment plotted on the left-hand side of Fig. IV-6 was performed by pulling clean air into the enclosure and exhausting the exit gas to a fume hood. This experiment, therefore, represents the condition of having a 100% efficient scrubbing system. The experiment plotted on the right-hand side of Fig. IV-6 was performed under identical conditions (release size, flow rate, etc.) except that the enclosure atmosphere was circulated in a closed loop through the oxidizer bed and molecular sieve bed. The increased departure from ideal behavior in the latter case (compared to the once-through flushing case) is attributable to a less than 100% HTO scrubbing efficiency

---

19 W. M. Stacey, Jr., et al., "Fusion Power Program Quarterly Progress Report, October-December, 1976," Argonne National Laboratory, ANL/FPP-76-6 (1977).

20 W. M. Stacey, Jr., et al., "Fusion Power Program Quarterly Progress Report, January-March, 1977," Argonne National Laboratory, ANL/FPP-77-1 (1977).

21 W. M. Stacey, Jr., et al., "Fusion Power Program Quarterly Progress Report, April-June, 1977," Argonne National Laboratory, ANL/FPP-77-2 (1977).

22 R. G. Clemmer, R. H. Land, V. A. Maroni and J. M. Mintz, "Simulation of Large Scale Air-Detritiation Operations by Computer Modeling and Bench-Scale Experimentation," Argonne National Laboratory, ANL/FPP-77-3 (November, 1977); also published in abridged form in the Proceedings of the Seventh IEEE Symposium on Engineering Problems of Fusion Research, October 25-28, 1977, Knoxville, Tennessee.

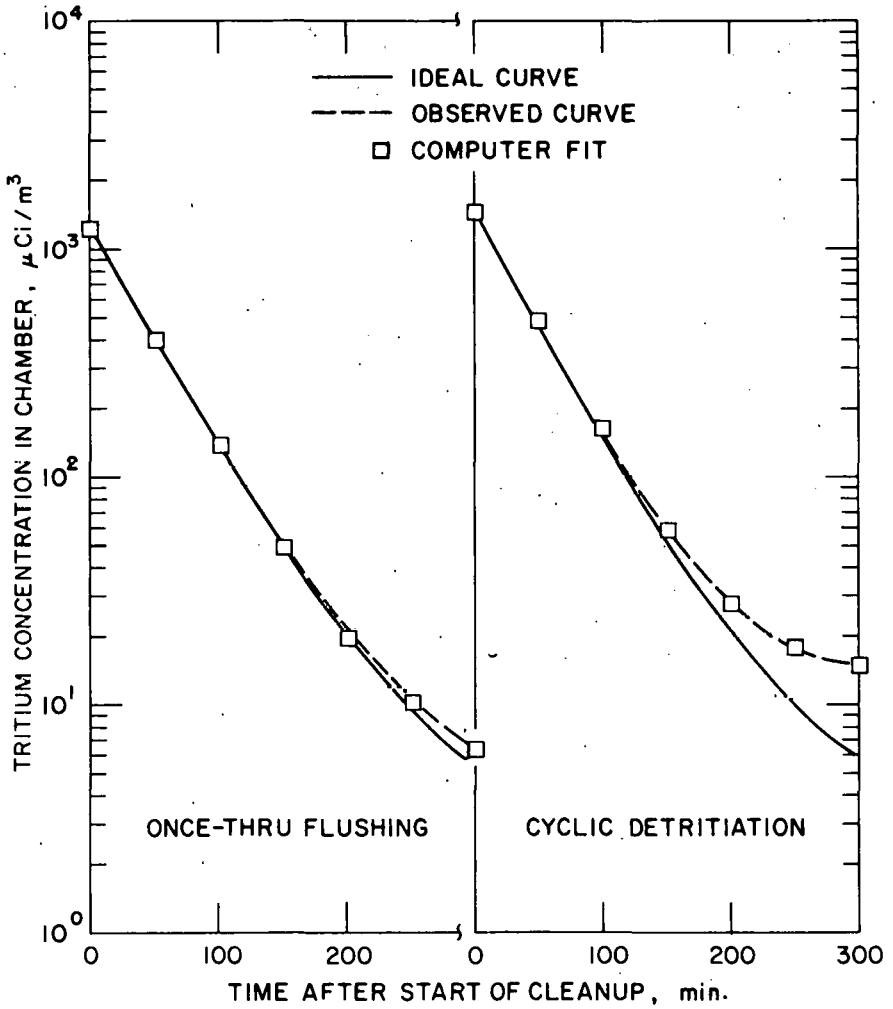

Figure IV-6. Comparison of observed versus ideal and TSOAK calculated results for two air detritiation experiments (flow rate = 1 liter/min, enclosure volume 50 liters).

of the molecular sieve bed. While on first thought this appears to be the result of having an inadequately designed scrubbing system, it does not take much of a departure from 100% efficiency to create a sizeably increased apparent HTO production rate in the enclosure; i.e., less than 1% reduction in efficiency would be more than adequate to explain the differences in Fig. IV-6. Table IV-2 lists the TSOAK-derived fitting parameters for the two experiments in Fig. IV-6 and for two other interesting cases presented in reference 21 (Fig. IV-7). Particularly worthy of note are the substantial changes in all three parameters when the fan and hot plate are both operating. The 400-fold increase in the required reaction rate parameter is considered to be well above the uncertainties associated with the computer model and with the experiment itself.

Table IV-2. Summary of Curve Matching Parameters Obtained from TSOAK Fits to Enclosure Detritiation Experiments

Condition	Reaction Rate Parameter[a] ($m^3/\mu Ci$-min)	Adsorption Rate Parameter[a] ($\mu Ci/m^2$-min)	Release Rate Parameter[a] (%/min)
Typical Literature Data	10^{-12}-10^{-14}	--	--
Enclosure: Fan Off, Plate Cool	1×10^{-5}	3×10^{-4}	3
Enclosure: Fan On, Plate Cool	5×10^{-5}	2×10^{-4}	3
Enclosure: Fan On, Plate Hot[b]	4×10^{-4}	5×10^{-5}	12
Enclosure: Once-Through Flushing	1×10^{-6}	2×10^{-4}	3

[a] See reference 22 for a discussion of the derivation and implementation of these parameters.

[b] Plate heated to $\sim$ 200°C.

D. Cross Section Measurements, Evaluations and Techniques

1. Neutron Inelastic Scattering Studies for Lead-204

D. L. Smith and J. W. Meadows, Applied Physics Division

A 9.57-g sample of lead metal, enriched to 99.7% ^{204}Pb, has been used in an investigation of neutron inelastic scattering from this rare isotope at the Argonne National Laboratory Fast-Neutron Generator Facility. Neutron excitation of the 66.9-m isomeric state at 2.186 MeV in ^{204}Pb has been measured from near threshold to $\sim$ 10 MeV using activation techniques. Cross sections and a value for the isomeric half life have been derived from these data. Time-of-flight techniques were employed to measure spectra of promptly-emitted gamma rays from the ^{204}Pb(n;n',γ)^{204}Pb reaction at neutron energies $\leq$ 3 MeV. Cross sections and angular distributions have been derived from these data for several of the stronger transitions.

2. Graphical Representation of Neutron Differential Cross Section Data for Reactor Dosimetry Applications

D. L. Smith, Applied Physics Division

The need for improved understanding of the relationships between available differential and integral data for neutron reactions used in reactor dosimetry has prompted investigation of a method for graphically representing experimental differential data in a form which appears to be quite useful for dosimetry applications. The method involves weighting the differential cross sections by spectral functions and plotting these values. Graphs of this form clearly indicate which differential data are important for spectrum unfolding applications. Simultaneous plots of experimental and evaluated differential cross sections -- weighted by spectral functions -- provide a means for comparing evaluations from the point of view of their impact on specific dosimetry applications.

3. Evaluated Nuclear Data File of Th-232

J. Meadows, W. Poenitz, A. Smith, D. Smith, J. Whalen and R. Howerton*, Applied Physics Division

An evaluated nuclear data file for elemental thorium has been prepared. The file extends over the energy range 0.049 (i.e., first inelastic threshold) to 20.0 MeV and is formulated within the framework of the ENDF system. The input data base, the evaluation procedures and judgments and ancillary experiments carried out in conjunction with the evaluation are outlined. The file includes: neutron total cross sections, neutron scattering processes, neutron radiative capture cross sections, fission cross sections, (n;2n) and (n;3n) processes, fission properties (e.g., nu-bar and delayed neutron emission) and photon production processes. Regions of uncertainty are pointed out particularly where new measured results would be of value. The file is extended to thermal energies using previously reported resonance evaluations thereby providing a complete file for neutronic calculations.

* Lawrence Livermore Laboratory.

4. Evaluated Fast Neutron Cross Sections of Uranium-238

W. Poenitz, E. Pennington, A. Smith and R. Howerton*, Applied Physics Division

An evaluated fast neutron data file of ^{238}U is presented in the ENDF/B format. The incident energy range extends from 0.045 to 20.0 MeV. The file content consists of: (1) neutron total cross sections, (2) fission cross sections, neutron emission spectra and associated properties, (3) neutron radiative-capture cross sections, (4) (n;2n') and (n;3n') processes, and (5) photon-production cross sections and spectra. The methodology of the file derivation is outlined. File content is graphically illustrated and uncertainty estimates are given. Comparisons with comparable portions of ENDF/B-IV are made and some large differences are noted. Some results of integral "benchmark" tests using this file are outlined. Many of the components of this file are those explicitly submitted for ENDF/B, Version V.

* Lawrence Livermore Laboratory.

5. Titanium-II: An Evaluated Nuclear Data File

C. Philis,* R. Howerton** and A. B. Smith, Applied Physics Division

A comprehensive evaluated nuclear data file for elemental titanium is outlined including definition of: the data base, the evaluation procedures and judgments and the final evaluated results. The file describes all significant neutron-induced reactions with elemental titanium and the associated photon-production processes to incident neutron energies of 20.0 MeV. In addition, isotopic-reaction files, consistent with the elemental file, are separately defined for those processes which are important to applied considerations of material-damage and neutron-dosimetry. The file is formulated in the ENDF format. This report formally documents the evaluation and, together with the numerical file, is submitted for consideration as a part of the ENDF/B-V evaluated file system.

* Bruyeres le Chatel, France.

** Lawrence Livermore Laboratory.

V. MAGNETIC SYSTEMS

A. Energy Storage and Transfer Program

R. Fuja, R. L. Kustom, R. P. Smith and R. Wehrle, Accelerator Research Facilities Division

The energy storage and transfer systems described in previous Fusion Power Program Quarterly Reports have been built and preliminary tests have been completed.

The model homopolar generator (Hope 1), used for energy reversal in the OH coil of TEPR, has been assembled and preliminary tests have been completed. The first tests performed on the homopolar generator were designed to measure the brush voltage drop. A 10-V, 100-A power supply was connected across the cylindrical drum and brush support structure. The radial field was set at approximately 0.93 T. The air bearing pressure was set at 10 psi and the brush pressure had to be set to 30 psi before we were fairly confident that the brushes were making electrical contact. With the high brush pressure we were unable to rotate the drum by hand. The power supply was turned on and after several seconds the drum reached an angular velocity of 3500 rpm, the current through the drum was 70 A. The voltage drop across the brushes was calculated at 2.3 to 2.4 V. Because of the high brush pressure and large brush voltage drop, the brush support structure is to be modified, but before disassembly energy transfer was attempted. The 13.6 mh inductor was energized to 500 A and the current was switched through the homopolar generator. These tests were performed several times and confirmed the need for brush modifications. The switching circuits required for energy reversal worked properly. A schematic diagram of the Hope 1 system is shown in Fig. V-1. The brush support structure was removed and is undergoing modifications. The brush contact area will be increased and the brush pressure mechanism will be modified to allow for freer movement of the brushes.

The irregularities in the field between the pole tips along the ϕ and z axis, of a cylindrical coordinate system have been reduced to $\pm$ 1% of the total field which is about 1.0 T. The modification will be completed shortly and testing will resume thereafter.

Studies for the control of energy transfer from the inductor-converter (IC) brudge at a controlled and variable rate have been completed. An Intel 80/20 microcomputer was purchased to function as the IC bridge controller. The operation and programming of the microcomputer is under study and soon the programs needed to control the IC bridge will be developed. The input and output devices needed for variable energy transfer rate control are being determined and the interface of these devices to the microcomputer will be designed and assembled.

When this system is developed it should allow us to control any size three-phase IC bridge arrangement. The next step in the program will then be to develop a bridge which can switch 10 kA.

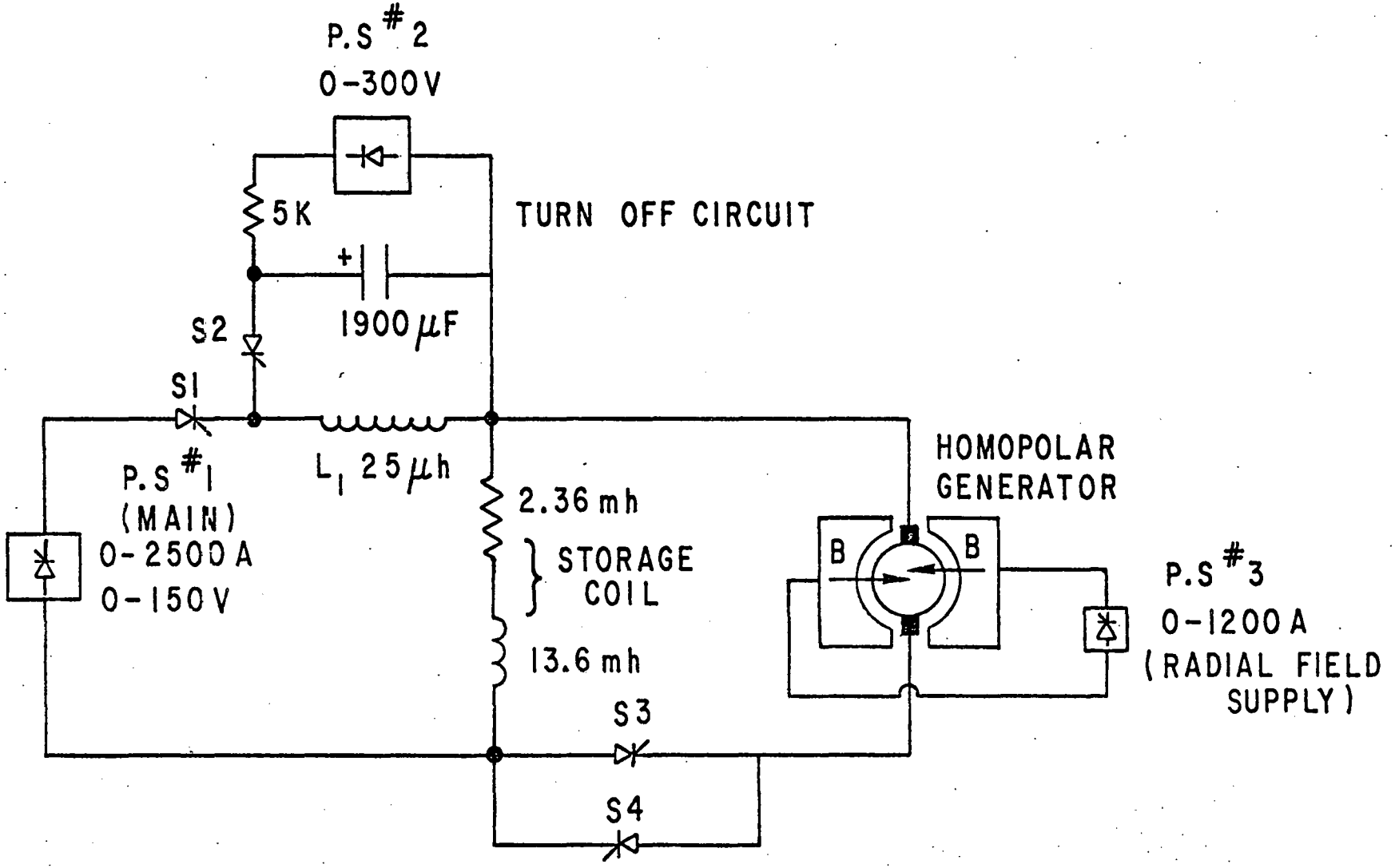

Figure V-1. Hope 1 Schematic Diagram

B. Negative Ion-Source Development

1. Charge Exchange H^- Ion Sources

J. A. Fasolo and H. R. Hiddleston, Accelerator Research Facilities Division

A test in which output from the unmodified 30 Hz tandem acceleration H^- source was passed through a recirculating supersonic sodium vapor jet being developed for use with a modified version of the source has been repeated. (The first test was discussed in the previous report.) In the second test, the sodium cell was isolated so that it could be biased with respect to ground potential. In addition, two rings with apertures slightly larger than the cell entrance and exit apertures were mounted just in front of the entrance aperture and beyond the exit aperture. The rings were mounted on insulators and connected together and to a power supply. The rings and the cell could be biased independently. With the rings and cell grounded, the main result of the previous test (a factor of two decrease in collected H^- current when the sodium was heated to operating temperature) was reproduced. The effects of bias voltages on the cell and/or the rings were then studied and some results are shown in Fig. V-2. The average beam current increases when a negative bias is placed on the cell or the rings. Negative biases on the cell and rings are better (give more average beam) than no biases but not as good as bias on the cell only. The beam becomes more noisy when the cell is biased. In no case did a bias voltage raise the collected beam current to a value equal to or in excess of the value obtained without sodium vapor.

The sodium cell test was conducted with a high-perveance, parallel-ribbon extraction geometry in which a positive ion beam is extracted from the source plasma through a single-aperture, 1.96-cm diameter source grid which is followed by a parallel-ribbon W-3Re extraction grid with 107 ribbons, 5.1×10^{-3} cm wide, spaced 1.78×10^{-2} cm center-to-center. After the test was completed, the source and extractor grids were replaced by two aligned multiaperture grids. Each of the copper-tungsten grids has 299 0.081-cm diameter apertures within a 1.96-cm diameter circle. The grids are slightly spherical, with a radius of curvature $R \approx 1.0$ m and produce a slightly divergent beam.

The grids were curved to give the kind of controlled expansion that has been achieved in ion thrusters and fusion ion sources. With previous aligned grid sets, a rate effect in which collected beam current decreased with increasing pulse rate was observed. This effect, believed to be due to uncontrolled thermal expansion (oil canning), has not been observed with the shaped grids.

During initial voltage conditioning, a 15.4 mA, 30 Hz H^- beam (Fig. V-3) was obtained with an extraction voltage of $\sim$ 15.2 kV just before the run was terminated by a power supply failure. If, as expected, the beam current varies as $V^{3/2}$ up to the voltage holding limit of $\sim$ 24 kV, the design current of 30 mA will be obtained.

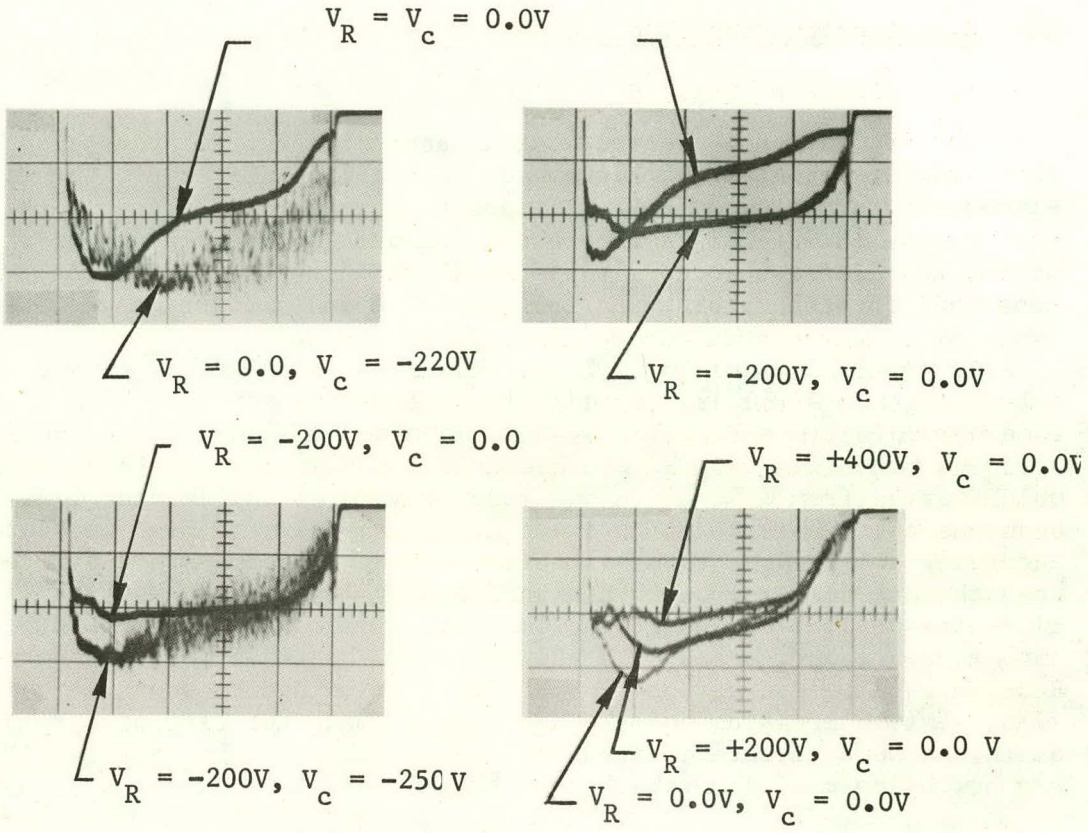

Figure V-2. Effects of ring bias voltage V_R and cell bias voltage V_c on collected H^- beam currents. Beam from unmodified charge exchange source, through sodium vapor cell. 2 mA/div., 100 μs/div.

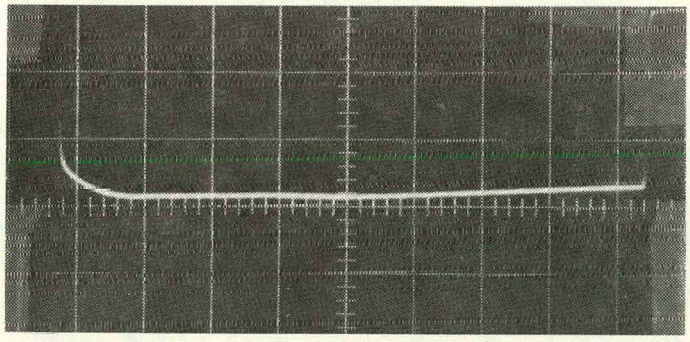

Figure V-3. 30 Hz H^- beam from charge exchange source with curved multi-aperture grids. 5.5 mA/div., 50 μs/div., ∿ 15.2 keV extraction voltage.

2. Direct Extraction H^- Source

J. A. Fasolo, Accelerator Research Facilities Division

The Argonne Penning-type, cesium-activated surface plasma source, built from drawings provided by Los Alamos Scientific Laboratory, was taken to Los Alamos and installed on P. W. Allison's test stand in place of the LASL source on July 26, 1977. This source was in almost all respects an exact duplicate of the Los Alamos source;[1] it was modified in several instances to simplify construction without altering the discharge and extraction geometries.

A normal 75-A arc and a 75-mA, 13-keV H^- beam were obtained on July 26. The pulse length was 750 μs and the pulse repetition rate was 12 Hz. The beam was somewhat noisy (see Fig. V-4). Next morning, the source was run at 37 Hz with a 500 μs pulse length. With a bistable arc of ∿ 25 A, a 16 keV bistable beam which varied from ∿ 30 mA in one mode to ∿ 40 mA in the other was obtained. The beam was quite noisy, with a lower noise level in the high current mode. According to Allison, this bistable behavior is temperature related; it occurs when the average arc power is significantly less than the value (∿ 50 W) which gives the optimum cesium generation rate from the $Cs_2Cr_2O_7$ + Ti mixture packed into a cavity in the source anode, which is heated by the discharge. In a Russian Penning source[2] and in the Fermilab magnetron source,[3] as recently modified,[4] external cesium boilers are used to make the rate of arrival of cesium at the cathode surface independent of arc power. (The LASL and ANL sources are now being modified to achieve the same end.)

The gas flow was pulsed with the LASL gas valve, which had been exposed to excessive heat and was not working properly. The pulsed gas flow of 18 cm^3/min reported by Allison in reference 1 for a 100 mA beam was lower than any of the flows measured during testing of the ANL source. The gas valve voltage pulse widths used by Allison are more than an order of magnitude larger than those used at Novosibirsk and at Fermilab, where the length of the applied voltage pulse is 100 μs. (The hydrogen consumption per pulse in the Russian source of reference 2 is ∿ 0.079 atmospheric cm^3/min, or about 3.0 cm^3/min at a pulse repetition rate of 37 Hz.) Allison prefers to work with dc gas flows and has not devoted much time to minimizing gas consumption.

---

1 P. W. Allison, "A Direct Extraction H^- Ion Source," IEEE Trans. on Nuclear Science, NS-24 (3), p. 1594 (1977).

2 G. I. Dimov, G. Ye. Dereviankin and V. G. Dudnikov, "A 100-mA Negative Hydrogen-Ion Source for Accelerators," IEEE Trans. on Nuclear Science, NS-24 (3), p. 1545 (1977).

3 C. Schmidt and C. Curtis, "Negative Hydrogen-Ion Program at Fermilab," Proc. Proton Linear Accelerator Conference, Chalk River, Ontario, Canada, Report No. AECL 5677 (1976).

4 C. Schmidt, private communication.

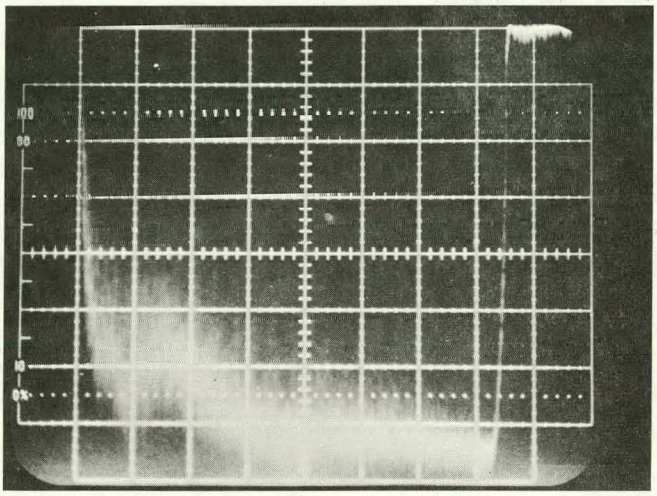

Figure V-4. 12 Hz H^- beam from direct extraction Penning source. 10 mA/div., 100 μs/div., 11.75 keV.

The immediate objective of the Penning source program at Argonne is to produce an operational source for direct H^- injection into the Zero Gradient Synchrotron (ZGS) and/or Booster II as quickly as possible. The beam intensities and duty cycles required for these applications were achieved during the initial tests at Los Alamos.

As noted above, during these tests the arc and beam currents were quite noisy and gas consumption was excessively high. Efforts to eliminate these problems are underway.

In view of the encouraging results obtained during the Los Alamos tests, construction of a test stand for the ANL source is now proceeding on an accelerated schedule.

VI. APPLIED PLASMA PHYSICS

A. Spitzer Function of a Multispecies Plasma

C. D. Boley and E. M. Gelbard, Applied Physics Division

The neoclassical transport coefficients of a multispecies tokamak plasma have recently been obtained in several combinations of collisionality regimes.[1] At present they are being incorporated into the Argonne 1-D transport code, along lines proposed earlier.[2] Those neoclassical transport coefficients which give the Ware fluxes and bootstrap current are expressed in terms of the classical Spitzer function f^s_{a1}, which satisfies

$$-\frac{e_a f_{ao}}{T_a} v_{\|} E_{\|} = \sum_b \{C_{ab}[f^s_{a1}, f_{bo}] + C_{ab}[f_{ao}, f^s_{b1}]\}$$

where the notation is conventional.[1] The Spitzer function is presently being evaluated for a multispecies system. Thus far, several model systems have been considered, including the cases:

(a) One species, with an arbitrary number of charge states;

(b) A disparate-mass system, in which particles of each species are much lighter than or much more massive than particles of the other species; and

(c) A disparate-mass system like (b), with the generalization that each species can have various charge states.

In each case the Spitzer function, expanded in Sonine polynomials, can be calculated explicitly. In the future, attention will be focused on removal of the mass restriction in cases (b) and (c), and on the development of an interpolation scheme.

---

[1] S. P. Hirshman and D. J. Sigmar, *Phys. Fluids*, 20, p. 418 (1977); and E. M. Gelbard and S. P. Hirshman, *Phys. Fluids* (to be published).

[2] C. D. Boley, "Summary of Neoclassical Transport Coefficients for a Multispecies, Mixed-Regime Tokamak Plasma," Argonne National Laboratory, ANL/FPP/TM-101 (December, 1977).

B. Bethe Cross Sections for Ionization of Na and Fe^{15+} by Fast Electrons

Y.-K. Kim and K. T. Cheng, Radiological and Environmental Research Division

The sum rule method[3] for the Born cross sections was applied to Na and Fe^{15+}. The resulting cross section, known as the Bethe cross section, has the form

$$\sigma_{ion} = T^{-1} (A \ln T + B), \tag{1}$$

where T is the incident-electron energy in eV, and A and B are atomic constants independent of T. The values of A and B for Na and Fe^{+} are listed in Table VI-1. Equation (1) is to be used when the incident electron has an energy $\sim$ 10 times the ionization potentials (5.1 eV for Na and 331 eV for Fe^{15+}) or higher. For very fast electrons ($\sim$ 5 keV and up), one should use the relativistic form

$$\sigma_{ion} = \beta^{-2} \{A' [\ln \left(\frac{\beta^2}{1 - \beta^2}\right) - \beta^2] + B'\}, \tag{2}$$

where $\beta (= v/c)$ is the ratio of the electron speed to that of light. The values of A' and B' are also listed in Table VI-1.

Table VI-1. Parameters for the Bethe Cross Sections for Ionization of Na and Fe^{15+} by Electron Impact. The constants are in units of 10^{-16} cm^2.

Target	A	B	A'	B'
Na	64.2	-125	2.54×10^{-4}	7.49×10^{-4}
Fe^{15+}	5.33	- 19.2	5.93×10^{-6}	4.67×10^{-5}

The constants A and B were evaluated from the relativistic Hartree-Fock wavefunctions and from continuum f values based on the Herman-Skillman potential.[4]

---

[3] Y.-K. Kim and M. Inokuti, *Phys. Rev. A*, 3, p. 665 (1971).

[4] J. L. Dehmer, M. Inokuti and R. P. Saxon, *Phys. Rev. A*, 12, p. 102 (1975).

Our result on Na supports the calculation by McGuire,[5] whose result is almost a factor of two smaller than the theoretical result by Omidvar, et al.[6] as well as the experimental results by McFarland and Kinney.[7] The possibility that the experimental results by McFarland and Kinney might be too large was also pointed out by Jalin, et al.[8]

---

[5] E. J. McGuire, *Phys. Rev. A*, 3, p. 267 (1971).

[6] K. Omidvar, H. L. Kyle and E. C. Sullivan, *Phys. Rev. A*, 5, p. 1174 (1972).

[7] R. H. McFarland and J. D. Kinney, *Phys. Rev.*, 137, p. 1058 (1965).

[8] R. Jalin, R. Hagemann and R. Botter, *J. Chem. Phys.*, 59, p. 452 (1973).

FPP AND FPP-RELATED DOCUMENTS AUTHORED BY ARGONNE PERSONNEL

S. AGARWAL, D. I. POTTER AND A. TAYLOR
"Void Swelling in V-Ion Irradiated V-O Alloys"
Presented at the ANS Annual Meeting, June 12-16, 1977, New York; to be published in the *Journal of Nuclear Technology*.

S. C. AGARWAL, D. I. POTTER AND A. TAYLOR
"Effects of Interstitial Solutes on the Microstructures of Self-Ion Irradiated Vanadium"
Proceedings of the Eighth International ASTM Symposium on The Effects of Radiation on Structural Materials, May 4-6, 1976.

B. S. BROWN
"A Summary of the International Discussion Meeting on Radiation Effects on Superconductivity"
Presented at the International Cryogenic Materials Conference, August 2-5, 1977, Boulder, Colorado.

F. CAFASSO, D. GRUEN, M. KAMINSKY, J. E. ROBINSON AND H. WIEDERSICH
"A New Approach to Assessing Fusion Plasma-Materials Interactions"
Nuclear Technology, 34, pp. 131-134 (July, 1977).

H. FARRAR IV, D. W. KNEFF, R. A. BRITTEN AND R. R. HEINRICH
"Fluence Trapping of RTNS-I by Helium Accumulation and Foil Activation Methods"
Proceedings of Symposium on Neutron Cross-Sections from 10-40 MeV, p. 391, BNL-NCS-50681.

D. G. DORAN, R. R. HEINRICH, L. R. GREENWOOD AND H. FARRAR IV
"MFE Damage Analysis Program Nuclear Data Needs"
Proceedings of Symposium on Neutron Cross-Sections from 10-40 MeV, p. 175, BNL-NCS-50681.

R. FUJA, R. KUSTOM AND R. P. SMITH
"Results from a Model System of Superconducting Solenoids and Phase Shifting Bridge for Pulsed Power Storage Studies for Proposed Tokamak EF Coils"
Presented at the International Cryogenic Materials Conference, August 2-5, 1977, Boulder, Colorado.

E. S. FISHER, S. H. KIM, R. J. LINZ AND A. P. L. TURNER
"Effects of Cyclic Strains on Transport Properties of a Superconducting Composite: Phase I, Degradation of Electrical Conductivity in Copper at 4.2 K"
Argonne National Laboratory, ANL-77-50 (August, 1977).

L. R. GREENWOOD AND R. R. HEINRICH
"Integral Testing of Neutron Activation Cross Sections Using the $^{9}Be(d,n)$ Reaction at 14-16 MeV"
Proceedings of Symposium on Neutron Cross-Sections from 10-40 MeV, p. 391, BNL-NCS-50681.

R. T. KAMPWIRTH, C. T. WU AND J. W. HAFSTROM
"Nb_3Ge and Nb_3Sn Films Prepared by High Rate Magnetron Sputtering"
Presented at the International Cryogenic Materials Conference, August 2-5, 1977, Boulder, Colorado.

S. H. KIM, S. T. WANG AND L. R. TURNER
"Effects of Elec rical Shorts on Cryostatic Stable Superconducting Magnets"
Presented at the International Cryogenic Materials Conference, August 2-5, 1977, Boulder, Colorado.

S. H. KIM AND S. T. WANG
"The Measurements of Mechanical and Electrical Properties of High Purity Aluminum and Aluminum Soldering Joints"
Presented at the International Cryogenic Materials Conference, August 2-5, 1977, Boulder, Colorado.

J. MEADOWS, W. POENITZ, A. SMITH, D. SMITH, J. WHALEN AND R. HOWERTON
"Evaluated Nuclear Data File of Th-232"
Argonne National Laboratory, ANL/NDM-35

D. R. NETHAWAY, R. A. VAN KONYNENBURG, M. W. GUINAN AND L. R. GREENWOOD
"Neutron Spectra from 30-MeV Deuterons on a Thick Beryllium Target"
Proceedings of Symposium on Neutron Cross-Sections from 10-40 MeV, p. 135, BNL-NCS-50681.

R. NIEMANN, J. GONCZY, K. MATAYA AND P. SMELSER
"An Epoxy Fiberglass Tension Member Support for Superconducting Magnets"
Presented at the International Cryogenic Materials Conference, August 2-5, 1977, Boulder, Colorado.

R. C. NIEMANN, S. T. WANG, P. SMELSER, J. GONCZY, K. MATAYA, W. J. PELCZARSKI, P. VANDER AREND AND S. STOY
"Cryogenic Aspects of the U.S. SCMS Superconducting Dipole Magnet for MHD Research"
Presented at the International Cryogenic Materials Conference, August 2-5, 1977, Boulder, Colorado.

W. P. POENITZ, E. PENNINGTON, A. SMITH AND R. HOWERTON
"Evaluated Fast Neutron Cross Sections of Uranium 238 for ENDF/B-V"
Argonne National Laboratory, ANL/NDM-32

C. PHILIS, R. HOWERTON AND A. B. SMITH
"Titanium II - An Evaluated Neutron Data File"
Argonne National Laboratory, ANL/NDM-28

D. L. SMITH
"Graphical Representation of Neutron Differential Cross Section Data for Reactor Dosimetry Applications"
Argonne National Laboratory, ANL/NDM-34

D. L. SMITH AND J. W. MEADOWS
"Neutron Inelastic Scattering Studies for Lead-204"
Argonne National Laboratory, ANL/NDM-37

L. R. TURNER, S. T. WANG AND P. SMELSER
"Superconducting Coil Design for a Tokamak Experimental Power Reactor"
Presented at the Sixth International Conference on Magnet Technology, August 25-28, 1977, Bratislava, Czechoslovakia.

L. R. TURNER, S. T. WANG AND S. H. KIM
"Field-Screening Calculations for Superconducting Tokamak Magnets"
Presented at the Sixth International Conference on Magnet Technology, August 25-28, 1977, Bratislava, Czechoslovakia.

E. VELECKIS, R. M. YONCO AND V. A. MARONI
"Solubility of Lithium Deuteride in Liquid Lithium"
Journal of Less-Common Metals, 55, p. 85 (1977).

S. T. WANG, S. H. KIM, L. R. TURNER, K. M. THOMPSON, W. F. PRAEG, C. KRIEGER AND R. L. KUSTOM
"Design and Development of Cryostable Superconducting Ohmic Heating Coils for a Tokamak"
Presented at the International Cryogenic Materials Conference, August 2-5, 1977, Boulder, Colorado.

S-T. WANG, S. H. KIM, W. F. PRAEG AND C. I. KRIEGER
"A 1.5 MJ Cryostatic Stable Superconducting Ohmic Heating Coil"
Presented at the Sixth International Conference on Magnet Technology, August 25-28, 1977, Bratislava, Czechoslovakia.

S. T. WANG, R. C. NIEMANN, R. L. KUSTOM, P. SMELSER, W. J. PELCZARSKI, L. R. TURNER, E. W. JOHANSON, S. H. KIM, J. D. GONCZY, H. F. LUDWIG, K. F. MATAYA, W. E. LaFAVE, F. J. LAWRENTZ AND F. P. CATANIA
"Fabrication Experience and Operating Characteristics of the U.S. SCMS Superconducting Dipole for MHD"
Presented at the International Cryogenic Materials Conference, August 2-5, 1977, Boulder, Colorado.

S. T. WANG, R. P. SMITH, J. J. PEERSON, P. SMELSER, S. H. KIM AND S. W. GRAY
"Design and Development of a Large Superconducting Solenoid with Aluminum Stabilized Superconductors"
Presented at the International Cryogenic Materials Conference, August 2-5, 1977, Boulder, Colorado.

S-T. WANG, L. R. TURNER, K. M. THOMPSON, S. H. KIM AND R. L. KUSTOM
"A Conceptual Design on Superconducting OH Coil for the Argonne/GA TNS Tokamak Reactor"
Presented at the Sixth International Conference on Magnet Technology, August 25-28, 1977, Bratislava, Czechoslovakia.

C. K. YOUNGDAHL
"First Wall Stress Analysis for a Tokamak Reactor"
Nuclear Engineering and Design, 42 (2), pp. 391-407 (1977).

Distribution of ANL/FPP-77-4

Internal:

M. Abdou
C. C. Baker
C. C. Bolta
J. Brooks
F. Cafasso
J. B. Darby
D. Ehst
K. Evans
J. Fasolo
E. Gelbard
L. Greenwood
D. M. Gruen, A. Krauss
S. Harkness
M. Kaminksy, S. Das, P. Dusza
R. L. Kustom, W. Kim, W. Praeg, S-T. Wang
V. Maroni
F. Nolfi, B. Hall, H. Wiedersich
D. L. Smith
B. Ancker-Johnson
R. Avery
L. Burris, Jr.
E. J. Croke
S. A. Davis
P. R. Fields
B. R. T. Frost
P. F. Gustafson
R. V. Laney
R. L. Martin
M. V. Nevitt
E. N. Pettitt
E. G. Pewitt
D. C. L. Price
R. J. Royston
R. G. Sachs
W. K. Sinclair
C. E. Till
J. B. van Erp
R. S. Zeno
G. T. Garvey
A. D. Kulsciunas
FP Program (21)
ANL Contract Copy
ANL Libraries (5)
TIS Files (5)

External:

DOE-TIC, for distribution per UC-20, plus -20a through -20g (406)
Manager, Chicago Operations Office
Chief, Chicago Patent Group
President, Argonne Universities Association
Applied Physics Division Review Committee:
  P. Crecbler, General Electric Co., Sunnyvale
  R. L. Hellens, Combustion Engineering, Inc.
  W. B. Loewenstein, Electric Power Research Inst.
  R. F. Redmond, Ohio State U.
  R. Sher, Stanford U.
  D. B. Wehmeyer, Detroit Edison
  S. A. Werner, U. Missouri
Chemical Engineering Division Review Committee:
  R. C. Axtmann, Princeton U.
  J. T. Banchero, U. Notre Dame
  D. L. Douglas, Gould Inc.
  P. W. Gilles, U. Kansas
  R. I. Newman, Allied Chemical Corp.
  G. M. Rosenblatt, Pennsylvania State U.
Chemistry Division Review Committee:
  J. Bigeleisen, U. Rochester
  W. H. Flygare, U. Illinois
  H. F. Franzen, Iowa State U.
  H. S. Gutowsky, U. Illinois
  D. R. Herschbach, Harvard U.
  E. L. Muetterties, Cornell U.

J. O. Rasmussen, Lawrence Berkeley Lab.
F. S. Rowland, U. California, Irvine
J. H. Wang, State U. New York, Buffalo

Components Technology Division Review Committee:
J. W. Dally, U. Maryland
W. E. Kessler, Commonwealth Associates
N. J. Palladino, Pennsylvania State U.
N. C. Rasmussen, Massachusetts Inst. Technology
M. A. Schultz, Pennsylvania State U.
A. Sesonske, Purdue U.
H. Thielsch, ITT Grinnell Corp.

Materials Science Division Review Committee:
G. S. Ansell, Rensselaer Polytechnic Inst.
R. W. Balluffi, Cornell U.
S. L. Cooper, U. Wisconsin
S. Doniach, Stanford U.
H. L. Falkenberry, Tennessee Valley Authority
C. Laird, U. Pennsylvania
D. Lazarus, U. Illinois
M. T. Simnad, General Atomic
A. R. C. Westwood, Martin Marietta Labs.

Physics Division Review Committee:
B. Bederson, New York U.
D. A. Bromley, Yale U.
W. L. Brown, Bell Telephone Labs.
R. Middleton, U. Pennsylvania
D. E. Nagle, Los Alamos Scientific Lab.
J. W. Negele, Massachusetts Inst. Technology
H. B. Willard, Case Western Reserve U.

Reactor Analysis and Safety Division Review Committee:
S. Baron, Burns and Roe, Inc.
W. Kerr, U. Michigan
M. Levenson, Electric Power Research Inst.
S. Levy, S. Levy, Inc.
R. B. Nicholson, Exxon Nuclear Co., Inc.
D. Okrent, U. California, Los Angeles

Solid State Science Division Review Committee:
C. P. Flynn, U. Illinois
D. M. Ginsberg, U. Illinois
K. L. Kliewer, Iowa State U.
G. A. Russell, U. Missouri

ZGS Complex Review Committee:
V. W. Hughes, Yale U.
J. D. Jackson, U. California, Berkeley
W. Lee, Columbia U.
R. B. Neal, Stanford Linear Accelerator Center
J. L. Rosen, Northwestern U.
G. A. Smith, Michigan State U.
G. H. Trilling, Lawrence Berkeley Lab.

N. Amherd, R. Scott, Electric Power Research Institute
J. Baublitz, C. Head, J. Neff, DOE/DMFE
R. Balzhiser, Electric Power Research Institute
D. Beard, F. Coffman, E. Ziurys, DOE/DMFE
Roger Boom, G. L. Kulcinski, C. W. Maynard, R. Conn, U. Wisconsin
S. Locke Bogart, DOE/DMFE

W. Briggs, D. Kummer, McDonnell-Douglas Company - East
S. J. Buchsbaum, Bell Telephone Laboratories, Inc.
G. A. Carlson, R. W. Werner, Lawrence Livermore Laboratory
R. A. Carruthers, Culham Laboratory
G. Casini, Commission of the European Community Joint Research Center, ITALY
Library, Centre de Recherches en Physique des Plasma, SWITZERLAND
J. A. Casazza, Stone & Webster Management Consultants, Inc.
R. Challender, United Kingdom Atomic Energy Authority
F. F. Chen, University of California
J. F. Clarke, DOE/DMFE
M. Clarke, Combustion Engineering
M. Collins, E. Golankiewicz, Engelhard Minerals & Chemicals Corp.
Librarian, Culham Laboratory
N. Anne Davies, R. Blanken, D. Ignat, J. Willis, DOE/DMFE
S. O. Dean, A. M. Sleeper, DOE/DMFE
J. F. Decker, G. J. Mischre, P. Stone, W. Dove, DOE/DMFE
D. Dingee, Battelle Northwest Laboratory
W. E. Drummond, H. Woodson, University of Texas at Austin
A. M. Dupas, Centre d'Etudes Nucleaires, FRANCE
T. S. Elleman, North Carolina State University
W. L. Ellis, E. Oktay, DOE/DMFE
J. Feinstein, Varian Associates, Incorporated
S. Fernbach, Lawrence Livermore Laboratory
H. Finger, Center of Energy Systems
Bibliotheque, Service du Confinement des Plasmas, CEA, Fontenay-aux-Roses
H. K. Forsen, Exxon Nuclear Company, Inc.
J. S. Foster, Jr., TRW
T. K. Fowler, Lawrence Livermore Laboratory
H. P. Furth, Princeton Plasma Physics Laboratory
M. B. Gottlieb, Princeton Plasma Physics Laboratory
J. N. Grace, K. Moses, L. K. Price, DOE/DMFE
D. Grafstein, Exxon Research & Engineering Co.
R. A. Gross, Columbia University
G. Hansen, Convair Division/General Dynamics
A. F. Haught, United Technologies Research Center
N. Hershkowitz, K. E. Lonngren, W. R. Savage, University of Iowa
I. Grant Hedrick, Grumman Aerospace Corporation
A. Hill, L. Lidsky, Massachusetts Institute of Technology
R. A. Huse, Public Service Electric & Gas Company
H. Horwitz, General Electric Company
G. R. Ingram, DOE/DMFE
Library, FOM-Institut voor Plasma-Fysica, THE NETHERLANDS
Thermonuclear Library, Japan Atomic Energy Research Institute
E. E. Kintner, DOE/DMFE
H. Kouts, Brookhaven National Laboratory
A. Kolb, Maxwell Laboratories
W. B. Kunkel, University of California, Berkeley
Library, Kurchatov Institute of Atomic Energy, U.S.S.R.
Library, Laboratorio Gas Ionizata, ITALY
S. Hale Lull, Northeast Utility Service Company
R. Lengye, Bibliothek, Max Planck Institut fur Plasmaphysik
G. H. Miley, F. H. Southworth, R. Turnbull, University of Illinois
R. Meyerand, United Technologies Research Center
T. Ohkawa, General Atomic Company

R. E. Price, I. L. Sadowski, D. M. Priester, DOE/DMFE
S. Naymark, Nuclear Services Corporation
J. Purcell, General Atomic Company
R. Davidson, DOE/DMFE
D. R. Morgan, L. A. Berry, ORNL
D. Steiner, M. Roberts, ORNL
R. Raeder, Max-Planck-Institute fur Plasmaphysik
H. Dreicer, Los Alamos Scientific Laboratory
C. Rickard, General Atomic Company
K. H. Schmitter, Max-Planck-Institute fur Plasmaphysik
Z. Shapiro, Westinghouse Electric Corporation
M. N. Rosenbluth, Institute of Advanced Study, Princeton, New Jersey
W. M. Stacey, Jr., Georgia Institute of Technology
J. Williams, DOE/DMFE
P. Rose, North West Inc.
H. Willenberg, Battelle - Northwest Laboratory
K. Zwilsky, M. Cohen, E. Dalder, C. Finfgeld, T. Reuther, DOE/DMFE
D. Stekart, DOE

☆ U.S. GOVERNMENT PRINTING OFFICE: 1978 — 750-133